Journal of Materials Chemistry A

ROYAL SOCIETY OF CHEMISTRY

REVIEW

View Article Online
View Journal | View Issue

Cite this: J. Mater. Chem. A, 2026, 14, 783

Multifunctional polymers in perovskite photovoltaics: bridging efficiency, stability, and manufacturing

Farzad Zahedi,[a] Mohsen Ameri,*[b] Mohammad Hossein Rajabi Manshadi,[c] Mohammad Jafari Pouya,[c] Marziyeh Mohebbi,[d] Maryam Alidaei,[e] Siming Huang,[f] Tandis HosseinMirzaie,[c] Galyam Sanfo[f] and Mojtaba Abdi-Jalebi*[f]

Polymers have emerged as multifunctional enablers in the evolving architecture of perovskite solar cells (PSCs), addressing key challenges in film formation, interface engineering, defect modification, and device longevity. Their molecular tunability, macromolecular chains, and compatibility with low-temperature solution processing make them ideal candidates for integration at various functional layers within PSCs. This review delineates the strategic roles of polymers as both passive and active components in PSCs and emphasizes their indispensable contribution toward scalable, printable perovskite photovoltaics. In the active layer, polymeric additives modulate the nucleation and crystal growth kinetics of the perovskite phase, leading to adjusted grain size, reduced trap states, and suppressed ion migration. At the interfaces, conjugated polymers serve as efficient charge-transport materials (CTMs), offering favorable energy level alignment and improved mechanical adhesion, while insulating polymers mitigate interface-induced recombination and phase instability. Additionally, polymers have been pivotal in enabling flexible and lightweight PSCs. This review provides a comprehensive overview of perovskite defects and systematically investigates the role of polymers in enhancing the properties of PSCs. We explore the incorporation of polymers into the active layer, charge transport layers (CTLs), and their interfaces, highlighting recent advancements in self-healing, deep-level trap passivation, network formation, the use of hyperbranched polymers for flexible devices, and so on. A detailed analysis of semiconducting polymers, focusing on main-chain and side-chain structures, physical properties, and dopant-free systems, is presented for both the active layer as the bulk heterointerface and CTLs. Finally, addressing the imminent industrialization of PSCs, we examine various printing techniques and propose polymer-based strategies to mitigate structural defects during large-scale fabrication, concluding with a perspective on future scalability.

Received 12th September 2025
Accepted 21st October 2025

DOI: 10.1039/d5ta07481a

rsc.li/materials-a

1 Introduction

Perovskite materials, known for their high absorption coefficients, long carrier diffusion lengths, high carrier mobilities, and bipolar transport characteristics, have significantly enhanced the efficiency of third-generation solar cells. They effectively absorb sunlight over a wide wavelength range, capturing more solar energy. These materials allow charge carriers to travel long distances without recombining, which is crucial for efficient charge extraction and high device performance. The bandgap of perovskite materials can be easily tuned by adjusting the composition of metal halides, and optimizing light absorption and energy conversion efficiency.[1–3] The simplicity of perovskite thin film fabrication, compositional engineering, and accessible solution-based fabrication protocols have driven research and quickly boosted efficiency to over 27.5%,[4] rivalling traditional silicon-based solar cells.

In PSCs, a perovskite absorber layer is situated between an ETL and a HTL. These layers are designed to extract and direct photo-generated electrons and holes into the circuit. However, this process is hindered by defects within the perovskite structure and during fabrication. These defects lead to issues such as charge recombination and ion migration, which reduce the efficiency and stability of PSCs and make them susceptible to degradation from external factors like moisture, heat, and light.[5] Therefore, managing the fabrication process and

[a]Polymer Engineering Department, Amirkabir University of Technology (Tehran Polytechnic), Tehran, Iran
[b]First Solar, Inc., 28101 Cedar Park Blvd., Perrysburg, OH 43551, USA. E-mail: mohsen.ameri@firstsolar.com
[c]Physics Department, Faculty of Science, University of Tehran, Iran
[d]Department of Chemistry, University of Isfahan, Isfahan, 81746-73441, Iran
[e]Faculty of Electrical and Computer Engineering, Tarbiat Modares University, Tehran, Iran
[f]Institute for Materials Discovery, University College London, Malet Place, London WC1E 7JE, UK. E-mail: m.jalebi@ucl.ac.uk

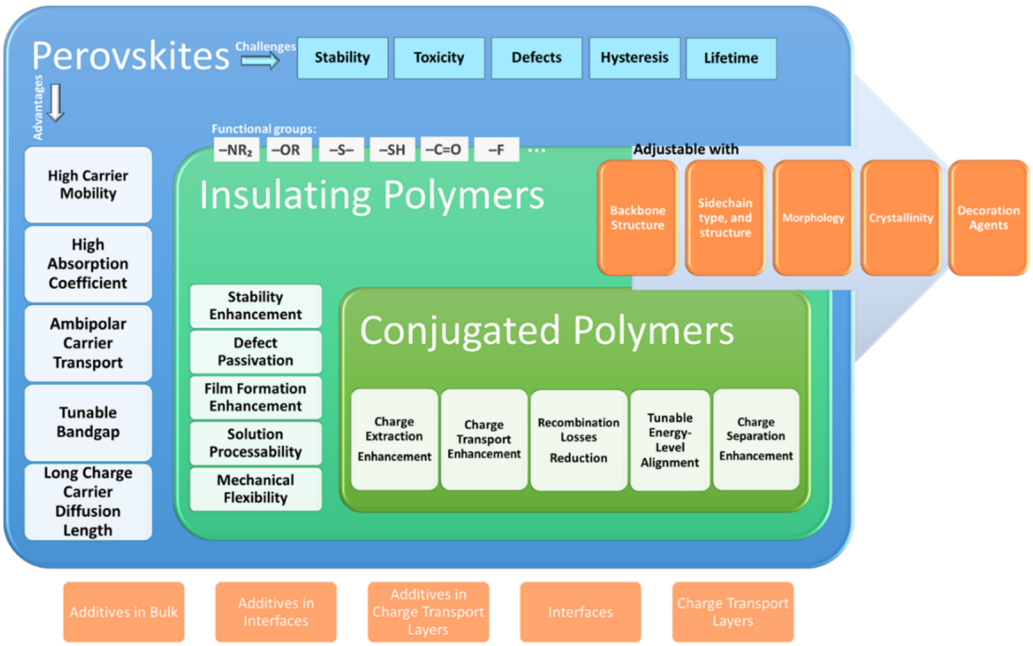

Fig. 1 Benefits and challenges of perovskites and synergistic effects of polymers for use in perovskite solar cells.

passivating these defects is essential for achieving high performance and stability.

The morphology of the perovskite layer, both in the bulk and on the surface, plays a critical role in photovoltaic performance.[6] Researchers aim to manipulate the composition and interfaces to reduce recombination, enhance charge transport, extend charge carrier lifetime, and improve stability. For this purpose, two goals are running in parallel, one is the engineering of perovskite compounds and the other is the employment of suitable materials to passivate defects.[7–9] Perovskite passivation includes a broad range of techniques with various agents from inorganic additives to polymers.

Among the materials, small molecules are beneficial but macromolecules are more efficient. Polymers can be engineered to have a wide range of properties, such as energy level alignment, charge mobility, and solubility, which are crucial for optimizing the performance of solar cells. They tend to form high-quality films with fewer defects, which is essential for producing uniform layers. Polymers can improve the stability of perovskite solar cells under environmental stressors like moisture, heat, and UV light, which is a significant advantage over small molecules. The structures of polymer–perovskite solar cells are of great significance due to their potential for high efficiency and stability.[10–12] Fig. 1 depicts, in a categorized manner, some of the most important advantages and limitations of PSCs and the role of polymers in them.

In this review, we begin by briefly outlining the various types of defects present in perovskite materials. We then explore how polymers can be strategically employed to enhance the performance of perovskite solar cells. To this end, we first touch upon the key factors of polymeric additives and then examine their integration into the active layer, CTLs, and their corresponding interfaces. This discussion highlights cutting-edge research, including self-healing mechanisms, passivation of deep-level traps, network formation, the application of hyperbranched polymers in flexible solar cells, and so on. Subsequently, we offer an in-depth analysis of semiconducting polymers (SCPs), investigating the influence of main-chain and side-chain engineering, physical and crystalline properties, dopant-free systems, and donor–acceptor polymers within the device architecture. Given the impending commercialization of this technology, we then address the challenges of scalable manufacturing by evaluating various printing methods. We identify key structural challenges associated with printing and present polymer-based solutions drawn from both foundational and recent studies. Finally, we conclude with a forward-looking perspective on the large-scale production of polymer-enhanced PSCs (see Fig. 2).

2 Perovskite defects and passivation

The primary cause of defects in perovskite materials is their tendency for rapid crystallization. Ideally, a crystal structure would have each atom in a fixed location without imperfections or gaps. However, during the formation of films, numerous defects naturally occur within the crystal structure.[13] Perovskite films are often composed of polycrystals with inherent grain boundaries, which contribute to defect creation and energy band misalignment. Any deviation in the atomic arrangement of a crystalline solid is considered a defect.[14] In PSCs, defects can include traditional solid-state imperfections as well as various types classified as planar (*e.g.*, grain boundaries and stacking faults), bulk (*e.g.*, pores and precipitates), point defects (*e.g.*, vacancies, interstitials, substitutions, antisites, Frenkel, Schottky, and impurity types), and line defects (*e.g.*,

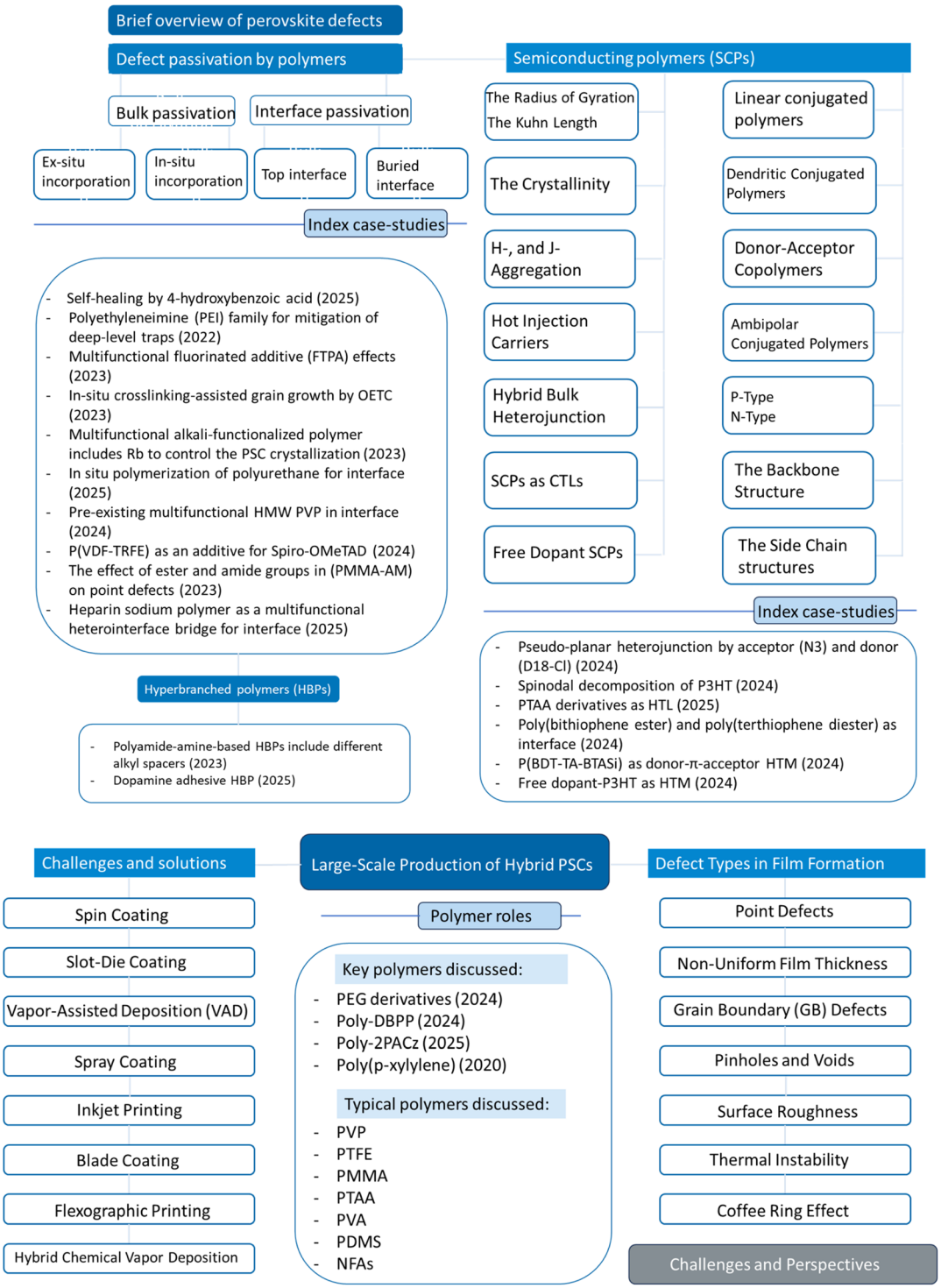

Fig. 2 Hierarchical chart summarizing the key themes of this paper, including polymer-assisted defect passivation strategies, the roles of semiconducting polymers, and the challenges and perspectives in large-scale production of hybrid perovskite solar cells.

dislocations, disclinations, and cracks).[15] See Fig. 3 for a summary of the defects.

Imperfections typically induce shallow or deep energy levels within the band structure. Shallow-level defects, which can be identified by a redshift in the photoluminescence (PL) peak, cause energy loss due to charge capture.[16] These defects are near the band edge and provide potential pathways for trapped electrons to recombine within the conduction or valence bands. On the other hand, deep-level defects capture charges that lead to non-radiative recombination, with most energy dissipated as phonons to the neighboring lattice. This severely impacts the

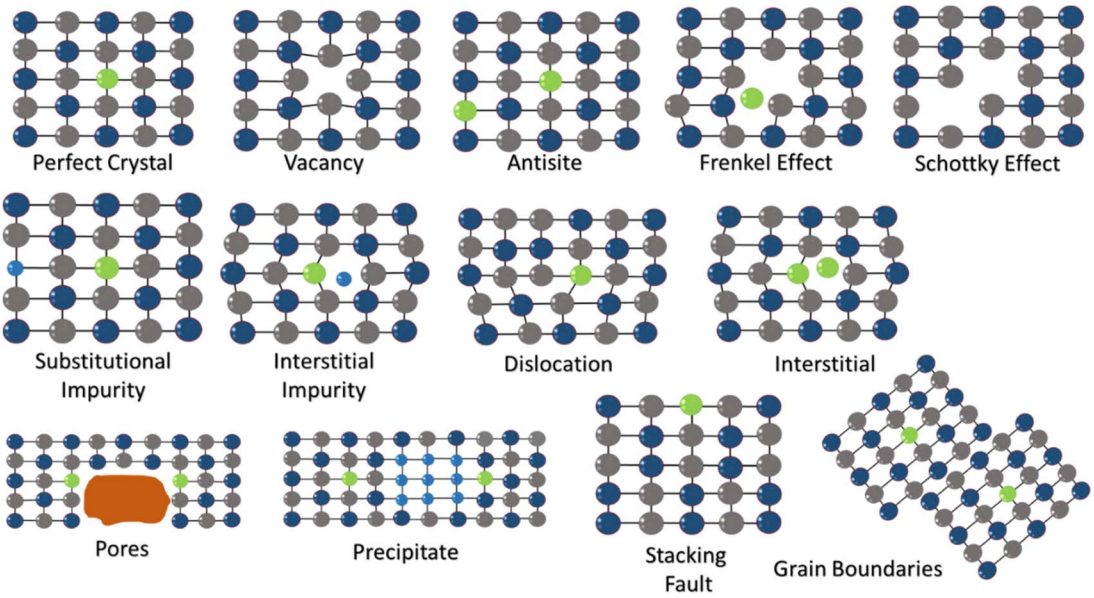

Fig. 3 Defect types in the perovskite lattice.

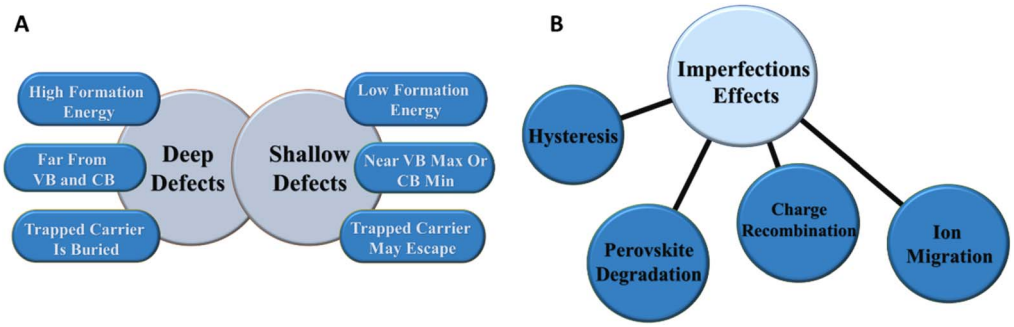

Fig. 4 Schematic of defect types in PSCs. (A) The consequences of imperfection effects in the PSCs (B).

performance of PSCs by reducing carrier density, diffusion length, and lifetime.[17]

From an energy level perspective, defects create trap states for charge carriers, with the depth of these trap states indicating the potential risk they pose. Shallow defects are less energetically activated and are close to the valence band maximum (VBM) or conduction band minimum (CBM), often allowing trapped carriers to escape.[18] Conversely, deep defects are the most destructive, possessing high formation energy and energy levels distant from the VBM and CBM, leading to carrier recombination and reduced PSC efficiency (Fig. 4A). Some researchers introduced the term defect tolerance to explain the unusually long carrier diffusion length in perovskites compared to traditional semiconductors, attributing this characteristic to atomic orbital coupling within the material.[19,20] Due to the antibonding nature of the molecular orbitals in perovskites, the material inherently exhibits more shallow defects, making it more defect tolerant. This means that these defects do not severely disrupt charge carriers, leading to reduced recombination and enhanced PCE. Further computational studies expanded on this concept by examining the role of ions in perovskites, providing deeper insights into both deep and shallow defects. Although the sharp absorption edge and unique defect tolerance of perovskites have been acknowledged, recent research studies have shed more light on the nature of these defects. This increased understanding highlights the necessity of defect passivation to mitigate their adverse effects, which is essential for producing high-performance PSCs.[21–23]

2.1 Adverse effects of perovskite defects

Defects and trap states facilitate carrier recombination, especially at interfaces, lowering performance despite improvements in bulk film quality (Fig. 4B). High-quality perovskite films reduce recombination losses, but interfaces remain critical hotspots for charge accumulation and performance loss. Defects and grain boundaries trigger ion movement, causing instability, hysteresis, and phase segregation; passivation is required for long-term stability. Carrier trapping at interfaces causes scan-dependent *J–V* curves and reduced efficiency. Structural strain (*e.g.*, from lattice mismatch or the

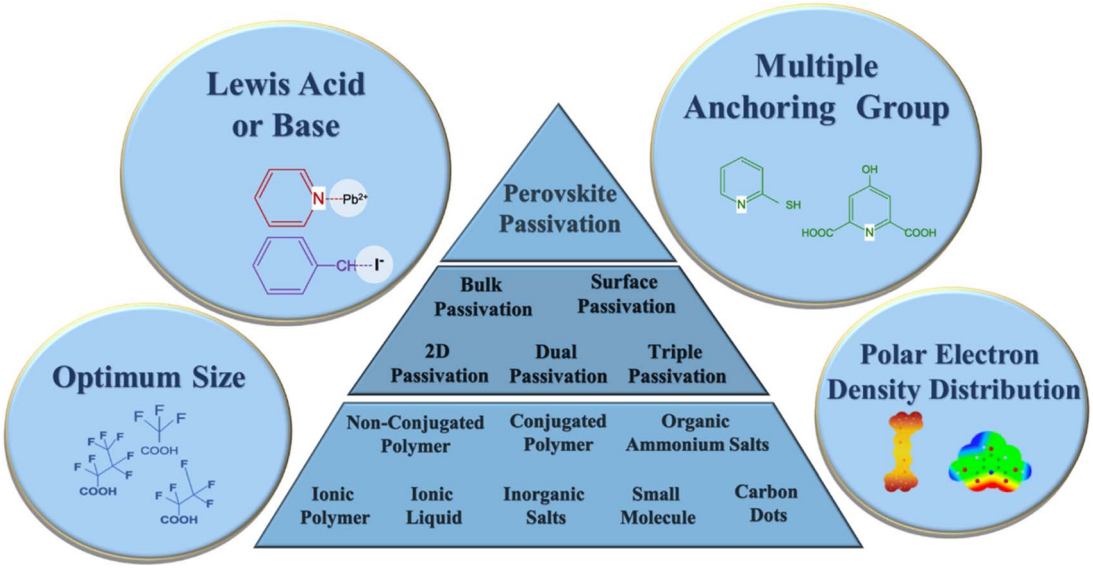

Fig. 5 General methods for passivation of perovskite photovoltaics. Perovskite passivation strategies are diverse, employing various chemical and structural modifications to neutralize defects that hinder efficiency and stability. 2D passivation involves using large organic cations to create a two-dimensional perovskite layer on the surface of the three-dimensional film. This layer acts as a barrier, passivating surface defects and preventing moisture infiltration. Dual and triple passivation involves the simultaneous use of two or three different passivating agents, respectively, to target a wider range of defect types. These agents often have distinct properties, such as one being a Lewis base with lone-pair electrons that coordinate with undercoordinated Pb^{2+} ions, while another might be a Lewis acid that accepts electrons. Many effective passivators utilize multiple anchoring groups to create stronger, more stable bonds with the perovskite lattice. Additionally, some molecules are designed with a polar electron density distribution, which helps them to interact more effectively with charged defects and minimize non-radiative recombination.

Goldschmidt tolerance factor) worsens instability, necessitating strain control.[24] Intrinsic defects accelerate recombination, ion migration, and environmental sensitivity (moisture, heat, and light). These reduce the open-circuit voltage (V_{OC}), mainly through non-radiative recombination. The V_{OC} is limited by the bandgap (E_g) of the semiconductor in the absorber layer and is further decreased by the recombination of electrons and holes, both through radiative and non-radiative processes.[25] Eqn (1) frequently defines the V_{OC}:

$$V_{OC} = V_{OC}^{rad} - \Delta V_{OC}^{non\text{-}rad} \quad (1)$$

where $V_{OC}^{non\text{-}rad}$ represents the loss in V_{OC} due to non-radiative recombination, and V_{OC}^{rad} is the V_{OC} at the radiative limit, where all recombination is radiative. Currently, the individual contributions of radiative and non-radiative activities to the voltage deficit ($E_g - qV_{OC}$) remain unknown. However, it is observed that the V_{OC} decreases with increasing non-radiative losses, primarily due to surface defects.[26]

2.2 Passivation strategies for perovskite defects

Passivation in PSCs is driven by chemical and physical interactions (*e.g.*, charge balance, Lewis acid–base, and steric effects) to neutralize defects. Effective strategies, targeting either bulk or surface/interface traps, are essential for improving device performance and stability. Various strategies are introduced to mitigate the effects of perovskite defects, considering appropriate chemical and physical effects.[27–29] Although the mechanisms of many passivation techniques are still not fully understood, an overview of passivation routes is provided in Fig. 5.

3 Defect passivation by using polymers

Various passivation agents have been used in the literature including organic molecules, inorganic materials,[30,31] zwitterions, ionic salts, and polymers. Polymers are promising passivation agents due to their durability under operation conditions, possible multi-functionality, presence of hydrophobic long chains, the possibility of *in situ* polymerization inside the layer, good solubility and interference in the film-formation process, ion immobilization ability, *etc.*[32–34]

Since defect formation largely occurs during the fabrication of perovskite, and due to the inherently defective nature of the surface and CTL/perovskite interfaces in a PSC, researchers have generally considered two primary approaches for PSC defect passivation, perovskite bulk and interface passivation. Within the scope of this review, we will sequentially focus on the use of polymers in these two main approaches to passivation.

3.1 Bulk passivation by using polymers

As illustrated in Fig. 6A, polymers can be integrated into perovskite materials using either an *ex situ* or *in situ* approach.

3.1.1 *Ex situ* polymer introduction. In the *ex situ* method, a specific quantity of a polar polymer is directly introduced into

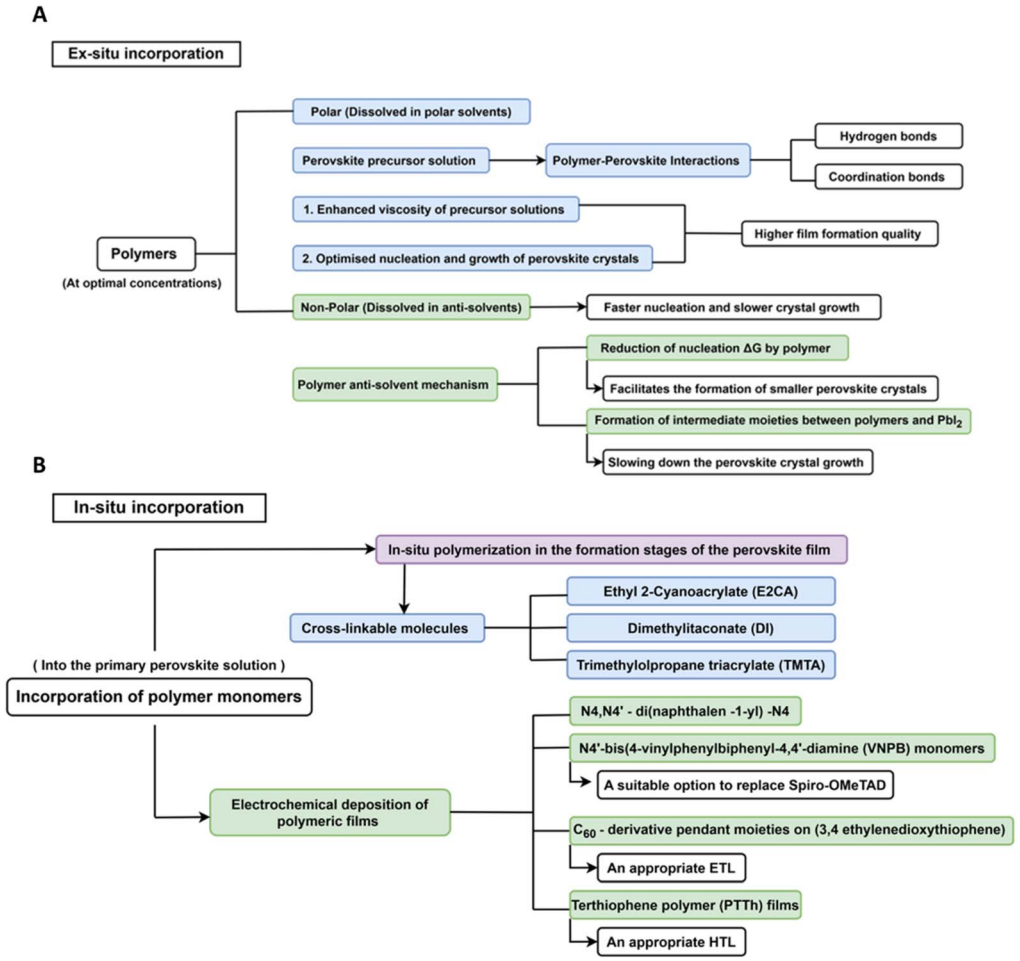

Fig. 6 A summary chart of polymer incorporation methods in perovskites, *ex situ* (A) and *in situ* (B).

the polar solvents that dissolve the perovskite precursors.[35] This results in a polymer-precursor solution that enhances coordination and promotes long-range molecular arrangement along the polymer backbone, and even side chains. The underlying mechanism involves Lewis acid–base interactions between the polymer chains and perovskite precursor molecules, facilitating a more structured molecular organization. Furthermore, the presence of polymer chains increases the energy barrier required for nucleation, thereby reducing the likelihood of spontaneous nucleation events. Consequently, fewer nuclei are formed, and their subsequent growth occurs in a more continuous manner without collisions. Upon thermal annealing, the perovskite precursors that are initially bound within the polymeric matrix crystallize after overcoming the increased activation energy barrier for nucleation. The perovskite crystals that form near the extended polymer chains become stabilized by the surrounding polymer structure, promoting the interconnection of large perovskite grains through polymer linkages.[36]

On the other hand, when non-polar polymers are utilized, they can be introduced *via* the anti-solvent method.[37] During the fabrication of thin perovskite films, an anti-solvent (such as chlorobenzene, toluene, or diethyl ether) is employed to rapidly remove the primary solvent (such as DMF or DMSO) during the spin-coating process. This rapid extraction triggers the immediate nucleation of the perovskite phase. When polymers are incorporated into the anti-solvent, they interact with perovskite precursors, altering the kinetics of crystallization by either decelerating the process or modulating grain formation. This modification ensures more regulated grain growth, thereby minimizing the formation of excessive grain boundaries and structural defects. The incorporation of polymers can influence the surface energy of the perovskite film, thereby improving its compatibility with CTLs. Furthermore, hydrophobic polymers establish a protective layer over the perovskite surface, serving as a barrier against moisture ingress and enhancing the material's overall stability.[38] Certain polymers also mitigate residual mechanical stress and strain, reducing the risk of crack formation or pinhole defects within the perovskite film.[39]

It should be considered that strong polymer–PbI_2 interactions can increase nucleation density but reduce grain size, making it difficult to achieve a well-dispersed, homogeneous polymer–perovskite composite. This often leads to suboptimal film quality and diminished performance enhancements.[40]

3.1.2 *In situ* polymer introduction. According to Fig. 6B, incorporating polymers *in situ* (directly during perovskite

formation) or using cross-linkable monomers is a powerful strategy to enhance PSC performance and stability.[41] This approach allows polymers to integrate intimately with the perovskite structure, improving film quality, defect passivation, and mechanical robustness. Monomers are introduced into the perovskite ink and polymerized *in situ via* heat/UV light.[42,43] In this method, the monomers or oligomers remain well-dispersed in the perovskite matrix during the solution-processing stage. Upon film formation and post-deposition treatment, these monomers polymerize or cross-link, forming a polymeric network within the perovskite layer. The cross-linking process locks the polymer chains in place, enhancing mechanical stability, and interfacial compatibility. The *in situ* cross-linking process affects the nucleation and growth of perovskite grains, leading to larger and more uniform grain sizes with fewer defects. The polymer network reduces internal stresses within the perovskite film, preventing microcracks and enhancing mechanical stability. This approach also suppresses ion migration, which, as mentioned, is one of the major degradation pathways in perovskite solar cells.[44,45]

Totally, the molecular structure of polymer passivation agents and their interaction with perovskite crystals are key factors that are not fully understood. As a result, selecting an appropriate polymeric surface passivation agent often requires complex trial-and-error processes. Therefore, a guideline for identifying the most effective passivating functional groups within the polymeric structure to neutralize charged defects and extend the device lifespan is greatly needed. Fig. 7 summarizes some of the most commonly used insulating polymers in hybrid PSCs.

The agent used in a study is 4-hydroxybenzoic acid (4-HBA), which acts as a crosslinking agent that polymerizes *in situ* to form a network, playing multiple critical roles in improving the performance of PSCs, especially flexible versions (Fig. 8).[46] The primary role of 4-HBA is to serve as a multifunctional additive that controls the growth of the perovskite film and enhances its final properties. It forms an *in situ* cross-linking network that acts as a template or formwork for high-quality perovskite crystal growth, and significantly decreases grain boundary defects, lowers the film's residual stress, and reduces its Young's modulus, making it more flexible. The network introduces dynamic hydrogen bonds that give the perovskite film the ability to self-heal after mechanical damage. Unlike many insulating polymer additives, the 4-HBA network improves

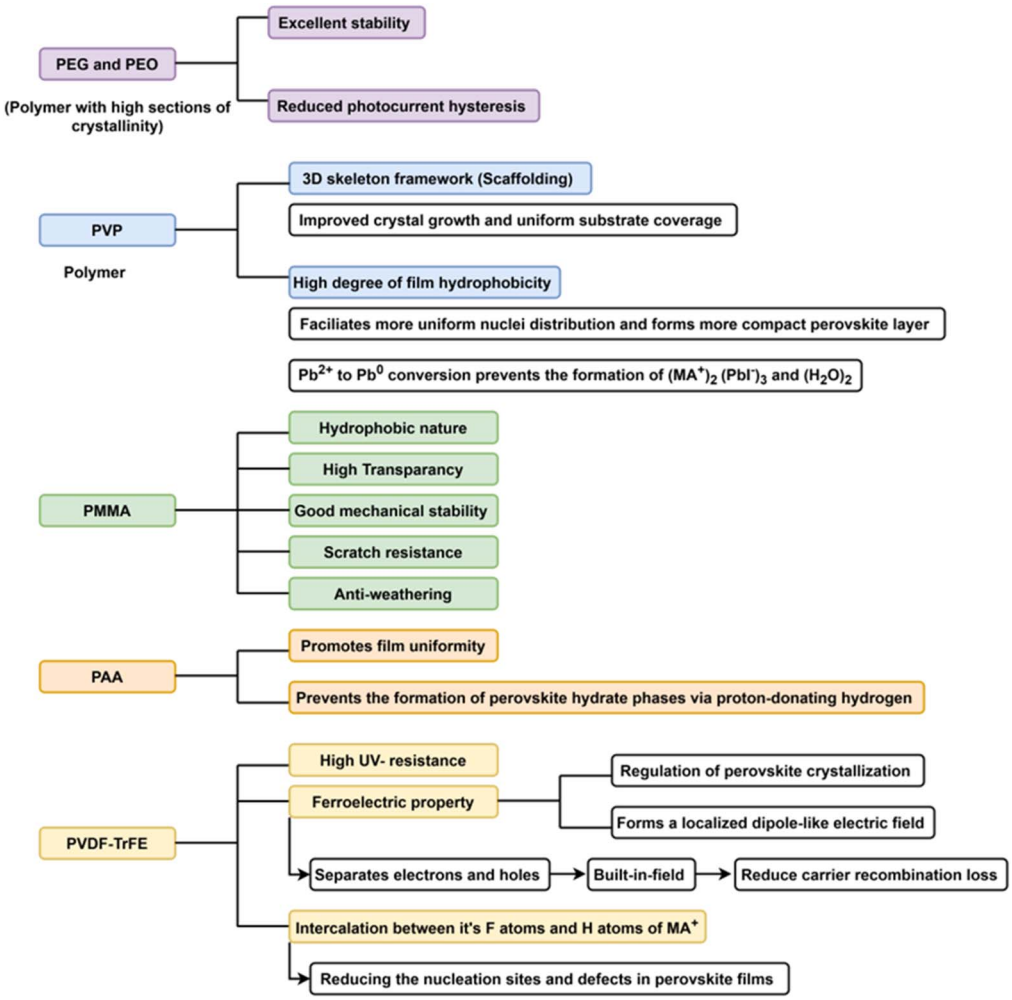

Fig. 7 The most widely used insulating polymers in perovskite structures.

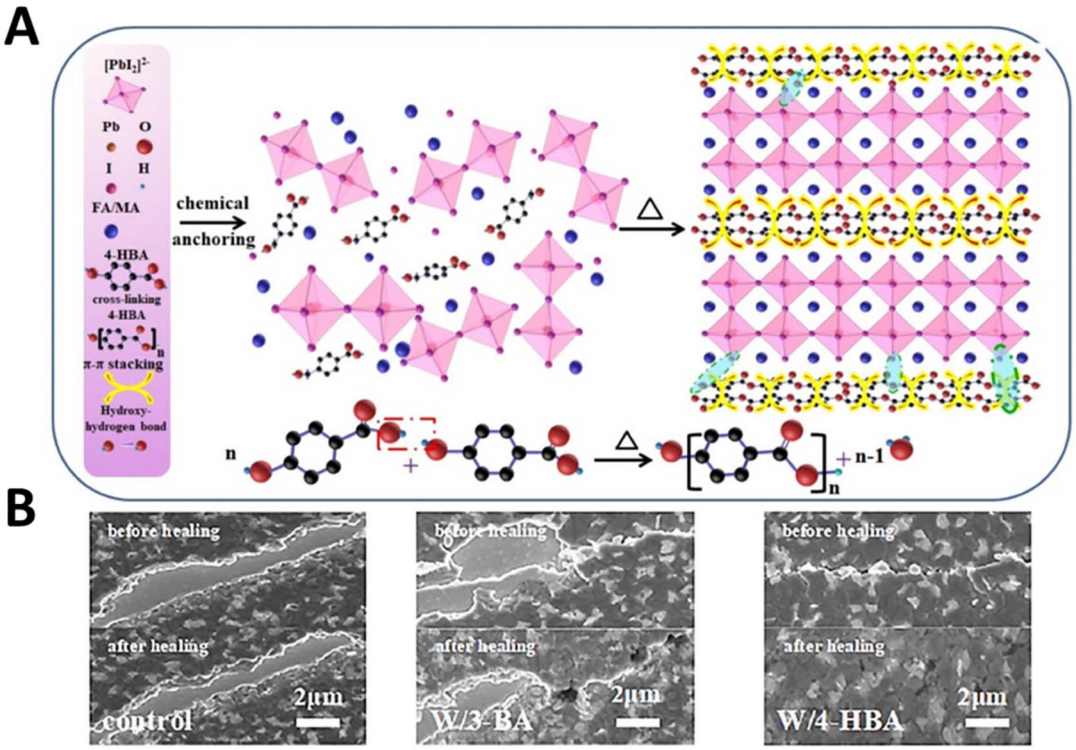

Fig. 8 (A) A schematic diagram that illustrates how the 4-hydroxybenzoic acid (4-HBA) crosslinking agent interacts with perovskite precursors to form a high-quality film, compared to the standard process. The C═O/C–O groups in 4-HBA form coordination bonds with lead (Pb^{2+}) ions, while the hydroxyl (–OH) groups form hydrogen bonds with iodide (I^-) ions. This anchors the agent directly to the perovskite components. The benzene rings of the 4-HBA molecules interact with each other (π–π stacking) and with Pb^{2+} ions (electrostatic interaction), which helps enhance the film's electrical conductivity. (B) These three figures are a series of SEM images that visually demonstrate the mechanical resilience and remarkable self-healing properties of the perovskite film modified with 4-HBA after being subjected to extreme stress. For this test, the films were bent 4000 times at a tight radius of 2 mm. The left picture (control film): the "before healing" image shows that the standard perovskite film suffers from severe, widespread cracks after bending. The "after healing" image is identical, showing that the film has no ability to self-heal. The middle picture (3-BA modified film): this film, modified with a similar but non-crosslinking molecule, also exhibits serious cracks from the stress and shows no self-healing. The right picture (4-HBA modified film): this film is far more robust. The "before healing" image shows only slight, minor cracks after the same intense bending. Most importantly, the "after healing" image reveals that after a mild heat treatment (60 °C for 1 hour), the cracks have completely disappeared. Reproduced with permission from Yankun Yang, *et al.*, *Advanced Science*, 2025, Wiley.[46]

charge transport and extraction, avoiding the issue of electrical insulation. The hydrophobic nature of 4-HBA enhances the perovskite film's resistance to environmental factors like humidity. The process by which 4-HBA improves the perovskite film occurs in distinct stages during fabrication and operation. During the mild heating in the annealing stage (*e.g.*, 100 °C for 30 min), 4-HBA molecules undergo an esterification reaction, causing them to crosslink with each other. This creates a network of oligomers with an average chain length of about seven units, held together by both covalent ester bonds and intermolecular hydrogen bonds. This network provides an excellent scaffold for the perovskite to grow on. Before and during crystallization, the functional groups on 4-HBA interact strongly with the perovskite precursors. The carbon-oxygen double bond (C═O) forms a coordination bond with uncoordinated Pb^{2+} ions. This strong interaction limits the number of excessive perovskite nucleation sites and prolongs the overall crystallization process. By slowing down and controlling the crystal growth, this method allows for the formation of a high-quality perovskite film with significantly larger grains (average size of 937 nm *vs.* 584 nm for the control) and fewer defects.

After the film is formed, the 4-HBA network remains at the grain boundaries, acting as a flexible bridge that connects the rigid perovskite grains. This helps to release residual lattice stress and significantly lowers the film's Young's modulus, making it much more robust against bending and stretching. The network is rich in dynamic hydrogen bonds. When the film is bent and cracks appear, these bonds can break and then rapidly reform with mild heat treatment (*e.g.*, 60 °C), allowing the cracks to heal and the device to recover up to 89% of its original efficiency. The benzene ring in 4-HBA has an electrostatic interaction with Pb^{2+} ions, and the molecules can arrange to allow for π–π stacking. This creates effective channels for charge extraction and transport, overcoming the insulation problem often caused by other polymer additives. The efficiency of rigid PSCs reached 24.76%, while FPSCs achieved 22.73%, and the PSCs retained 91% of their initial efficiency after 10 000 bending cycles at a 5 mm radius.

Developing complex polymers with three-dimensional (3D) structures and multiple functional groups is a current trend for addressing deep-level traps in various perovskites. One efficient approach is multi-mode passivation. In a study,[47] a singular functional group within the polyethyleneimine (PEI) family matrix with various configurations and protonation states was used. The *in situ* protonation process reduced deep-level traps for minority carriers. The research emphasized the importance of primary amine branches with moderate density for optimal passivation effects, highlighting the limitations of traditional protonation methods in addressing carrier traps. The protonation process of perovskite/PEI fundamentally differs from physisorption or metal-chelation mechanisms. The study employed deep-level transient spectroscopy (DLTS) to investigate variations in the properties of deep-level traps, such as trap category, energy level, carrier lifetime, and cross-section area of captured charges (Fig. 9). The p–i–n device structure consists of ITO/PTAA/perovskite/PEIE/C_{60}/BCP/Ag, with the hole carrier acting as the minority carrier at the perovskite/PEIE junction. The DLTS spectra are illustrated through the linear fitting of DLTS peaks, and the energetic positions of these traps were deduced from the Arrhenius plot. In devices lacking the PEIE layer, two p-type deep-level traps for hole carriers were detected at energy levels of 0.61 and 0.73 eV above the valence band maximum. In contrast, a single p-type trap was identified in devices with the PEIE layer, located at an energy level 0.65 eV above the valence band maximum. The PEIE coating reduced trap density by a factor of ten compared to the standard device, significantly extending carrier lifetime. Another crucial trap parameter that impacts carrier density and distribution is the captured cross-section area. This research demonstrates that *in situ* protonation is essential for effective interface passivation. The presence of non-protonated PEIE molecules in excess PEIE significantly increases insulation, leading to noticeable decreases in J_{SC} and FF. Additionally, the reduction of the perovskite's work function is not the primary factor driving the performance improvement. Statistical analysis shows that the 15% increase in PCE of PEIE devices compared to control devices is mainly due to enhancements in V_{OC} and FF.

The J_{SC} remained unchanged, consistent with the overlap of external quantum efficiency (EQE) spectra. Furthermore, the diode ideality factor of the PEIE device (n = 1.03) showed significant improvement compared to the control device (n = 1.27), indicating reduced non-radiative recombination. PEIE devices exhibited remarkable shelf stability, maintaining their original performance when stored in an N_2 atmosphere for 5500 hours. Notably, the PEIE devices retained their initial PCE after aging at 85 °C for 1100 hours, in contrast to the control device

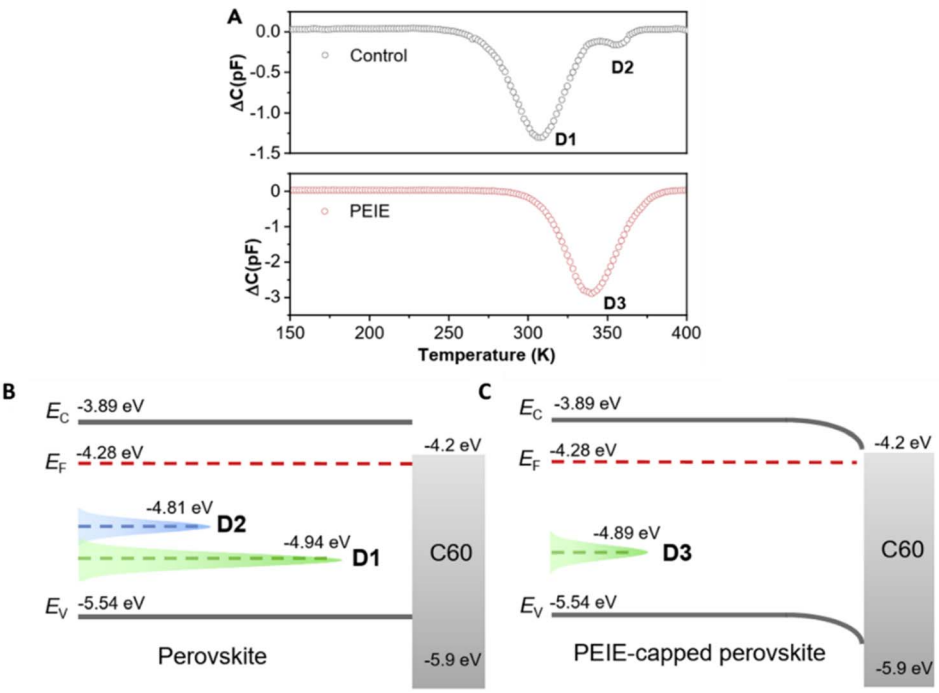

Fig. 9 (A) Deep-level transient spectroscopy (DLTS) measurements comparing unmodified perovskite (control, black curve) and PEIE-incorporated perovskite devices (red curve) reveal three distinct minority carrier trap states, denoted as D1, D2, and D3. The spectral analysis demonstrates significant differences in trap state signatures between the bare and surface-passivated perovskite samples. And comparative study of the energy band structure and deep-level trap states was conducted for both control (B) and PEIE-passivated (C) devices. The observed peaks in the trap density profiles correspond to distinct defect states (D1, D2, and D3), where their spectral positions indicate trap depths and their amplitudes reflect relative trap densities. Key electronic parameters—including the conduction band minimum (EC), valence band maximum (EV), and Fermi level (EF)—were experimentally determined through ultraviolet photoelectron spectroscopy (UPS) measurements. This analytical approach provides critical insights into how PEIE passivation modifies the energetic landscape of the devices. Reproduced with permission from Zhu *et al., Joule*, 2022, Cell Press journal.[47]

without PEIE passivation, which experienced a 10% reduction in PCE.

Li *et al.*[48] developed a multifunctional fluorinated additive, capable of polymerizing through hydrogen bonds to control the intermediate phase and influence the preferred orientation of crystal growth. This additive, known as FTPA, was applied individually or simultaneously to the bulk and surface of various cell structures and perovskite compositions (Fig. 10). The FTPA additive includes delocalized aromaticity for charge carrier regulation, fluorine to stabilize the intermediate phase, and vinyl groups for *in situ* polymerization, which fills grain boundaries in the perovskite. By leveraging the chemical interactions of FTPA's functional groups with solution components, they effectively managed nucleation and crystallization, achieving a PCE of 24.10% (from 22.48%), with a V_{OC} of 1.182 V and a FF of 83.45% for the top-performing planar $FA_{0.95}MA_{0.05}Pb(I_{0.95}Br_{0.05})_3$-based PSC. This PSC showed significant operational stability, maintaining over 95% of its initial efficiency after 1000 hours of continuous sunlight exposure and 2000 hours in ambient air with ~50% humidity. A known issue with formamidinium lead iodide ($FAPbI_3$) perovskite is the instability of the α-black-phase, which easily converts to the δ-yellow-phase. In this study, the unsealed FTPA-incorporated perovskite film retained the black phase for more than 5 minutes of immersion in water due to the FTPA network preventing water molecule penetration.

In another study, the careful design of an elastomer-like polymer with consistent *in situ* polymerization during perovskite crystal growth led to significant improvements in both PCE and mechanical stability for flexible PSCs. Wu *et al.*[49] demonstrated that incorporating bis((3-methyloxetan-3-yl) methyl)thiophene-2,5-dicarboxylate (OETC) into the PbI_2 solution and subsequent deposition created a mesoporous PbI_2 scaffold with fewer nucleation sites, allowing cations to penetrate the PbI_2 network and form large perovskite grains with a preferential (100) crystal orientation (Fig. 11). Additionally, polymer residues in the grain boundaries impart flexibility to the perovskite layer and increase Young's modulus. Consequently, PCEs of 23.4% and 21.1% were achieved for flexible PSCs with active areas of 0.062 cm^2 and 1.004 cm^2, respectively, demonstrating the ability to relieve mechanical stress through the flexibility of the perovskite film.

In a study, researchers used Rb-functionalized poly(acrylic acid) (Rb-PAA) as a multifunctional alkali-functionalized polymer to control the crystallization of $FAPbI_3$ perovskite films. The synthesis of the Rb-PAA complex involves a simple acid–base neutralization reaction between Rb_2CO_3 and PAA (poly(acrylic acid)), resulting in Rb-PAA held together by ionic interactions. When dissolved in chlorobenzene, these ionic interactions may weaken. During the anti-solvent dropping process, chlorobenzene removes DMF and DMSO from the wet perovskite films, ensuring even dispersion of the Rb-PAA complex within the film, which allows for further diffusion and distribution of Rb ions during post-annealing at 150 °C. However, due to the large size and steric hindrance of the PAA polymer, it primarily remains on the film's surface rather than penetrating the bulk. Small angle X-ray diffraction showed that the signals of excess PbI_2 in PAA and Rb-PAA treated films were significantly suppressed. SEM analysis revealed uniform films with compact textures and grain sizes in the hundreds of nanometers range, free of visible pinholes. Additionally, the Rb-PAA-treated film had a slightly larger average grain size (909 nm) compared to the control film (847 nm), similar to the PAA-treated film (907 nm), indicating fewer grain boundaries and defects. The UV-vis absorption spectra show absorption edges at around 800 nm, indicating a favorable light absorption range and suggesting that the optical properties (such as the optical bandgap) of the perovskite films remain unchanged after Rb-PAA and PAA

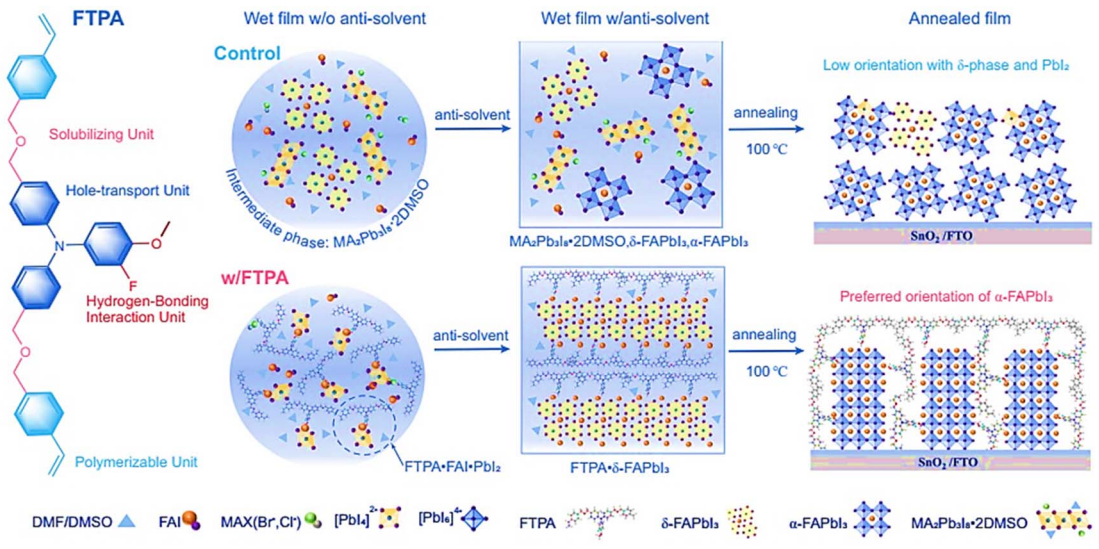

Fig. 10 The molecular structure design of FTPA, and schematic diagram of the possible phase evolution of the nucleation and crystallization of FA-based mixed anion perovskites ($FA_{0.95}MA_{0.05}Pb(I_{0.95}Br_{0.05})_3$) during the film-forming process with (w) or without (w/o) FTPA. Reproduced with permission from ref. 48. Reprinted from *Nature Communication*, Mubai Li, *et al.*, 2023, under CC BY license.

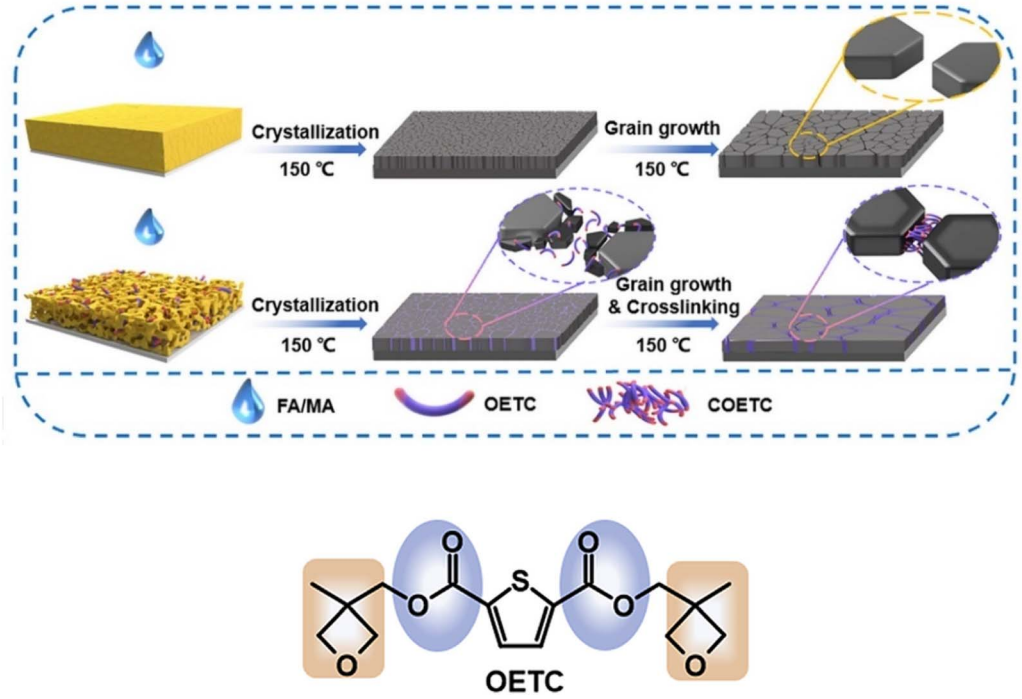

Fig. 11 Schematic of the *in situ* crosslinking-assisted grain growth process. Reproduced with permission from ref. 49. Reproduced with permission from Yeyong Wu, *et al.*, *Joule*, 2023, Cell.

treatments. This result implies that adding PAA does not affect the crystallization of perovskite, and Rb^+ does not integrate into the crystal lattice to form Rb-based perovskite, which would otherwise result in a wider bandgap structure. The PL spectra indicate that the emission intensity of films treated with Rb-PAA is about twice that of films treated only with PAA or left untreated, suggesting that Rb^+ doping effectively reduces defect density and minimizes non-radiative recombination. The recombination in time-resolved photoluminescence (TRPL) is mainly governed by first-order trap-assisted recombination. The fitted lifetime of perovskite films has significantly increased from 470 to 1059 ns due to the passivation effect of Rb^+ and PAA. The enhanced PL intensity and significantly extended charge carrier lifetime of the treated perovskite film are clearly due to the reduced defects. Additionally, the extended charge-carrier lifetime of the perovskite film treated with Rb^+ corresponds to the presence of micron-sized crystal grains with fewer grain boundaries, which act as recombination centers and charge carrier traps. The top-performing Rb-PAA polymer-treated device showed a PCE of 24.93% for the reverse scan, a PCE of 24.69% for the forward scan, and a stabilized efficiency of 24.74%. After 500 hours of operation, the PSC treated with Rb-PAA retained 83% of its initial efficiency, compared to 30 ± 5% for the PSC without Rb-PAA treatment.[50]

Table 1 lists the photovoltaic characteristics of perovskite solar cells that use more conventional polymers in their active layer.

Fig. 12 shows the PCE change after addition of polymers in the bulk perovskite according to Table 1.

3.2 Interface passivation by using polymers

High defect density on the surface of layers causes energetic reactivity, leading to moisture absorption and increased ion migration. Common solution-based coatings for polycrystalline perovskite limit the formation of high-quality layers with large grains.[93] Often small grains result in widespread grain boundaries, which are concentrated regions of voids and defects. Therefore, a crucial aspect of perovskite passivation focuses on morphology control and surface treatment. When the perovskite layer interfaces with CTLs, defect issues worsen, and recombination rates increase. Interface engineering is essential for providing an ideal substrate for subsequent layers, especially for perovskite crystallization. Additionally, lattice mismatch strain between layers occurs at the contacts. Perovskite films made through rapid low-temperature methods often have many interfacial defects. Compared to bulk defects, interfacial defects can be more harmful to device performance due to their much higher densities, leading to significant non-radiative recombination losses. These interfacial defects accelerate the degradation of PSCs and must be addressed to achieve industrial-scale production. Passivation approaches are categorized into top and buried interfacial methods based on their spatial positioning.[94,95]

3.2.1 Top interface approach. The top interface passivation approach is a strategy used to reduce defects at the interface between the perovskite layer and the overlying CTLs in perovskite solar cells. These defects can be caused by the release of volatile organic components during the thermal annealing process, which can lead to deficiencies in the coordination of lead or halide vacancies on the perovskite surface. To address

Table 1 Photovoltaic performance parameters of some PSCs integrating conventional polymeric components within the photoactive layer

Device	Polymer	Device structure	V_{OC} (V)	J_{SC} (mA cm^{-2})	FF (%)	PCE (%)	Ref.
1	EVA	ITO/NiO_x/$Cs_{0.1}FA_{0.7}MA_{0.2}PbI_xBr_{3-x}$:EVA/$PC_{61}BM$/BCP/Ag	1.06	22.39	81.0	19.31	51
2	PVA	FTO/TiO_2/$FA_xMA_{1-x}PbBr_yI_{3-y}$:PVA/spiro-OMeTAD/Au	1.07	22.14	72.69	17.22	52
3	PVB	FTO/TiO_2/$FA_xMA_{1-x}PbBr_yI_{3-y}$:PVB/spiro-OMeTAD/Au	1.09	23.09	75.89	19.10	52
4	4Tm	ITO/SnO_2/$Cs_{0.05}(FA_{0.87}MA_{0.13})_{0.95}Pb(I_{0.87}Br_{0.13})_3$:4Tm/spiro-OMeTAD/Au	1.17	23.79	79.05	22.06	53
5	F4TCNQ	ITO/SnO_2/PCBM/$Cs_{0.09}FA_{0.27}MA_{0.64}PbI_3$:F4TCNQ/P3HT/carbon	1.07	22.23	63.68	15.1	54
6	PTMA	FTO/TiO_2/$Cs_xFA_yMA_{1-x-y}PbBr_zI_{3-z}$/PTAA/Au	1.09	22.8	75.0	18.8	55
7	PECL	ITO/NiO_x/$Cs_{0.05}(MA_{0.15}FA_{0.85})_{0.95}Pb(I_{0.85}Br_{0.15})_3$:PECL/PCBM + C_{60}/BCP/Cr/Au	1.15	23.98	83.79	23.11	56
8	FTPA	FTO/SnO_2/$FA_{0.95}MA_{0.05}Pb(I_{0.95}Br_{0.05})_3$:FTPA/FTPA/spiro-OMeTAD/Au	1.18	24.43	83.45	24.10	57
9	PEG	FTO/TiO_2/$MAPbI_3$:PEG/spiro-OMeTAD/Au	0.98	22.5	72.0	16.00	58
10	Rb-PAA	FTO/c-TiO_2/m-TiO_2/$(FAPbI_3)_{0.97}(MAPbBr_3)_{0.03}$:Rb-PAA/spiro-OMeTAD/Au	1.18	25.42	82.8	24.93	59
11	poly[Se-MI][BF_4]	ITO/SnO_2/$MA_{0.08}FA_{0.92}PbI_3$:poly[Se-MI][BF_4]/PEAI/spiro-OMeTAD/Au	1.16	26.04	82.66	25.10	60
12	PAA	FTO/SnO_2/$FA_xMA_{1-x}PbBr_yCl_zI_{3-y-z}$:PAA/spiro-OMeTAD/Ag	1.16	25.20	82.46	24.19	61
13	D2	FTO/SnO_2/$Cs_{0.05}(MA_{0.17}FA_{0.83})_{0.95}Pb(I_{0.83}Br_{0.17})$:D2/spiro-OMeTAD/Au	1.12	18.3	74.0	15.1	62
14	D3	FTO/SnO_2/$Cs_{0.05}(MA_{0.17}FA_{0.83})_{0.95}Pb(I_{0.83}Br_{0.17})$:D3/spiro-OMeTAD/Au	1.07	18.2	74.0	14.4	62
15	PEI	ITO/PEDOT:PSS/$MAPbI_{3-x}Cl_x$:PEI/PCBM/LiF/Ag	0.97	22.63	64.4	14.07	63
16	PCDTBT	ITO/PEDOT:PSS/$MAPbI_xCl_{3-x}$:PCDTBT/PCBM/Bphen/Ag	0.94	21.71	77.0	15.76	64
17	PVP	ITO/NiO_x/$MAPbI_3$:PVP/$PC_{60}BM$/BCP/Ag	1.08	21.57	75.0	17.5	65
18	J71	FTO/TiO_2/$MAPbI_3$:J71/spiro-OMeTAD/Au	1.11	22.31	77.6	19.19	66
19	PPC	ITO/SnO_2/$MAPbI_3$:PPC/spiro-OMeTAD/Ag	1.13	22.81	77.8	20.06	67
20	PANI	FTO/TiO_2/$(FAPbI_3)_{0.85}(MAPbBr_3)_{0.15}$:PANI/spiro-OMeTAD/Au	1.10	22.50	77.13	19.09	68
21	F1	FTO/TiO_2/$MAPbI_3$:F1/spiro-OMeTAD/Au	1.09	20.7	73.0	16.41	69
22	F2	FTO/TiO_2/$MAPbI_3$:F2/spiro-OMeTAD/Au	1.06	17.8	76.0	15.07	69
23	F3	FTO/TiO_2/$MAPbI_3$:F3/spiro-OMeTAD/Au	1.07	18.5	78.0	16.37	69
24	PMMA-AM	FTO/c-TiO_2/SnO_2/$FA_{0.90}MA_{0.03}Cs_{0.07}Pb(I_{0.92}Br_{0.08})_3$/PMMA-AM/spiro-OMeTAD/Au	1.22	24.12	78.99	23.24	70
25	P–Si	ITO/SnO_2/PCBA-$(FAPbI_3)_x(MAPbBr_3)_{1-x}$:P–Si/spiro-OMeTAD/Au	1.13	25.1	77.0	21.5	71
26	PBAT	ITO/NiO_x/$Cs_xMA_yFA_{1-x-y}PbBr_zI_{3-z}$:PBAT/PCBM + C_{60}/BCP/Cr/Au	1.13	23.53	83.1	22.07	72
27	C_{60}-PU	FTO/SnO_2/$FAPbI_3$:C_{60}-PU/spiro-OMeTAD/Ag	1.15	22.44	82.66	21.36	73
28	PTB7	ITO/SnO_2/$Cs_{0.05}FA_{0.79}MA_{0.16}Pb(Br_{0.17}I_{0.83})_3$:PTB7/spiro-OMeTAD/Au	1.16	21.40	71.49	17.75	74
29	PBTI	ITO/Cu:NiO_x/CsFAMA perovskite:PBTI/PCBM/ZrAcac/Ag	1.13	22.91	79.8	20.67	75
30	PEA	FTO/TiO_2/$MAPbI_3$:PEA/spiro-OMeTAD/Au	1.08	22.89	76.3	18.87	76
31	PEA	ITO/SnO_2/$(FAPbI_3)_{1-x}(MAPbBr_3)_x$:PEA/spiro-OMeTAD/Au	1.15	24.42	76.94	21.60	76
32	PHIA	FTO/NiO_x/$MAPbI_3$:PHIA/PCBM/Rhodamine 101/Ag	1.07	23.92	78.40	20.17	77
33	N2200	FTO/TiO_2/$MAPbI_3$:N2200/spiro-OMeTAD/Au	1.05	22.4	76.0	17.9	78
34	F-N2200	FTO/TiO_2/$MAPbI_3$:F-N2200/spiro-OMeTAD/Au	1.06	22.7	76.0	18.4	78
35	PF-0	FTO/TiO_2/$MAPbI_3$:PF-0/spiro-OMeTAD/Au	1.07	22.8	75.0	18.1	78
36	PF-1	FTO/TiO_2/$MAPbI_3$:PF-1/spiro-OMeTAD/Au	1.08	22.8	76.0	18.7	78
37	MCE	ITO/SnO_2/$MAPbI_3$:MCE/spiro-OMeTAD/MoO_3/Ag	1.17	23.0	78.1	21.0	79
38	S-Polymer	FTO/c-TiO_2/m-TiO_2/$FA_{0.65}MA_{0.35}PbI_{3-x}Cl_x$:S-polymer/spiro-OMeTAD/Au	1.11	25.57	83.14	23.52	80
39	s-PU	PDMS/hc-PEDOT:PSS/PEDOT:PSS Al4083/$FA_xMA_{1-x}PbBr_yI_{3-y}$:s-PU/PCBM/PEI/hc-PEDOT:PSS/PDMS	1.09	22.34	78.65	19.15	81
40	PU-PMDS-IU	ITO/SnO_2/$MA_{0.25}FA_{0.75}PbCl_{0.6}I_{2.4}$:PU-PMDS-IU/spiro-OMeTAD/Au	1.15	25.34	79.5	23.25	82
41	P(VDF-TrFE)	FTO/TiO_2/$MAPbI_3$:P(VDF-TrFE)/spiro-OMeTAD/MoO_3/Ag	1.13	22.95	77.0	20.04	83
42	P(VDF-TrFE-CFE)	FTO/TiO_2/$MAPbI_3$:P(VDF-TrFE-CFE)/spiro-OMeTAD/MoO_3/Ag	1.13	22.84	75.0	19.14	83
43	P(VDF-TrFE-CTFE)	FTO/TiO_2/$MAPbI_3$:P(VDF-TrFE-CTFE)/spiro-OMeTAD/MoO_3/Ag	1.12	22.59	75.0	19.08	83
44	TET	PEN/ITO/PTAA/$Cs_xFA_yMA_{1-x-y}PbBr_zI_{3-z}$:TET/$C_{60}$/BCP/Cu	1.06	22.92	83.1	20.32	84
45	DI	ITO/SnO_2/FA_xMA_{1-x} PbI_3:DI/spiro-OMeTAD/Ag	1.14	24.9	80.8	23.0	85

Table 1 (*Contd.*)

Device	Polymer	Device structure	V_{OC} (V)	J_{SC} (mA cm^{-2})	FF (%)	PCE (%)	Ref.
46	β-FV2F	ITO/MeO-2PACz/$Cs_{0.05}(FA_{0.98}MA_{0.02})_{0.95}$ $Pb(I_{0.98}Br_{0.02})_3$:β-FV2F/$PC_{61}BM$/BCP/Ag	1.17	24.8	84.3	24.6	86
47							
48	TUEG3	Glass/ITO/PTAA/$MAPbI_3$:TUEG3/$PC_{61}BM$/BCP/Ag	1.10	20.61	76.7	17.42	87
49	TUEG3	PET/ITO/PTAA/$MAPbI_3$:TUEG3/$PC_{61}BM$/BCP/Ag	0.99	20.04	69.0	13.64	87
50	POSP	ITO/NiO_x/$Cs_xFA_yMA_{1-x-y}PbBr_zI_{3-z}$:POSP/PCBM + C_{60}/BCP/Cr/Au	1.14	23.56	84.8	22.74	88
51	PCL	Glass/ITO/PEDOT:PSS/$MAPbI_3$:PCL/$PC_{61}BM$/BCP/Ag	1.01	19.35	74.14	14.49	89
52	PS	ITO/TiO_2/$Cs_{0.05}FA_{0.81}MA_{0.14}PbI_{2.55}Br_{0.45}$:PS/spiro-OMeTAD/Au	1.15	21.5	85.0	21.0	90
53	PU	ITO/NiO_x/$MAPbI_3$:PU/PCBM/BCP/Ag	1.05	22.12	80.3	18.7	91
54	PMMA	ITO/NiO_x:PDA/$MAPbI_3$:PMMA/PCBM/BCP/Ag	1.07	22.97	82.0	20.12	92

this issue, various methods have been developed, including using halide salts to induce recrystallization or employing low-dimensional perovskite passivation layers to modify the perovskite surface.[96]

Also, the researchers developed a two-step method involving pre-polymerization and secondary polymerization.[97] In pre-polymerization, a solution of the monomer, such as acrylonitrile, is first heated for a short period (*e.g.*, 60 seconds) before being applied to the solar cell. This initial step forms low molecular weight (LMW) polyacrylonitrile, which is less volatile than the original monomer. In secondary polymerization, this LMW polymer solution is then spin-coated onto the perovskite film's surface and heated again. This second heating completes the polymerization process, creating a stable, thin (~3 nm) polymer network directly on the top interface. The resulting polyacrylonitrile layer passivates the perovskite surface through the formation of strong coordination bonds between its cyano groups (C≡N) and the uncoordinated Pb^{2+} defects. This top surface passivation significantly reduces defect density, which leads to enhanced photoluminescence, longer carrier lifetimes, and ultimately, a more efficient and stable solar cell with a higher open-circuit voltage.

3.2.2 Buried interface approach. Defects that accumulate at the buried interface cause non-radiative recombination, a process where charge carriers are lost as heat instead of being converted into electricity. This leads to a significant loss in the device's V_{OC} and overall PCE. The abundance of trap sites on the surfaces of CTLs can negatively affect perovskite crystal growth, interfacial charge transport, and overall device stability. Defects arise from several issues. Mismatches in the thermal expansion coefficients between the perovskite and the underlying layer can create stress and defects. Mismatched electrical properties can lead to poor contact, causing charge carriers to accumulate and recombine instead of being efficiently extracted. The rapid and sometimes non-uniform crystallization of the perovskite precursor can lead to a high density of defects at the interface. To optimize the buried interface, volatile organic additives are pre-buried in the charge transport layer, and multifunctional hybrid interfacial layers have been introduced. These methods effectively reduce trap densities at the buried interfaces, optimize interfacial charge transport, and significantly enhance device stability.[98] However, the buried interface is difficult to modify because it is formed during the deposition of the perovskite film, making it inaccessible for post-treatment.

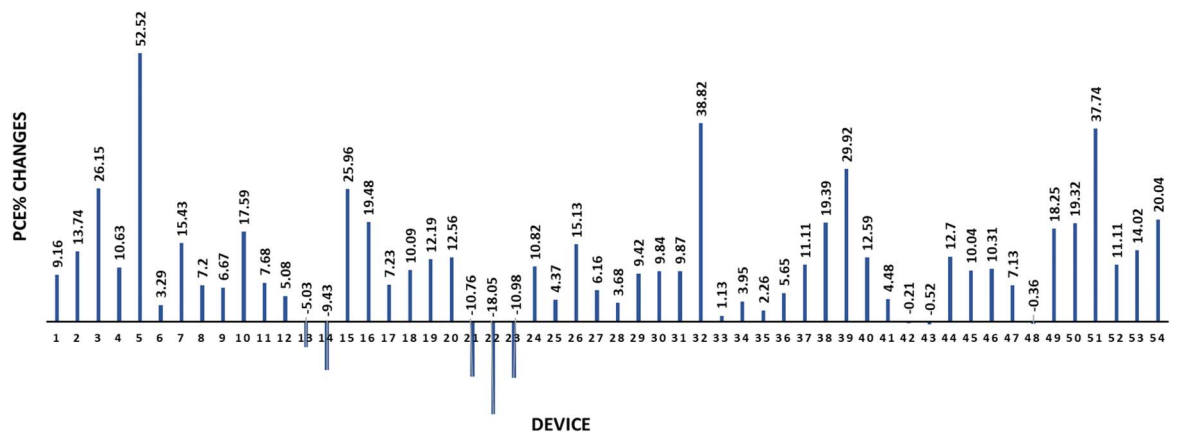

Fig. 12 Comparative analysis of PCE changes induced by selected conventional polymer integrations within the perovskite active layer, based on the device performance metrics presented in Table 1.

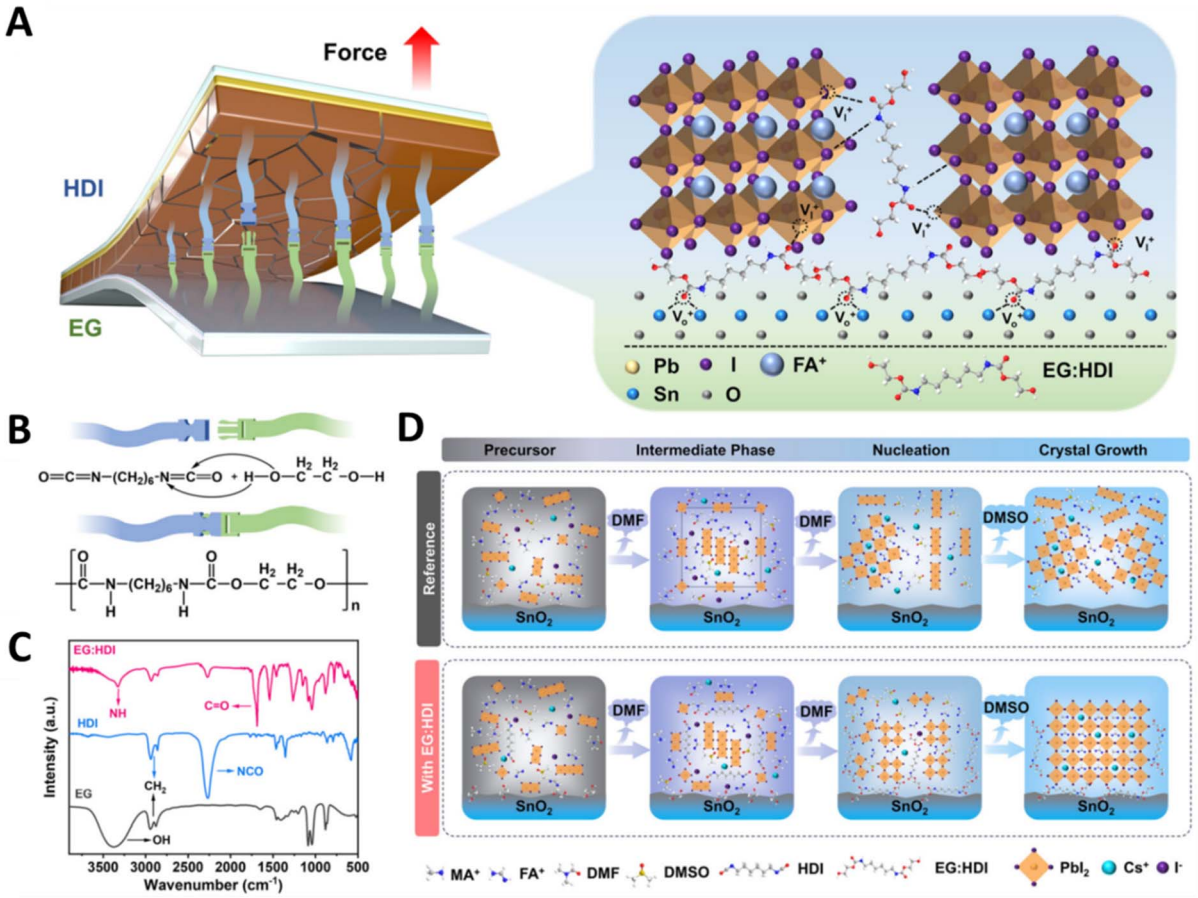

Fig. 13 The illustration of the buried interface fastening strategy. (A) A schematic of the strategy, where a polyurethane layer formed *in situ* fastens the SnO_2 electron transport layer to the perovskite film above it *via* hydrogen bonds. (B) Details of the chemical reaction mechanism between the two additives, hexamethylene diisocyanate (HDI) and ethylene glycol (EG), which form this polyurethane bridge. (C) The FTIR spectroscopy data as proof, confirming the reaction occurred by showing the new N–H and C=O bonds in the EG:HDI mixture. (D) A schematic showing how the HDI additive regulates the perovskite crystallization process, inhibiting complex intermediate phases and promoting oriented crystal growth for a higher-quality film.

Using polymers for this purpose offers unique advantages in improving both the chemical and mechanical properties of this interface. For instance, one strategy involves adding hexamethylene diisocyanate (HDI) to the perovskite precursor solution and coating the underlying ETL with ethylene glycol (EG).[99] During the annealing process, the HDI and EG react *in situ* to form polyurethane at the interface. The resulting polyurethane fastens the perovskite to the ETL through a network of hydrogen and coordination bonds. This strong adhesion improves the mechanical robustness of the device and mitigates residual stress in the perovskite film. The process also regulates crystallization by inhibiting the formation of complex intermediate phases, leading to a more uniform and higher-quality perovskite film (Fig. 13).

In another study,[100] a pre-existing polymer is coated on the CTL before the perovskite is deposited. A HMW PVP is used as a multifunctional interlayer at the buried interface. The functional groups on the polymer (*e.g.*, C=O in PVP) interact

Table 2 A comparison summary of the top and buried interface approach

	Top interfacial passivation	Buried interfacial passivation
Application timing	After perovskite formation	Before perovskite deposition
Main target	Surface defects	Bulk/interface defects
Processing method	Spin-coating, ALD,[a] and vapor-phase	SAMs,[b] interlayers, and substrate mod
Most impact on the device	Improves stability	Enhances charge transport
Limitations	May block charge extraction	Requires precise control

[a] ALD: atomic layer deposition. [b] SAM: self-assembled monolayers.

strongly with the ions in the perovskite precursor solution. Specifically, PVP forms hydrogen bonds with the ammonium cations (FA^+ and MA^+), creating polymer–ammonium intermediates. This interaction is stronger than that with lead ions and effectively slows down, or retards, the perovskite crystallization process. This slower, more controlled crystallization leads to a perovskite film with improved crystallinity and fewer defects. The polymer interlayer also helps create a better energy level alignment for more efficient charge extraction.

The key features of these two methods are summarised in Table 2. The most efficient PSCs often use both top and buried passivation. In this way a buried interface improves crystallization and charge extraction, and the top interface passivates surface defects and enhances stability.[101]

Common defect passivation methods involve pre- or post-treatment of the perovskite film using solvents or ammonium salts, which can lead to uncontrolled changes in film morphology or bulk crystal phase, complicating the preparation process and increasing costs. Consequently, *in situ* passivation of defects at dual interfaces during perovskite film preparation has become a research hotspot. This approach enhances device performance by reducing defect density at both interfaces and improving perovskite crystallization, resulting in higher crystalline quality and improved PCEs.[101]

Research has shown that using the fluorinated polymer poly(vinylidene fluoride) (PVDF) as an additive in spiro-OMeTAD is beneficial for PSCs.[102] PVDF copolymers have been effective in PSC development, serving as additives in perovskite films and materials for interface passivation. Specifically, P(VDF-TRFE) has demonstrated potential in enhancing PSC resilience when used as a passivation material at perovskite–transport layer interfaces. The hydrophobic nature of P(VDF-TRFE) as an additive to transport layers like spiro-OMeTAD is still to be explored. The composite of spiro-OMeTAD and PVDF improves HTL conductivity, reduces non-radiative recombination, and enhances FF and V_{OC} compared to a spiro-based HTL. PSCs with P(VDF-TRFE) achieve an efficiency of 24.1%, surpassing that of the control PSCs at 21.4%. Additionally, these PSCs show impressive ambient and operational stability, retaining over 90% of their initial efficiency after 45 days without encapsulation and maintaining 94% of their initial efficiency after 1080 hours under nitrogen conditions. The SEM images reveal that the control HTL material has voids, indicating poor film quality, which could lead to non-radiative recombination. In contrast, the target HTL material exhibits a uniform film morphology, suggesting better quality and potential performance improvements. Nyquist plots show lower series and transfer resistance values in the target PSC, indicating improved charge transfer and extraction mechanisms. The higher recombination resistance suggests reduced recombination at the perovskite–HTL interface, aligning with enhanced FF and V_{OC}. Dark *I–V* characteristics analysed using the SCLC model reveal smaller V_{TFL} values for hole-only devices in the target PSC compared to the control PSC.

Point defects such as surface under-coordinated lead cations and iodine (I) anions of the PbI_6^{-4} octahedron, ionic vacancies, interstitial ions, and anti-site defects are primary sources of non-radiative Shockley–Read–Hall recombination. This recombination results in the loss of V_{OC} and accelerates the decomposition of PSCs. The presence of both ester and amide groups aids in the coordination of Pb^{2+} ions at the interface and the anchoring of I^- ions, thus suppressing defects like interstitial I and Pb–I anti-site defects. In this context, a novel polymer, poly(methyl methacrylate-*co*-acrylamide) (PMMA-AM), was developed as an interfacial passivation layer. The interfacial passivation layer demonstrated exceptional stability during HTL deposition due to its limited solubility in chlorobenzene. This approach effectively mitigated defects in the perovskite layer, significantly increasing the V_{OC} of the device from 1.12 V to 1.22 V, achieving a PCE of 23.24%. Additionally, a PCE of 20.64% was attained for a large-area perovskite module (14 cm^2). The device modified with PMMA-AM also showed remarkable long-term stability, retaining 95% of its initial PCE after 1000 hours of continuous operation under illumination.[103]

In a study, the linear polymer heparin sodium (HS) is introduced as a multifunctional heterointerface bridge between the SnO_2 ETL and the perovskite film in n–i–p solar cells[104] (Fig. 14). The long-chain structure of HS allows it to simultaneously interact with both layers, leading to a combination of chemical, electronic, and mechanical improvements. The HS polymer has multiple functional groups (COO^- and SO_3^-) and ions (Na^+) distributed along its backbone. These groups form robust chemical bonds that neutralize defects at the interface. The COO^- and SO_3^- groups form strong covalent coordination bonds with undercoordinated lead (Pb^{2+}) defects on the perovskite surface and with tin (Sn^{4+}) on the SnO_2 surface. The Na^+ ions interact with iodide, forming Na–I bonds that further passivate defects. This passivation is confirmed by a reduction in the trap density of the perovskite film. The HS layer optimizes the energy landscape for more efficient electron extraction. It raises the conduction band of the SnO_2 layer from −4.35 eV to −4.16 eV, creating a better energy level alignment with the perovskite film. The HS layer acts as a template for perovskite crystallization, resulting in films with larger grain sizes and improved crystallinity. The HS modification effectively alleviates the inherent tensile stress found in perovskite films, converting it to a minimal compressive stress. This reduction in mechanical strain is critical for long-term stability. The polymer acts as a molecular bridge that chemically bonds the ETL and perovskite layers together. This dramatically improves mechanical toughness, as demonstrated by the fracture energy, which more than doubled for the HS-modified interface compared to the control. The optimized interface results in a PCE of 26.61% for rigid devices (certified at 26.54%) and 25.23% for flexible devices. They retain 94.9% of their initial efficiency after 1800 hours of continuous operation under simulated sunlight. They maintain 95.2% of their initial PCE after being aged at 85 °C for 1800 hours. Flexible devices retain over 95.5% of their efficiency after 1000 bending cycles.

Hyperbranched polymers (HBPs) are unique polymers with a 3D branched molecular structure, numerous functional end groups, and nanometer-scale intramolecular voids.[105] By manipulating their molecular configuration and functional end groups, the physical and chemical properties of HBPs can be

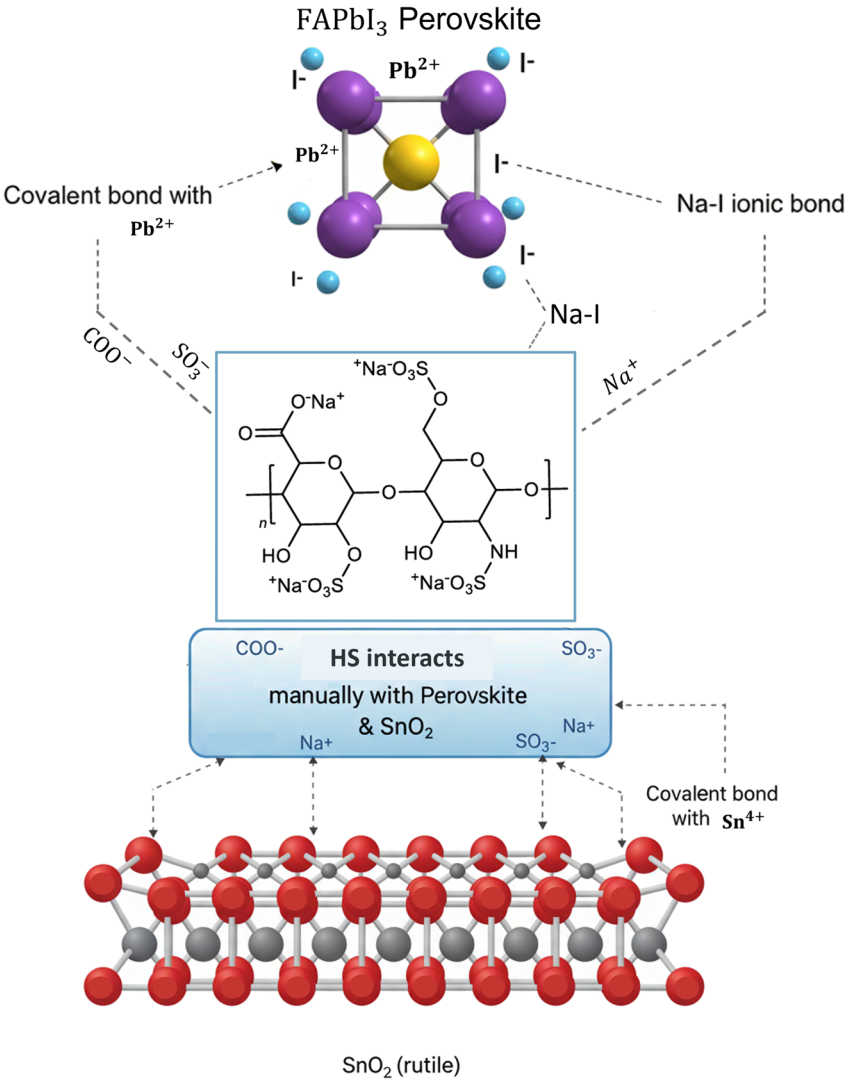

Fig. 14 The explanation of the mechanism and impact of using an HS polymer as a bridge at the interface between the tin oxide SnO_2 ETL and the perovskite film. A schematic that illustrates the core concept of the "heterointerface bridge". The long-chain HS polymer is shown sandwiched between the SnO_2 and perovskite layers. Its structure contains functional groups and ions (COO^-, SO_3^-, and Na^+) that are distributed along its backbone, allowing it to form robust chemical bonds with both the underlying SnO_2 and the overlying perovskite. This dual interaction serves to both physically connect the layers and chemically passivate interfacial defects. This results in the successful formation of the intended bridge layer. Redrawn based on concept reported in *Nature Photonics*, Xiaodan Tang, 2025, under CC BY license.[104]

precisely controlled. Incorporating complementary hydrogen bond donor and acceptor moieties within HBP branches creates an internal dynamic bonding network that absorbs mechanical energy and facilitates micro-fracture repair. The spherical shape and intramolecular voids of HBPs enhance branch mobility, enabling significant molecular deformation.[106] These unique structures give HBP materials exceptional mechanical strength and resilience. Furthermore, the polar end groups of HBPs can form strong interactions with other substances, providing excellent adhesive properties. As a result, elastic adhesive HBPs have gained significant interest as promising materials for reinforcing interfaces in various optoelectronic devices (Fig. 15).[105] HBPs with Pb^{2+} binding groups can be specifically designed to function as internal encapsulants, reducing lead leakage and creating a safer environment for daily use. A research study involved the synthesis of polyamide–amine-based HBPs with a range of branch lengths.[105] These HBPs are rich in amide, primary amine, secondary amine, and carboxyl groups on their spherical surface and within nanometer-scale cavities. These polar groups form strong hydrogen bonds with SnO_2 and perovskite, enhancing adhesion at the delicate ETL/perovskite interface. The flexible branches of HBPs allow them to rearrange hydrogen bond donors and acceptors, creating a dynamic, self-adjusting hydrogen bond network. The intramolecular cavities can also reorganize during bending, absorbing deformation energy. These features make HBPs excellent at damping and mitigating deformation energy, improving the mechanical resilience of flexible PSCs. This study found that rigid PSCs with HAD (hexane-diamine)–HBP modified SnO_2 achieved an impressive PCE of up to 25.05%. Flexible

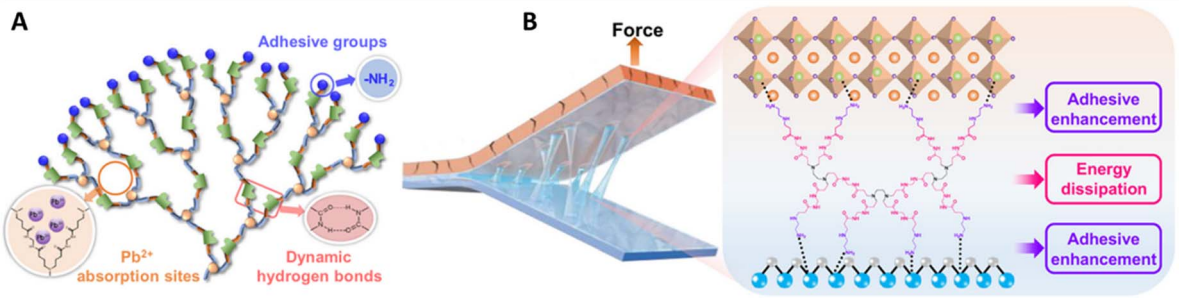

Fig. 15 Interfacial bonding mechanism of hyperbranched polymers (HBPs) as an adhesive layer between SnO_2 and perovskite layers. (A) Molecular architecture of HBPs. (B) Schematic illustration of HBP-mediated bonding at the SnO_2/perovskite interface.[105] Reprinted from *Nature Communication*, Zhihao Li, *et al.*, 2023, under CC BY license.

PSCs (1 cm^2) exhibited a PCE of up to 23.86% and demonstrated outstanding mechanical flexibility, retaining 88.9% of their initial PCE even after 10 000 bending cycles at a 3 mm radius. Furthermore, the carboxyl and amine groups within HBPs effectively interact with Pb^{2+}, significantly reducing the risk of lead leakage even if the flexible PSCs experience structural failure. To examine how chain flexibility affects the mechanical properties of HBPs, researchers utilized four different alkyl spacers with varying chain lengths. These HBPs were labeled as EDA (ethylenediamine)–HBPs, BDA (butanediamine)–HBPs, HDA–HBPs, and ODA (octanediamine)–HBPs, corresponding to ethylenediamine, 1,4-butanediamine, 1,6-hexanediamine, and 1,8-octanediamine derived HBPs, respectively. The polar $-NH_2$ terminal groups in HBPs can form high-density multiple hydrogen bonds with SnO_2 and perovskite layers, enhancing adhesion. The inter- and intramolecular hydrogen bond interactions involving –NH–, $-NH_2$, and C═O groups create a dynamic hydrogen bond network with strong mechanical properties, preventing crack propagation and increasing the toughness of the adhesive interface. HBPs with longer branches have a more relaxed structure, characterized by greater elasticity and flexibility. This is due to the extended aliphatic chains allowing ample single-bond rotation, reducing steric hindrance during synthesis, and resulting in a larger, more relaxed molecular configuration. Enhancing mechanical and adhesive properties in materials can be achieved by incorporating crystalline micro-domains in HDA–HBPs. Among the different HBPs tested, HDA–HBPs showed the best device performance, likely due to the strong interaction between the HBPs and adjacent SnO_2 and perovskite layers.

An HBP with dopamine adhesive (HPDA) is designed to enhance the mechanical durability of flexible perovskite solar cells (FPSCs), particularly under high humidity conditions.[107] The polymer's effects are inspired by marine mussels, which use dopamine groups to achieve strong adhesion in wet environments. The key to the polymer's success is its dopamine end-groups. Lap-shear tests show that HPDA maintains excellent adhesive strength even when washed with water, a feat that a control polymer without dopamine could not achieve (Fig. 16). Due to its 3D hyperbranched structure, the HPDA polymer

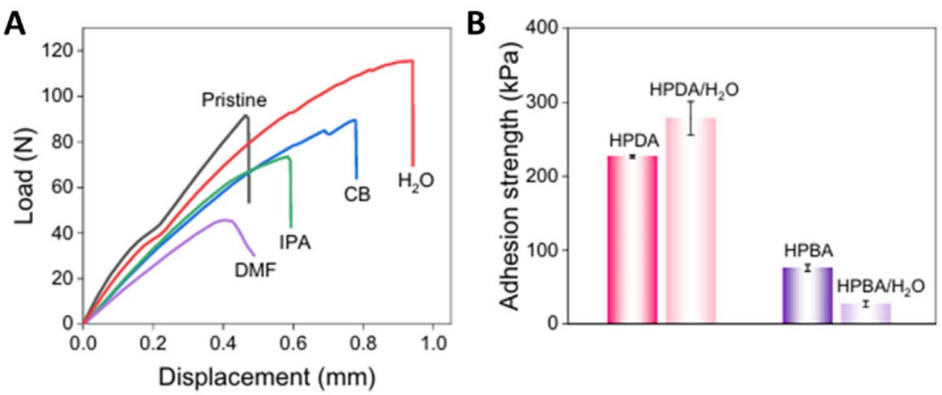

Fig. 16 (A) The results of a lap-shear test, which measures the force required to pull apart two ITO substrates that have been glued together with HPDA. The test was conducted in various solvent environments to simulate the conditions present during PSC fabrication and operation. The curves show that while solvents like DMF, IPA, and CB slightly reduce the polymer's adhesion, HPDA still maintains a decent bonding strength. Most importantly, the curve for water (H_2O) shows an excellent adhesive strength, comparable to the pristine (dry) condition. This demonstrates the polymer's remarkable ability to function effectively as an adhesive in a wet environment, a key feature inspired by marine mussels. (B) A bar chart to compare the underwater adhesion strength of HPDA with a control polymer, HPBA, which has a similar hyperbranched structure but lacks the critical dopamine end-groups. The results clearly show that after being washed with water, the adhesion strength of HPDA remains very high. This direct comparison proves that the dopamine terminal groups are essential for achieving strong underwater adhesion, highlighting the success of the bio-inspired design. Reprinted from nature communication, Z. Li, *et al.*, 2025, under CC BY license.[107]

forms a vertical scaffold that permeates the entire perovskite film. This scaffold physically connects the bottom ETL to the top HTL through the bulk of the perovskite. This internal scaffold acts as a reinforcement network, making the perovskite film significantly tougher. The fracture strength increases from 13.21 MPa to 43.73 MPa, and the fracture energy nearly doubles. Crucially, after aging in a humid environment, the control film loses ~80% of its fracture strength, while the HPDA-modified film loses only 10%. This prevents cracks from forming and propagating when the device is bent, especially in humid air. The HPDA scaffold effectively releases the residual tensile strain that typically builds up in perovskite films during crystallization. Measurements show a ~73% reduction in this strain, which helps to prevent the formation of micro-cracks that can degrade the device. The oxygen-containing functional groups in HPDA coordinate with and passivate uncoordinated Pb^{2+} defects within the perovskite grain boundaries. At the bottom interface, the dopamine's catechol groups form strong bidentate hydrogen bonds with the SnO_2 ETL. At the top interface, the benzene rings in the dopamine structure create π–π interactions with the spiro-OMeTAD HTL. The HPDA-modified flexible PSCs achieve a champion PCE of 24.43%. The polymer's strong affinity for lead ions also acts as a self-encapsulation mechanism, preventing 99% of lead leakage if the device is damaged.

Tables 3 and 4 show the photovoltaic characteristics of perovskite solar cells that use more conventional polymers in the ETL and the HTL, respectively. Fig. 17A and B show the PCE change after the addition of polymers in the ETL and HTL according to Tables 3 and 4, respectively.

Based on Fig. 17 the addition of PMMA and PEI in the TiO_2 and ZnO layers, respectively, has had an impressive effect on increasing the PCE of devices. On the other hand, the addition of the PEDOT:EVA in the ITO and also PASQ-IDT in the PTAA have had a good effect on increasing PCE.

The alignment of energy bands at the heterojunctions creates the built-in electric fields and energetic pathways that control all aspects of charge carrier dynamics. A fundamental understanding of these interfacial physics is therefore an essential prerequisite for designing high-efficiency devices. The optimization of the Conduction Band Offset (CBO) and Valence Band Offset (VBO) is a critical determinant of the power conversion efficiency in PSCs, as these offsets directly govern charge carrier transport and recombination dynamics at the interfaces. The alignment can be broadly categorized into two types, cliff and spike, each with distinct consequences for device performance.[147] A cliff alignment occurs when the energy level of the transport layer provides a downward step for the majority carrier. In contrast, a spike alignment presents a small energy barrier to the majority carrier. Research has shown that a moderate spike is highly beneficial for device performance. This small barrier does not significantly impede the forward extraction of majority carriers (*e.g.*, electrons into the ETL), but it serves two crucial functions. First, it effectively blocks the back-injection of electrons from the ETL into the perovskite. Second, and more importantly, it creates an energy barrier that repels minority carriers (*e.g.*, holes in the perovskite) from the interface, thereby suppressing interfacial recombination. However, the magnitude of the spike is critical.[148] The V_{OC} is fundamentally limited by recombination. Since interfacial recombination is a dominant loss mechanism in many PSCs, minimizing it is crucial for achieving high voltages. A moderate spike alignment at both the ETL and HTL interfaces is one of the most effective strategies for suppressing this recombination channel, thereby maximizing the achievable V_{OC}, and a defective interface with high recombination rates can lower shunt resistance and this leads to a reduced FF.[149]

Table 3 Photovoltaic performance parameters of some polymer-assisted electron transportation in perovskite–polymer hybrid solar cells

Device	Polymer	Device structure	V_{OC} (V)	J_{SC} (mA cm^{-2})	FF (%)	PCE (%)	Ref.
1	HP	ITO/SnO_2:HP/$Cs_{0.05}FA_{0.85}MA_{0.10}Pb(I_{0.97}Br_{0.03})_3$/spiro-OMeTAD/Au	1.162	25.0	79.2	23.03	108
2	PEI	ITO/ZnO:PEI/PCBM/$MAPbI_3$/spiro-OMeTAD/Ag	1.04	19.77	75.0	15.38	109
3	PEG	ITO/SnO_2:PEG/$Cs_{0.05}FA_{0.81}MA_{0.14}Pb_{2.55}IBr_{0.45}$/ spiro-OMeTAD/Au	1.12	22.67	81.9	20.8	110
4	PEGDA	ITO/SnO_2:PEGDA/$FAPbI_3$/spiro-OMeTAD/MoO_3/Ag	1.14	25.24	81.0	23.31	111
5	PVC	FTO/TiO_2/PVC/$MAPbI_3$/spiro-OMeTAD/AgAl	1.07	23.65	74.75	19.02	112
6	PMMA	FTO/c-In-TiO_2/m-TiO_2/PCBM:PMMA/$Cs_{0.07}Rb_{0.03}$ $FA_{0.765}MA_{0.135}PbI_{2.55}Br_{0.45}$/spiro-OMeTAD/Au	1.170	22.75	75.8	20.20	113
7	PY-IT	ITO/2PACz/$Cs_{0.05}(FA_{0.98}MA_{0.02})_{0.95}Pb(I_{0.98}Br_{0.02})_3$/ PY-IT/PCBM/BCP/Ag	1.15	24.37	84.0	23.57	114
8	F8TBT	FTO/PEDOT:PSS/$MAPbI_3$/$PC_{61}BM$:F8TBT/Ag	1.12	22.43	82.0	20.6	115
9	PMMA	ITO/c-TiO_2/TiO_2 nanorods/PMMA:PCBM/$Cs_{0.05}$ $FA_{0.88}MA_{0.07}PbI_{2.56}Br_{0.44}$/PMMA/P3HT:CuPc/Au	1.240	22.112	84.5	23.168	116
10	PN4N	ITO/SnO_2/PN4N/$CsPbI_2Br$/PDCBT/MoO_3/Ag	1.3	15.3	81.5	16.2	117
11	PMMA	FTO/TiO_2:PMMA/$MAPbI_3$/spiro-OMeTAD/Au	0.979	18.70	76.3	14.0	118
12	PFO	ITO/NiO_x/$MAPbI_3$/$PC_{61}BM$:PFO/BCP/Ag	1.03	16.3	64	10.8	119
13	F8BT	ITO/NiO_x/$MAPbI_3$/$PC_{61}BM$:F8BT/BCP/Ag	1.04	19.28	74.7	15.0	119
14	Parylene C	FTO/NiMgLiO/$(Cs_{0.15}FA_{0.85})Pb(I_{0.95}Br_{0.05})_3$/parylene C/PCBM/BCP/Ag	1.130	23.30	82.80	21.81	120
15	PFNOX	ITO/PEDOT:PSS/$MAPbCl_{3-x}I_x$/$PC_{61}BM$:PFNOX/Ag	0.94	20.4	72.9	14.0	121

Table 4 Photovoltaic performance parameters of some polymer-assisted hole transportation in perovskite–polymer hybrid solar cells

Device	Polymer	Device structure	V_{OC} (V)	J_{SC} (mA cm^{-2})	FF (%)	PCE (%)	Ref.
1	PTAA	ITO/TiO_2–Cl/$Cs_{0.05}MA_{0.05}FA_{0.9}PbI_{2.85}Br_{0.15}$/PTAA/spiro-OMeTAD/Au	1.126	23.2	79.8	20.9	122
2	PTPD	ITO/TiO_2–Cl/$Cs_{0.05}MA_{0.05}FA_{0.9}PbI_{2.85}Br_{0.15}$/PTPD/spiro-OMeTAD/Au	1.137	23.1	83.2	21.9	122
3	polyTPD	FTO/c-SnO_2/$FA_{0.85}MA_{0.15}Pb(I_{0.85}Br_{0.15})_3$/polyTPD/spiro-OMeTAD/Au	1.167	23.3	79.0	21.37	123
4	P3	ITO/SnO_2/PCBA/$MAPbI_3$/P3/MoO_3/Ag	1.080	20.9	77.0	17.4	124
5	2DP-F	ITO/SnO_2/*p*-FPhFA-incorporated $MA_{0.16F}A_{0.84}PbI_3$/2DP-F/spiro-OMeTAD/MoO_3/Ag	1.162	24.95	80.40	23.31	125
6	2DP-O	ITO/SnO_2/*p*-FPhFA-incorporated $MA_{0.16F}A_{0.84}PbI_3$/2DP-O/spiro-OMeTAD/MoO_3/Ag	1.184	24.91	81.60	24.08	125
7	PCDTBT	FTO/TiO_2/$MAPbI_3$/p-DTS($FBTTh_2$)$_2$:PCDTBT/Au	1.1	20.6	79.4	18.0	126
8	PTAA	ITO/NPB:PTAA/$MAPbI_3$/$PC_{61}BM$/Al	1.06	20.80	80.72	17.79	127
9	PVDF-HFP	ITO/TiO_2–Cl/$Cs_{0.05}MA_{0.05}FA_{0.9}PbI_{2.85}Br_{0.15}$/PVDF-HFP/spiro-OMeTAD/Au	1.131	22.4	79.3	20.1	122
10	PVA	ITO/SnO_2/$FA_yMA_{1-y}PbCl_xBr_zI_{3-x-z}$/PVA/spiro-OMeTAD/Au	1.149	25.24	80.0	23.20	128
11	PEG	ITO/SnO_2/$FA_yMA_{1-y}PbCl_xBr_zI_{3-x-z}$/PEG/spiro-OMeTAD/Au	1.126	24.94	79.6	22.35	128
12	PVK	ITO/SnO_2/$FA_yMA_{1-y}PbCl_xBr_zI_{3-x-z}$/PVK/spiro-OMeTAD/Au	1.106	25.27	78.6	21.97	128
13	PS	ITO/PTAA:F4-TCNQ/PS/$MAPbI_3$/PCBM/Bphen/Al	1.11	23.58	76.7	20.09	129
14	PMMA	ITO/poly-TPD:F4-TCNQ/PMMA/$MAPbI_3$/PCBM/Bphen/Al	1.11	23.52	76.8	20.12	129
15	PS	FTO/c-TiO_2 + m-TiO_2/$Cs_{0.05}(FA_{0.83}MA_{0.17})_{0.95}Pb(I_{0.83}Br_{0.17})_3$/PS/spiro-OMeTAD/Ag	1.158	22.32	79.2	20.46	130
16	PFN-I	ITO/poly-TPD/PFN-I (double layer)/$Cs_{0.05}FA_{0.79}MA_{0.16}PbI_{2.4}Br_{0.6}$/PCBM/BCP/Ag	1.13	22.47	81.0	20.47	131
17	PTQ10	ITO/SnO_2/$FAPbI_3$/PTQ10/PTAA/Ag	1.12	23.15	81.57	21.21	132
18	PVBI-TFSI	FTO/c-TiO_2/mp-TiO_2/$K_{0.05}(MA_{0.15}FA_{0.85})_{0.95}PbI_{2.55}Br_{0.45}$/spiro-OMeTAD:PVBI-TFSI/Au	1.16	22.99	76.0	20.33	133
19	BNo-F	ITO/BNo-F/$MAPbI_3$/PCBM/BCP/Ag	1.065	22.31	80.2	19.07	134
20	p-NP-E	FTO/c-TiO_2/m-TiO_2/$Cs_xFA_yMA_{1-x-y}PbBr_zI_{3-z}$/p-NP-E/Au	1.130	24.5	78.3	21.7	135
21	PBDB-O	ITO/SnO_2/$Cs_xFA_yMA_{1-x-y}PbBr_zI_{3-z}$/PBDB-O/$MoO_3$/Ag	1.072	16.98	56.24	10.23	136
22	PBDB-T	ITO/SnO_2/$Cs_xFA_yMA_{1-x-y}PbBr_zI_{3-z}$/PBDB-T/$MoO_3$/Ag	1.122	22.75	74.70	19.07	136
23	PBDB-Cz	ITO/SnO_2/$Cs_xFA_yMA_{1-x-y}PbBr_zI_{3-z}$/PBDB-Cz/$MoO_3$/Ag	1.144	24.41	79.03	22.06	136
24	Asy-PSeDTS	FTO/TiO_2/$CsPbI_3$ PQDs/Asy-PSeDTS/MoO_x/Ag	1.25	15.8	77.0	15.2	137
25	PTAA-P1	ITO/PTAA-P1/$Cs_{0.05}(FA_{0.98}MA_{0.02})_{0.95}Pb(I_{0.98}Br_{0.02})_3$/$C_{60}$/bathocuproine/Ag	1.17	25.50	83.28	24.89	138
26	PFBTI	ITO/SnO_2/$Cs_{0.05}FA_{0.95}PbI_3$/PFBTI/MoO_3/Ag	1.16	24.6	80.8	23.1	139
27	RP33	FTO/SnO_2/$Cs_{0.05}(FA_{0.83}MA_{0.17})_{0.95}Pb(I_{0.83}Br_{0.17})_3$/RP33/Au	1.02	23.5	68.7	16.44	140
28	RP-OR	FTO/SnO_2/$Cs_{0.05}(FA_{0.83}MA_{0.17})_{0.95}Pb(I_{0.83}Br_{0.17})_3$/RP-OR/Au	1.14	22.9	72.7	19.06	140
29	CzAn	ITO/CzAn/$FA_{0.8}Cs_{0.2}Sn_{0.5}Pb_{0.5}I_3$/PMMA/$C_{60}$/BCP/Cu	0.870	32.64	79.62	22.61	141
30	TABT	ITO/SnO_2/$MAPbI_3$/Mes-TABT/Au	1.15	23.8	77.0	21.3	142
31	BNs	ITO/BNs/$MAPbI_3$/PCBM/BCP/Ag	1.099	21.75	79.6	19.03	134
32	BNs-F	ITO/BNs-F/$MAPbI_3$/PCBM/BCP/Ag	1.083	22.78	83.40	20.56	134
33	PEDOT:EVA	PET/ITO/PEDOT:EVA/$MA_xFA_{1-x}PbBr_yI_{3-y}$/PCBM:BCP/Ag	1.18	21.26	79.0	19.87	143
34	PEDOT:EVA	Glass/ITO/PEDOT:EVA/$MA_xFA_{1-x}PbBr_yI_{3-y}$/PCBM:BCP/Ag	1.18	22.91	82.0	22.16	143
35	PASQ-IDT	ITO/PTAA:PASQ-IDT/$MAPbI_{3-x}Cl_x$/C_{60}/BCP/Ag	1.14	22.41	82.47	21.07	144
36	PS	ITO/PTAA:PS/$MAPbI_3$(Cl)/PCBM/BCP/Ag	1.138	22.5	83.5	20.8	145
37	*m*-PFICZ	ITO/*m*-PFICZ/$Cs_{0.15}FA_{0.85}PbI_3$/PCBM/Bphen/Ag	1.062	24.21	77.30	19.87	146
38	*p*-PFICZ	ITO/*p*-PFICZ/$Cs_{0.15}FA_{0.85}PbI_3$/PCBM/Bphen/Ag	1.091	24.48	80.1	21.39	146
39	PBTI	ITO/SnO_2/$Cs_{0.05}FA_{0.95}PbI_3$/PBTI/MoO_3/Ag	1.14	24.7	80.4	22.6	139

In insulating polymers, the absence of π-conjugation results in a very large energy gap between the HOMO and LUMO, typically exceeding 4 eV. This wide bandgap makes these materials electrical insulators, or dielectrics. Instead, their utility in PSCs stems from their dielectric nature and chemical functionality, which allow them to serve as passive interfacial layers. Their primary role is not to transport charge but to mitigate performance losses by neutralizing defects and electrically isolating problematic regions of the perovskite film. The principal function of insulating polymers at the perovskite interface is to suppress non-radiative recombination by passivating defects. This is achieved through two distinct but complementary mechanisms that leverage both their chemical and physical properties. Chemical passivation targets molecular-level point defects, while physical passivation is driven by the mesoscopic topography of the film, suggesting that the optimal approach may depend on the dominant defect type in a given perovskite film.[150] The combined effect of

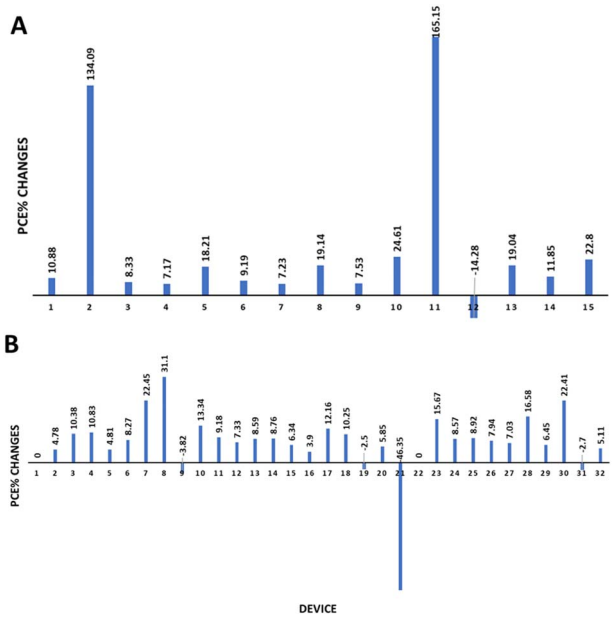

Fig. 17 Comparative analysis of PCE changes induced by selected conventional polymer integrations within the (A) ETL and (B) HTL, based on the device performance metrics presented in Tables 3 and 4, respectively.

chemical and physical passivation by insulating polymer interlayers leads to significant improvements in key photovoltaic parameters, primarily the V_{OC} and FF.[151] A crucial design parameter for this strategy is the thickness of the polymer layer. The layer must be sufficiently thin, ideally a sub-monolayer or monolayer, to allow charge carriers to efficiently tunnel through it to reach the adjacent CTL.

The primary role of conjugated polymers in PSCs is to function as active charge transport layers. They are designed to provide efficient, selective pathways for either holes or electrons to be extracted from the perovskite absorber and transported to the appropriate electrode. Many conjugated polymers exhibit high intrinsic charge carrier mobility, often surpassing that of commonly used small-molecule transport materials like spiro-OMeTAD, which is a significant advantage for minimizing transport losses.

The fundamental difference between insulating and semiconducting polymers at the interface lies in their mechanism of action. The former primarily acts by passivating defects, whereas the latter enhances the V_{OC} not only through defect passivation but also by facilitating efficient charge transport and improving the energy level alignment between the perovskite and the CTL.

4 Semiconducting polymers (SCPs)

SCPs or conjugated polymers are organic materials with π-electron delocalization along their backbone, enabling electrical conductivity while maintaining processability and flexibility. They bridge the gap between plastics and inorganic semiconductors.

4.1 Types of SCPs

SCPs are usually classified on two bases.

4.1.1 By structure

4.1.1.1 Linear conjugated polymers. They are a class of SCPs with a continuous, straight-chain backbone of alternating single and double bonds (π-conjugation). This conjugation allows delocalized π-electrons, enabling charge transport along the polymer chain. Some linear conjugated polymers are listed in Table 5.

4.1.1.2 Hyperbranched/dendritic conjugated polymers. They are highly branched, 3D macromolecules with unique structural and functional properties compared to linear polymers. Table 6 shows some important polymers in this category.

4.1.1.3 Donor–acceptor copolymers. They are a class of conjugated polymers engineered by alternating electron-rich (donor, D) and electron-deficient (acceptor, A) units along their backbone. This design enhances intramolecular charge transfer, enabling tunable electronic and optical properties for advanced organic electronics. Donor units (D) are typically aromatic or heterocyclic (*e.g.*, thiophene and carbazole). Acceptor units (A) are electron-withdrawing groups (*e.g.*, benzothiadiazole and diketopyrrolopyrrole (DPP)). Alternating the D–A–D–A sequence creates a "push–pull" effect, lowering the bandgap. The HOMO (donor) and LUMO (acceptor) levels can be adjusted by modifying D/A units, which enables absorption/emission across visible to near-infrared (NIR) spectra. Some key donor–acceptor (D–A) copolymers are listed in Table 7.

4.1.2 By function

4.1.2.1 p-Type (hole transport). They are organic semiconductors that primarily transport holes when doped or in a device. They are characterized by high-lying HOMO levels (typically −4.5 to −5.5 eV), facilitating hole injection. Table 8 shows some p-type conjugated polymers and their HOMO energies, and the chart in Fig. 18 illustrated some p-type conjugated polymers and their properties.

Table 5 Some linear conjugated polymers[152–154]

Polymer name	Bandgap (eV)	Charge mobility ($cm^2 V^{-1} s^{-1}$)	Primary applications
Polyacetylene (PA)	1.4–1.8	10^{-5}–10^{-1} (undoped–doped)	Early conductive polymers
Poly(3-hexylthiophene) (P3HT)	1.9–2.1	0.01–0.1 (hole)	OPVs and OFETs
Polypyrrole (PPy)	2.7–3.2	10^{-4}–10^{-1} (hole, doped)	Sensors and antistatic coatings
Poly(*p*-phenylene vinylene) (PPV)	2.4–2.5	10^{-5}–10^{-3} (hole)	OLEDs (green emission)
Polyfluorene (PFO)	2.8–3.2	10^{-3}–10^{-2} (hole)	Blue OLEDs and lasers
Polyaniline (PANI)	~3.5 (base)	10^{-2}–10^{0} (hole, doped)	Conductive films and corrosion protection
Polythiophene (PT)	2.0–2.2	10^{-5}–10^{-4} (hole)	OFETs and electrochromics
Polycarbazole (PCz)	~3.5 (PVK)	10^{-6}–10^{-5} (hole)	Perovskite solar cells and OLEDs

Table 6 Some main hyperbranched/dendritic conjugated polymers[155,156]

Polymer name	Structure type	Bandgap (eV)	Charge mobility ($cm^2 V^{-1} s^{-1}$)	Key properties	Primary applications
PAMAM dendrimers	Polyamidoamine (core–shell)	N/A	Insulating ($\sigma < 10^{-9}$)	High surface functionality	Drug delivery and gene therapy
Boltorn® hyperbranched polyester	Aliphatic polyester (random branches)	N/A	Insulating ($\sigma \sim 10^{-12}$)	Low viscosity and solubility	Coatings and adhesives
Conjugated dendrimers (*e.g.*, PPP-Ph)	Polyphenylene branches	2.5–3.0	10^{-4}–10^{-3} (hole)	Light-harvesting and energy transfer	OLEDs and sensors
Hyperbranched polythiophene (hb-PT)	Thiophene branches	1.8–2.2	10^{-3}–10^{-2} (hole)	High solubility and film-forming	OPVs and OFETs
Dendritic porphyrin polymers	Porphyrin core + conjugated arms	1.5–2.0	10^{-4}–10^{-3} (ambipolar)	Photocatalysis and NIR absorption	Photodynamic therapy and solar cells
Hyperbranched PPV (hb-PPV)	PPV with 3D branches	2.0–2.5	10^{-4}–10^{-3} (hole)	Enhanced light emission	LEDs and bioimaging
Carbazole dendrimers	Star-shaped carbazole cores	2.8–3.2	10^{-5}–10^{-4} (hole)	High triplet energy	Host materials in OLEDs
Dendritic triarylamines	Star-shaped triarylamine cores	2.5–3.0	10^{-3}–10^{-2} (hole)	Hole transport and thermal stability	OLED hole transport layers
Hyperbranched DPP polymers	DPP-core with conjugated arms	1.3–1.6	10^{-2}–10^{-1} (ambipolar)	Low bandgap and NIR absorption	OPVs and photodetectors

Table 7 Key donor–acceptor (D–A) copolymers[157,158]

Donor (D) unit	Acceptor (A) unit	Polymer name	Bandgap (eV)	Charge mobility ($cm^2 V^{-1} s^{-1}$)	Primary applications
Carbazole	Benzothiadiazole (BT)	PCDTBT	1.7–1.9	$\sim 10^{-3}$ (hole)	OPVs (PCE ~7%)
Cyclopentadithiophene (CPDT)	Benzothiadiazole (BT)	PCPDTBT	1.4–1.6	~0.1 (hole)	Low-bandgap OPVs
Fluorene	Benzothiadiazole (BT)	F8BT	2.1–2.3	$\sim 10^{-3}$ (ambipolar)	OLEDs (green emitter)
Dithienosilole (DTS)	Benzothiadiazole (BT)	PSBTBT	1.5–1.7	~0.1 (hole)	High-efficiency OPVs
Thienothiophene (TT)	Thiazolo[5,4-*d*]thiazole (TTz)	PTTz	1.3–1.5	~0.5 (hole)	NIR photodetectors
Benzodithiophene (BDT)	Thieno[3,4-*b*]thiophene (TT)	PTB7	1.6–1.8	$\sim 10^{-2}$–10^{-1} (hole)	OPVs (PCE ~9–10%)
Benzodithiophene (BDT)	Fluorinated thieno[3,4-*b*] thiophene	PTB7-Th	1.5–1.7	~0.1–0.2 (hole)	OPVs (PCE > 10%)
Indacenodithiophene (IDT)	DPP (diketopyrrolopyrrole)	PIDT-DPP	1.2–1.4	~1–5 (ambipolar)	OFETs and flexible electronics
Naphthodithiophene (NDT)	DPP	PNDT-DPP	1.3–1.5	~0.5–2 (hole)	High-mobility OFETs
Carbazole	Benzothiadiazole (BT)	PCDTBT1	1.8–2.0	$\sim 10^{-3}$ (hole)	OLEDs and OPVs
Thiophene	Quinoxaline	TQ1	~2.0	$\sim 10^{-2}$ (electron)	n-Type OFETs
Benzodithiophene (BDT)	Naphthalenediimide (NDI)	P(BDT-NDI)	1.4–1.6	~0.1–0.3 (electron)	All-polymer solar cells
Selenophene	DPP	PSeDPP	1.3–1.5	~0.5–1 (hole)	High-performance OFETs
Bithiophene	Isoindigo (IID)	PBTIID	1.5–1.7	~0.1–0.5 (ambipolar)	Flexible transistors and sensors
Dithienogermole (DTG)	DPP	PDTG-DPP	1.2–1.4	~1–3 (hole)	Stretchable electronics

4.1.2.2 n-Type (electron transport). They are organic semiconductors that primarily transport electrons. They are characterized by low-lying LUMO levels (typically −3.5 to −4.5 eV), facilitating electron injection, electron-deficient (acceptor) units in their backbone, and high electron affinity for stable charge transport. The chart in Fig. 19 illustrates some n-type conjugated polymers and their properties, and Table 9 shows some n-type conjugated polymers and their LUMO energies.

4.1.2.3 Ambipolar conjugated polymers. They are organic semiconductors that can transport both electrons and holes with comparable efficiency. These materials bridge the gap between p-type and n-type polymers, enabling complementary logic circuits and more efficient optoelectronic devices. Some of their main features include balanced charge transport so that they have similar hole (μ_h) and electron (μ_e) mobilities (typically 10^{-3}–10^{0} $cm^2 V^{-1} s^{-1}$) and LUMO levels and HOMO levels are placed around −3.5 to −4.2 eV and around −5.0 to −5.8 eV, respectively. Table 10 lists some ambipolar conjugated polymers and their hole and electron mobilities.

4.2 SCP role in perovskite hybrid solar cells

SCPs, with the potential to set energy bands, have unique electrical and optical features.[174] Therefore, they can passivate defects and also increase the carrier extraction, transportation, and light harvesting ability. The feasibility of extraction and transportation of carrier charges besides the suitable energy band levels and regulation of grain boundaries and size *via* highly delocalized conjugated polymers reduces the energy

Table 8 Some p-type conjugated polymers and their HOMO levels

Polymer	HOMO (eV)
Poly(3-hexylthiophene) (P3HT)	−4.9 to −5.2
Polypyrrole (PPy)	−4.9 to −5.2
Polyaniline (PANI)	−4.7 to −5.1
PBTTT (poly(2,5-bis(3-alkylthiophen-2-yl) thieno[3,2-*b*]thiophene))	−5.0 to −5.2
DPP-based polymers (*e.g.*, PDPP3T)	−5.1 to −5.3
IDT-BT (indacenodithiophene-benzothiadiazole)	−5.2 to −5.4
PTB7-Th	−5.2
PCDTBT	−5.5
PM6 (*e.g.*, PBDB-T-2F)	−5.4

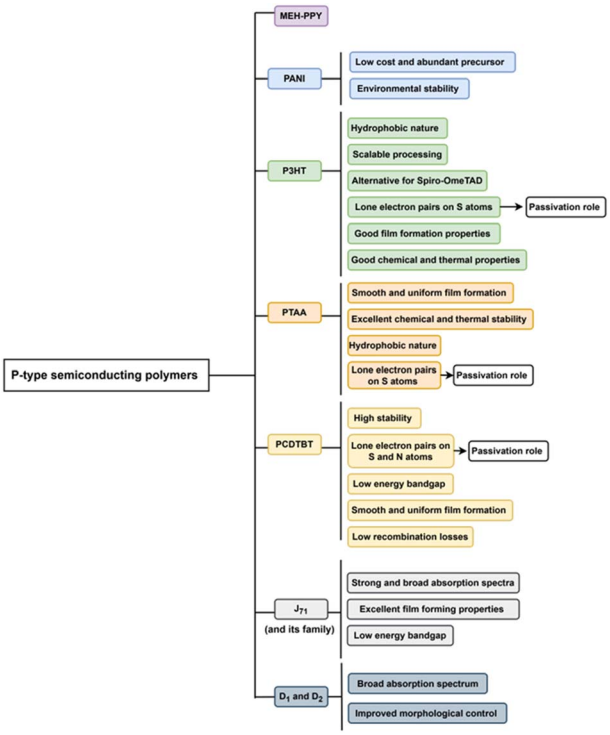

Fig. 18 Some important p-type conjugated polymers used in solar cells and their properties.[159–165]

losses significantly. In other words, SCPs can reduce energy losses in PSCs *via* four mechanisms. Improved charge transport reduces energy losses associated with charge recombination. Morphological control to enhance the crystallinity of perovskite films and reduce defect density subsequently lowers the recombination rate. Interfacial engineering to passivate the interfaces subsequently reduces trap-assisted recombination and improves charge extraction. And photon management can improve light absorption and minimize thermalization losses.[175] On the other hand, conducting polymers mostly are soluble in non-polar solvents and these solvents play the role of anti-solvents of a perovskite precursor. So, two mechanisms of rapid nucleation *via* anti-solvent pipetting and the slowing

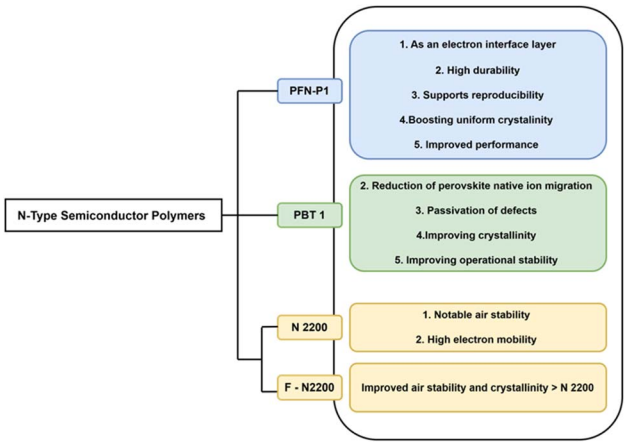

Fig. 19 Some important n-type conjugated polymers used in solar cells and their properties.[166–170]

Table 9 Some n-type conjugated polymers and their LUMO levels

Polymer	LUMO (eV)
Poly(benzimidazobenzophenanthroline) (BBL)	−4.3
Poly(perylene diimide) (PPDI)	−4.0
Poly(thiazole) (PTz)	−3.8
P(NDI2OD-T2) (N2200)	−4.0
P(PDI2OD-T2)	−3.9
PFT	−3.9
N2200	−4.0
PZ1	−3.7
P(NDI-T2)	−3.9 to −4.1

down of crystal growth *via* the presence of polymers in the precursor solution occur at the same time.

SCPs are used as charge transporting layers,[176,177] interfacial layers,[178] and additives[179,180] in perovskite solar cells. These polymers can be used as electron or hole transport materials. They facilitate the movement of charge carriers from the perovskite layer to the respective electrodes, which is essential for the conversion of light into electricity. Adjusting the LUMO level of SCPs with the LUMO level of the perovskite is necessary for polymer selection as a ETM, and suitable alignment of the HOMO level of the polymer with the HOMO level of the perovskite makes the polymer the HTM. The benefits of SCPs compared to traditional HTMs and ETMs are categorized in Fig. 20 and 21, respectively. In addition, they can act as interlayers between the active perovskite material and the charge-transporting layers. These polymer interlayers can improve the interface's electronic properties, leading to better charge extraction and reduced recombination. Also, polymers can be added to the perovskite layer to adjust its nucleation and crystallization processes. This can lead to improved film formation, increased grain size, reduced defects, enhanced charge transport, increased stability, and optoelectronic property tuning, which are beneficial for the device's efficiency and stability.

4.2.1 The backbone structures of SCPs. The backbone structures of SCPs used in perovskite solar cells can be categorized based on their chemical composition and the

Table 10 Some ambipolar conjugated polymers and their hole and electron mobilities[171–173]

Polymer	Structure	μ_h ($cm^2 V^{-1} s^{-1}$)	μ_e ($cm^2 V^{-1} s^{-1}$)
DPP-TT-T	Diketopyrrolopyrrole + terthiophene	0.1–1.3	0.05–0.8
PBTIID	Bithiophene + isoindigo	0.1–0.4	0.1–0.3
PCDTPT	Cyclopentadithiophene + pyridal thiadiazole	0.2–0.5	0.1–0.4

arrangement of their molecular units. Conjugated polythiophenes such as P3HT (poly(3-hexylthiophene)) have a backbone composed of thiophene rings. They are known for their good charge transport properties and are widely used in organic electronics. Polyphenylene derivatives include polymers like PPP (poly(*p*-phenylene)) and its derivatives, which have a backbone of benzene rings. They offer high thermal stability and good electronic properties.[181] Diketopyrrolopyrrole (DPP)-based polymers contain DPP units in their backbone and are known for their high charge carrier mobility and stability.[182] Naphthalene diimide (NDI)-based polymers have a backbone that includes naphthalene diimide units, providing high electron mobility and good environmental stability.[183] Helicene-based polymers as a recent addition to this category exhibit remarkable film-forming and hole transport properties, as well as exceptional thermal durability.[184,185] Each of these categories has unique properties that make them suitable for different applications within PSCs, such as active layers, or CTLs. The

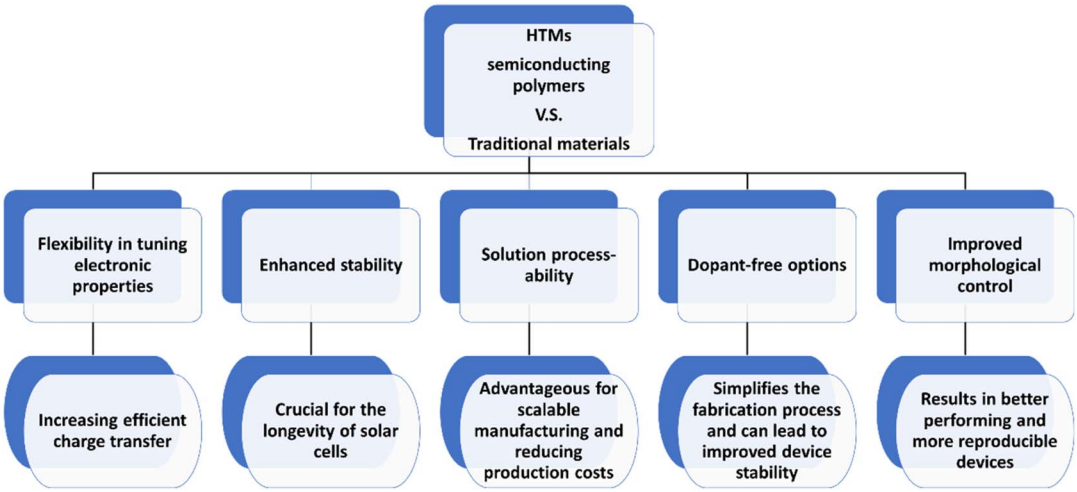

Fig. 20 Advantages of HTM SCPs relative to traditional HTMs.

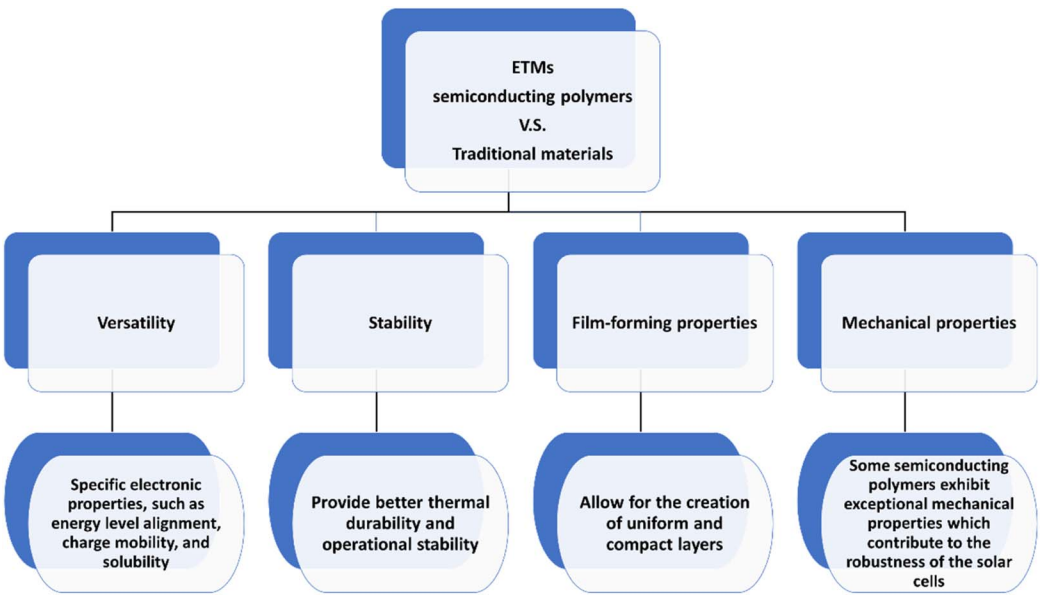

Fig. 21 Advantages of ETM SCPs relative to traditional ETMs.

Table 11 Conjugated polymers include alkyl side chains[196–199]

Side chain type	Example polymers	Impact on performance	Trade-offs
Linear alkyl (*e.g.*, $-C_6H_{13}$)	P3HT	Enhances π–π stacking	May reduce crystallinity if too long
Branched alkyl (*e.g.*, –2-ethylhexyl)	PTB7-Th	Prevents excessive aggregation	Can disrupt backbone packing
Short alkyl (*e.g.*, $-C_4H_9$)	P3BT	Promotes strong intermolecular ordering due to less steric hindrance	Limited solubility in many common organic solvents, making the polymer difficult to process

Table 12 Conjugated polymers include ether/alkoxy side chains

Side chain type	Example polymers	Impact on performance
Alkoxy (*e.g.*, $-OC_6H_{13}$)	PBDTTT-EFT	Improves donor–acceptor mixing
Ethylene glycol (*e.g.*, –OEG)	PEG-modified P3HT	Enhances water dispersibility (for eco-friendly processing)

Table 13 Conjugated polymers include fluorinated side chains[200,201]

Side chain type	Example polymers	Impact on performance
Fluoroalkyl (*e.g.*, $-CF_3$)	PTB7-Th (fluorinated BT)	Lowers HOMO and increases V_{OC}
Perfluoroarene (*e.g.*, $-C_6F_5$)	PF-based acceptors	Enhances air stability

Table 14 Conjugated polymers include siloxane side chains[202]

Side chain type	Example polymers	Impact on performance
Polydimethylsiloxane (PDMS)	PDMS-grafted DPP polymers	Improves mechanical flexibility

Table 15 Conjugated polymers include ionic side chains[203–205]

Side chain type	Example polymers	Impact on performance
Sulfonate ($-SO_3^-$)	P3HT-SO_3Na	Allows aqueous processing
Ammonium ($-NR_3^+$)	Cationic PF derivatives	Useful for layer-by-layer deposition

Table 16 Conjugated polymers include hybrid side chains[206,207]

Side chain type	Example polymers	Impact on performance
Oligoether-thiophene	p(g42T-T)	Balances solubility and ordering
Alkyl-phenyl	PffBT4T-2DT	Optimizes morphology in BHJs

choice of polymer is crucial for the overall performance and stability of the solar cell.

4.2.2 The side chains of SCPs. Side chains in SCPs play a multifaceted role in PSCs.[186,187] They can influence the polymer's solubility, film-forming ability, and the alignment of energy levels with the perovskite layer. Side chains can also impact the morphology of the active layer, charge carrier mobility, and overall device performance. For instance, side chains such as vinyloxy, allyloxy, and propargyloxy have been shown to improve hole mobility and match energy levels with the perovskite layer, which is essential for efficient device operation. Longer chains improve solubility but may reduce crystallinity. Branched chains prevent excessive aggregation. Additionally, side chains can be engineered to enhance the interfacial adhesion between layers, reduce charge recombination, and improve the environmental stability of the solar cells.[188] SCP side chains used in PSCs can be categorized based on their chemical structure and function. Alkyl side chains are the most common side chains used to improve the solubility and processability of polymers; examples include P3HT.[189] Aromatic side chains can enhance the electronic properties of polymers. For instance, phenyl-carbazole groups can be used for this purpose.[190] Redox-active side chains can participate in charge transfer processes. They can improve the reproducibility and stability of perovskite solar cells.[191–193] Functional side chains are designed to interact with the perovskite layer or to facilitate charge transport. For example, side chains terminated with vinyloxy, allyloxy, and propargyloxy have been shown to improve hole mobility.[194] Conformational side chains, and twisted or planar side chains can influence the packing and the charge transport properties of the polymer. Twisted triphenylamine (TPA) groups, for example, can favour interfacial charge transfer.[195] Each type of side chain can have a significant impact on the performance and stability of PSCs by influencing the polymer's physical and electronic interactions with the perovskite layer. Researchers continue to explore and optimize these side chains to enhance the efficiency and longevity of solar cells. Tables 11–16 categorize some important types of side chains of SCPs applicable in solar cells.

The structures of some SCPs are illustrated in Fig. 22.

4.2.3 The radius of gyration and Kuhn length of SCPs. The radius of gyration (R_g) and Kuhn length (L_k) are important parameters that describe the physical properties of SCPs, which can influence the performance of PSCs.[208,209] The R_g measures the distribution of the constituent atoms around the center of mass of a polymer molecule. In PSCs, a larger R_g typically indicates a more extended polymer chain, which can lead to better overlap between the electronic orbitals of adjacent chains. This improved orbital overlap can enhance charge transport properties, which is beneficial for the efficiency of solar cells.[210] The L_k is a measure of the stiffness of a polymer

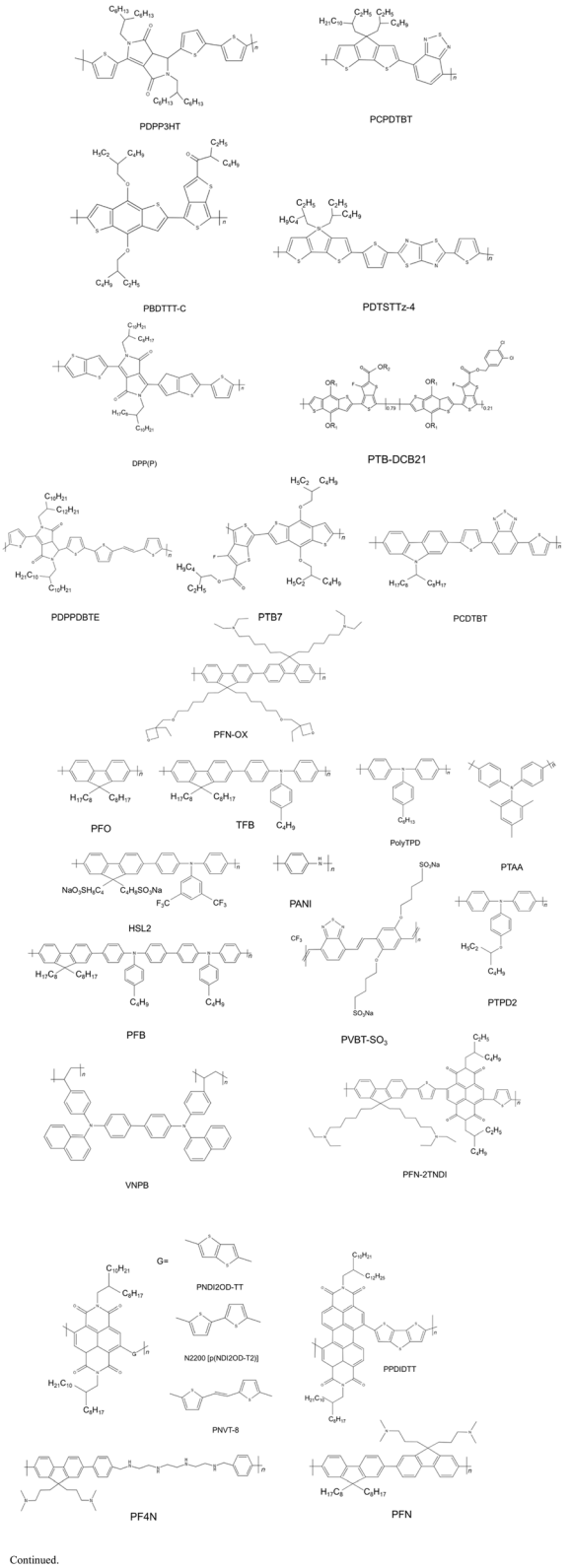

Fig. 22 The structures of some SCPs have been researched further.

chain, representing the length of a hypothetical segment of the chain that behaves as a rigid rod. An L_k implies a stiffer chain, which can affect the polymer's ability to form ordered structures. In the context of PSCs, polymers with longer Kuhn lengths may form more crystalline domains, leading to improved charge mobility and, consequently, better device performance.[211] The rigidity of SCPs in PSCs is crucial for maintaining structural integrity and facilitating efficient charge transport. A rigid polymer backbone can help to minimize the reorganization energy, which is beneficial for charge transfer processes.[212] For example, as mentioned a helicene-based SCP with a high T_g demonstrated exceptional mechanical properties, contributing to the thermal durability and operational stability of PSCs. In summary, the radius of gyration and Kuhn length of SCPs can significantly impact the morphology, charge transport, and overall efficiency of PSCs.

4.2.4 The crystallinity of SCPs. The amorphous and crystalline regions of SCPs play crucial roles in the performance of PSCs. The crystalline regions are typically associated with higher charge mobility due to their ordered structure, which can enhance the efficiency of charge transport within the solar cell. On the other hand, the amorphous regions can contribute to the flexibility and processability of the polymer, which is beneficial for the fabrication of solar cells. In the context of PSCs, the presence of both amorphous and crystalline regions can affect the optical and electronic properties of the active layer.[213] For instance, a study focusing on P3HT embedded with nitrogen/sulfur-doped graphene quantum dots (NS-GQDs) demonstrated that the degree of crystallinity influences the enhancement in electronic charge transfer for both the amorphous and crystalline regions.[214] This suggests that controlling the ratio and distribution of these regions within the SCP can be key to optimizing the performance of PSCs. Moreover, the interaction between the polymer and the perovskite material can be affected by the degree of crystallinity, which in turn can influence the overall PCE of the solar cell. Therefore, understanding and manipulating the effects of amorphous and crystalline regions in SCPs is essential for the development of high-performance perovskite solar cells.[215]

4.2.5 H- and J-aggregation. Intra- and inter-chain interactions of SCP nanowires (J- and H-aggregate, respectively) play a significant role in the performance of PSCs (Fig. 23). Intra-chain interactions are the interactions within a single polymer chain. They affect the polymer's ability to transport charge along its length. Efficient intra-chain interactions facilitate the movement of charge carriers, such as electrons and holes, which is crucial for the high electrical conductivity required in PSCs. Inter-chain interactions occur between adjacent polymer chains. They are vital for creating pathways that allow charge carriers to move between chains. Good inter-chain stacking can lead to enhanced charge mobility across the polymer network, contributing to the overall efficiency of the solar cell.[189] Both intra- and inter-chain interactions are influenced by the molecular structure of the polymer, such as the rigidity of the backbone and the nature of the side chains.[216,217] For instance, a study on naphthalene-diimide-based copolymers showed that a synergistic effect between intra-chain and inter-chain interactions gives rise to high electron mobilities,[218] which is desirable for PSCs. This indicates that neither intra-chain nor inter-chain interactions alone are sufficient; rather, their

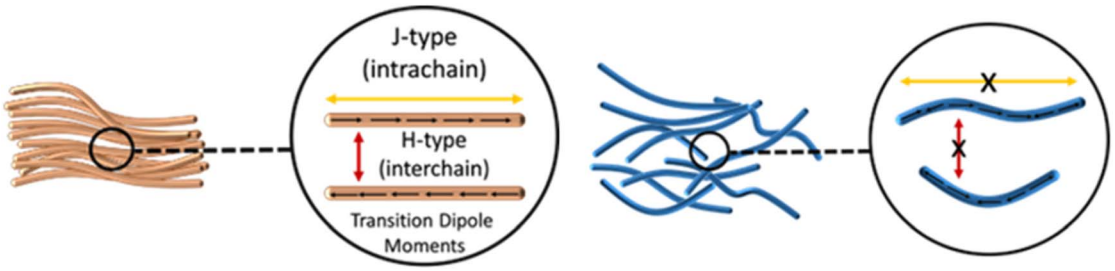

Fig. 23 Schematic of the J-type and H-type interactions in the SCP chains.

combination forms a robust network that supports efficient charge transport. Furthermore, the morphology of SCP nanowires, which is dictated by these interactions, can impact the light absorption, charge separation, and charge collection processes within PSCs.[189] Nanowires offer a direct pathway for charge carriers, which can reduce the distance that electrons and/or holes need to travel, thus minimizing recombination losses. This direct path can lead to improved charge mobility and higher PCEs.

Nanowire P3HT with the advantage of higher carrier mobility along both the vertical and parallel directions is a choice for facilitating hole extraction from the perovskite.[189,219]

4.2.6 Hot injection carriers and the role of SCPs. Hot electron/hole injection in solar cells refers to the process where high-energy charge carriers are generated by absorbing photons with energy greater than the bandgap of the solar cell material. Instead of losing this excess energy as heat, these hot carriers are quickly extracted before they can cool down, which can potentially increase the efficiency of the solar cell beyond the conventional limits (Fig. 24). The concept is a part of the efforts to surpass the Shockley–Queisser limit, which is the theoretical maximum efficiency of a single p–n junction solar cell under standard illumination. Hot carrier solar cells aim to utilize the excess kinetic energy of the charge carriers to achieve higher power conversion efficiencies.[220–222] However, there are challenges in realizing hot carrier solar cells, such as the need for materials that can effectively extract hot carriers and the requirement to minimize energy loss through carrier relaxation. Research in this area is ongoing, with various approaches being explored to optimize the extraction of hot carriers and integrate them into practical solar cell designs. SCPs can address the challenge of hot carriers in perovskite solar cells by providing pathways for efficient charge transfer. A study has shown that hot electrons can be injected into the low-lying LUMOs of certain SCPs.[223] This process can potentially lead to a loss pathway for hot electrons, which is significant because the final photocurrents of perovskite solar cells are affected by the suppression of this loss pathway. These findings suggest that by carefully selecting and engineering SCPs, it's possible to optimize the charge transport layers in perovskite solar cells, thereby improving their efficiency and stability while addressing the hot carrier challenge.

4.2.7 Hybrid polymer–perovskite bulk heterojunctions. The interpenetrating network (IPN) structure of Bulk Hetero Junction (BHJ) donor/acceptor SCPs and also intertwining into the perovskite layer offers several benefits for perovskite solar

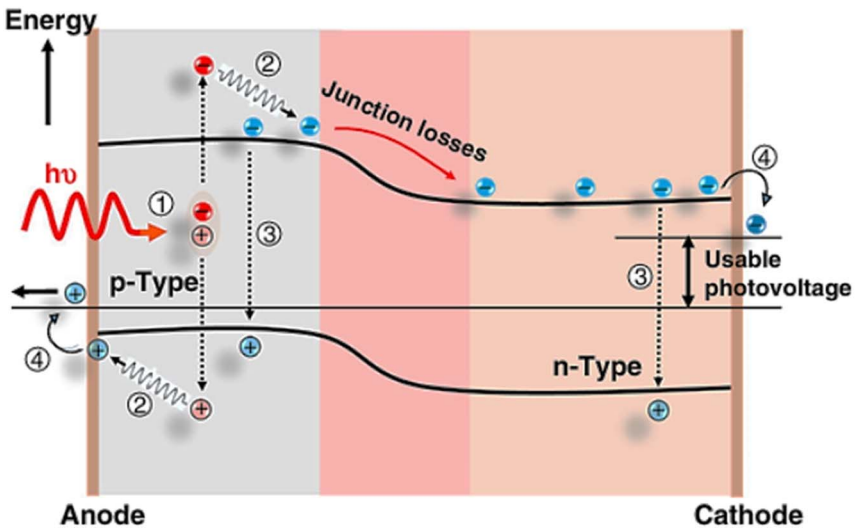

Fig. 24 Major energy loss mechanisms in standard single-junction solar cells: (1) photon absorption and excitation – initial conversion of sunlight into electron–hole pairs. (2) Thermalization of hot carriers – energy loss as excited electrons relax to the band edge. (3) Recombination losses – wasted energy from electron–hole pair annihilation (radiative/non-radiative). (4) Contact resistive losses – efficiency reduction due to imperfect charge collection at electrodes. Reprinted from *Nature*, Irfan Ahmed, *et al.*, 2021, under CC BY license.[222]

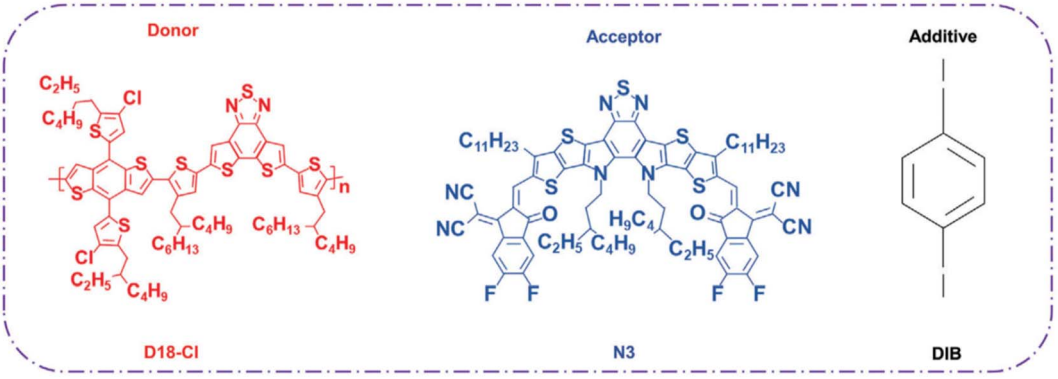

Fig. 25 Donor: the D18-Cl molecule is a polymer that functions as the electron donor in the heterojunction. The researchers chose this specific donor to pair with the acceptor N3 due to its optimal electronic and morphological properties, which are beneficial for achieving a larger (V_{OC}). Acceptor: N3 is a non-fullerene acceptor (NFA) that acts as the electron acceptor. It's designed to absorb light in the near-infrared spectrum, extending the overall light-harvesting range of the solar cell. DIB, which stands for 1,4-diiodobenzene, is used as an additive. Its purpose is to improve the crystallinity and morphology of the N3 acceptor layer during the fabrication process. This helps reduce material damage when the subsequent donor layer is deposited on top. Reproduced with permission from Li He, *et al.*, *Advanced Functional Materials*, 2024, Wiley.[229]

cells.[224] By employing a mixture of electron donor and electron acceptor materials the perovskite/BHJ structure can be formed.[225,226] The interconnected pathways within an IPN facilitate efficient charge transport, which is crucial for the high performance of PSCs. The IPN structure can enhance the separation of electron–hole pairs, reducing the probability of recombination before they are extracted, which is a common source of energy loss. The large interface area provided by an IPN can lead to better contact between the polymer and the perovskite layer, enhancing charge extraction and reducing recombination losses. The large interface area in an IPN can improve the contact between the active layer and charge transport layers, which minimizes charge recombination at these interfaces, a critical factor in energy loss. IPNs can help stabilize the perovskite layer against environmental factors such as moisture and oxygen, which can degrade the material and lead to increased non-radiative recombination and energy loss.

The miscibility diagram of SCP and perovskite solutions and blends is a graphical representation that shows the compatibility of the two materials when mixed.[227,228] It typically displays the phase behaviour of the blend across different compositions and temperatures, indicating regions where the materials are fully miscible, partially miscible, or immiscible. In the context of SCPs and perovskites, miscibility is crucial for the performance of devices like solar cells, where the microstructure and phase morphology of the active layer can significantly impact efficiency. In layered perovskite solar cells, the operation mechanism involves energy transfer from layered to 3D-like perovskite networks. The morphology of the interpenetrating network can affect this energy transfer, thus impacting the efficiency and stability of the solar cell.

A heterojunction is the interface formed between two different semiconductor materials. This interface is crucial for the operation of the solar cell, as it drives the separation of

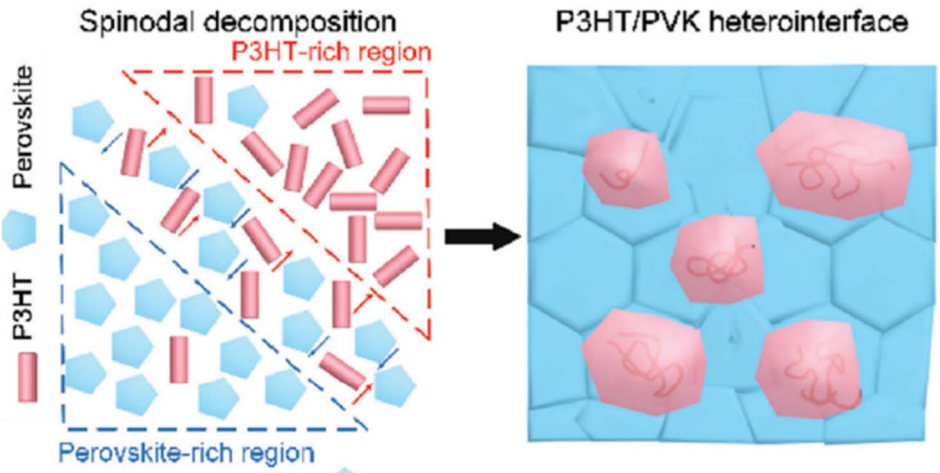

Fig. 26 This describes the interfacial structure created between P3HT and perovskite (PVK) when blended together. The two polymers form a phase-separated boundary that significantly influences charge transport properties in organic electronic devices. Reproduced with permission from Yuqian Yang, *et al.*, *Advanced Materials*, 2024, Wiley.[227]

charge carriers. A research study[229] investigates and compares two types of heterojunctions: the BHJ and the pseudo-planar heterojunction (PPHJ). The primary difference lies in how the donor and acceptor layers are arranged. In the BHJ, the donor and acceptor materials are mixed into a single layer, creating a distributed heterojunction throughout the bulk of the material. The PPHJ structure is created by sequentially depositing the acceptor (N3) and then the donor (D18-Cl) materials in distinct layers. This results in a more ordered, vertically separated structure, creating a sharper, more defined interface between the layers. Unlike the mixed BHJ, the PPHJ has a clear vertical distribution with the acceptor material (N3) concentrated at the bottom and the donor material (D18-Cl) at the top (Fig. 25). This well-defined separation is crucial for efficient charge transport, as it creates clear pathways for electrons and holes to move to their respective electrodes with less chance of recombination. The ordered PPHJ structure suppresses charge recombination and improves carrier transportation compared to the BHJ. It exhibits higher electron and hole mobility and a more balanced charge transport, which contributes to a higher J_{SC} and FF. The PPHJ structure has less energetic disorder, which means there are fewer electronic traps that can impede carrier movement. This leads to a higher (V_{OC}). The PPHJ structure, with its hydrophobic long alkyl chains and distinct fiber network, provides a more effective barrier against moisture. This leads to significantly improved long-term humidity and operational stability compared to devices based on the BHJ structure. The optimized integrated perovskite/PPHJ solar cell achieved a champion PCE of 23.25%. This is a significant increase from the control device's PCE of 20.14%. In a high-humidity environment ($\approx$25 °C, $\approx$80% relative humidity), the optimized device maintained 81% of its initial PCE after 1200 hours, and retained over 89% of its initial efficiency after 1000 hours of continuous illumination.

Using P3HT frequently results in a reduced V_{OC} in PSC devices. This is due to the inadequate physical interaction between P3HT and PVK, hindering effective carrier transport. The benefits of this polymer encompass its ability to avoid the need for moisture-attracting additives, deliver high performance, ensure prolonged durability, and facilitate processing over large areas.[161,198] Yuqian Yang *et al.*[227] use the spinodal or metastable decomposition of P3HT in the perovskite layer that created a hetero-interface bi-continuous morphology with an interpenetrating network structure. In order to lower the system's Gibbs free energy (ΔG), spontaneous uphill diffusion (spinodal decomposition) took place. Molecules of P3HT clustered together creating a phase rich in P3HT, while PVK molecules also aggregated to establish a PVK-rich phase (Fig. 26). As

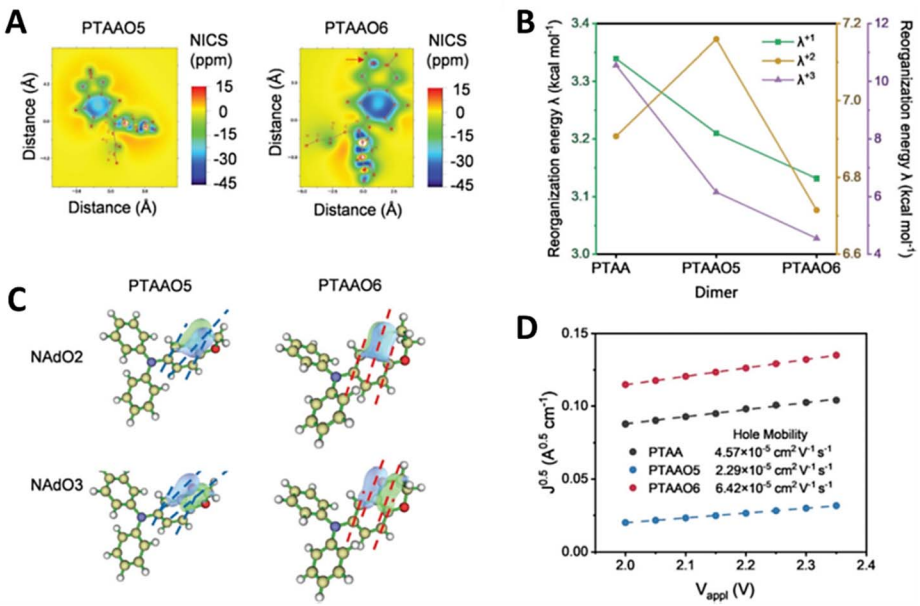

Fig. 27 (A) NICS distribution: this panel shows maps of the Nucleus-Independent Chemical Shift (NICS), a computational metric where lower values signify stronger aromatic conjugation. The side group in PTAAO6 exhibits a region of very strong shielding (NICS value ≈ -30 ppm), indicating that the specific bond angles in its six-membered ring effectively extend the π-conjugation. In contrast, the conjugation in PTAAO5's side group is disrupted. (B) Natural Adaptive Orbitals (NAdOs): these images visualize the molecular orbitals. For PTAAO6, the orbitals are shown to be well-aligned and parallel along the C–O bonds, which confirms the molecular orbital alignment responsible for the extended conjugation. (C) Reorganization energy: this chart shows the calculated reorganization energies, which represent the energy required for a molecule to adjust its geometry during charge transport. According to Marcus theory, a lower reorganization energy typically leads to higher charge mobility. The results show a clear trend where PTAAO6 has the lowest reorganization energy of the three polymers, predicting that it should have the best charge transport capability. This is attributed to its rigid structure, which requires minimal reorganization when charged. (D) Experimental hole mobility: this panel presents the experimental verification of the theoretical predictions using the SCLC method. The measurements confirm that PTAAO6 has the highest hole mobility at 6.42×10^{-5} cm^2 V^{-1} s^{-1}, a significant improvement over standard PTAA (4.57×10^{-5}). This result directly links PTAAO6's enhanced conjugation and low reorganization energy to its superior performance as a hole transport material. Reproduced with permission from Yuqian Sen Yin, *et al.*, *Advanced Energy Materials*, 2025, Wiley.[232]

both the PVK and P3HT phases materialized simultaneously and within the same area, they became entwined, resulting in the formation of a network structure that interpenetrates. Elemental analysis indicates that in the top layer, there is a decrease in Pb content originating from the perovskite and an increase in sulphur (S) content, primarily from P3HT. These findings imply the existence of a P3HT/PVK hetero-interface.

This method also brings gradual precipitation of the P3HT phase mitigating the energy barrier and increasing hole extraction and transportation through the P3HT/perovskite hetero-interface; thus carrier and energy loss can be effectively reduced. Following the modification with P3HT, the observed red shift in both the PL spectra and the UV-visible absorption spectra matched the data from PL mapping. This redshift is primarily due to the formation of the P3HT/PVK hetero-interface, which aids in the extraction of holes from the perovskite, a process enhanced by the p-type characteristics of P3HT. The PCE of the control device was calculated to be about 20.34%, and the addition of an optimal amount of P3HT soluble in chlorobenzene as an anti-solvent of perovskite brought up the PCE to about 23.02%. In addition, the water contact angles of the films are 58.96° and 96.73° for PVK and P3HT/PVK films, respectively.

4.2.8 SCPs as CTLs. SCPs play a crucial role as CTLs in PSCs, where they primarily function to extract and transport charges while minimizing recombination losses. Their role can be categorized as extracting electrons from the perovskite, blocking opposite charge carriers to reduce charge recombination, improving interfacial contact with the cathode or anode, passivating perovskite surface defects, improving energy-level alignment between perovskite and the electrode, and enhancing stability by protecting the perovskite from moisture/oxygen.[230,231]

While PTAA is a popular choice for an HTL in PSCs, it has several drawbacks that hinder device performance. PTAA has a poor interaction with the perovskite material it is in contact with. This can lead to a lower-quality perovskite film growing on top of it. The inherent structure of PTAA limits its ability to efficiently transport positive charge carriers (holes) from the perovskite to the electrode. To address PTAA's weaknesses, the researchers employed a side-chain modification strategy called cyclic alkoxylation.[232] This involves attaching oxygen-containing ring structures to the side benzene groups of the PTAA backbone. The core of their design is the insight that the size and geometry of the attached ring are critical. Based on theoretical calculations, they determined that a six-membered ring offers the optimal balance between molecular stability and the desired electronic energy levels for an HTL. Following this strategy, they synthesized two new polymers for comparison, PTAAO5 (modified with a five-membered benzo[*d*][1,3]dioxole ring), and PTAAO6 (modified with an optimized six-membered dihydrobenzo[*b*][1,4]dioxine ring) (Fig. 27). The study found that the six-membered ring in PTAAO6 provides significant advantages over both the original PTAA and the five-membered ring version, PTAAO5. The specific bond angles within the six-membered ring of PTAAO6 allow for better molecular orbital alignment, leading to extended π-conjugation in the side groups. PTAAO6 has a deeper HOMO energy level (−5.12 eV) compared to PTAA (−5.07 eV), which creates a more favourable alignment with the perovskite layer for efficient hole extraction. The improved conjugation and more rigid molecular structure enhance charge transport, giving PTAAO6 a higher hole mobility (6.42×10^{-5} cm^2 V^{-1} s^{-1}) than PTAA (4.57×10^{-5} cm^2 V^{-1} s^{-1}). Ultimately, using PTAAO6 as the HTL resulted in a solar cell with an outstanding efficiency of 25.19% and excellent operational stability.

The modification of macromolecule chains can be effective for higher-performance hybrid PSCs. Rai *et al.*[233] investigated the effect of polymer chains consisting of ester and thiophene groups in the format of a thin layer between $FA_{0.92}MA_{0.08}$-$Pb(I_{0.92}Br_{0.08})_3$ perovskite and spiro-OMeTAD as the HTM (Fig. 28). For this purpose, two poly(bithiophene ester) (PBTE) and poly(terthiophene diester) (PTTDE) were used. More functional groups have worked more successfully; in this way the PL intensity from the perovskite film was quenched two-fold and 3.5-fold upon applying poly(bithiophene ester) and poly(-terthiophene diester), respectively. In the same way, EIS indicates lower charge transport resistance and higher charge recombination resistance that can be attributed to higher concentration of the ester functionalities per thiophene unit. The findings indicate that the creation of Lewis acid–base complexes, involving Pb^{2+} ions with insufficient coordination in the perovskite structure and oxygen atoms within the ester

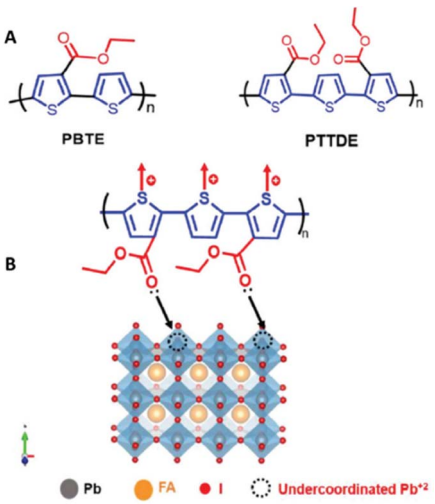

Fig. 28 (A) Chemical architectures of PBTE and PTTDE. Illustrated molecular configurations of the conjugated polymers PBTE (poly(-benzodithiophene-ethylene)) and PTTDE (poly(thienothiophene-di-ketopyrrolopyrrole-ethylene)), highlighting their distinct structural motifs. (B) Dual-functional interface mechanism in PSCs. The proposed operational model demonstrates how these polymeric interlayers function at the perovskite/HTM junction in PSCs: passivation pathway (black arrows): the polymers mitigate interfacial defects and non-radiative recombination through coordinated chemical interactions with undercoordinated lead ions at the perovskite surface. Charge transport pathway (red arrows): optimized energy level alignment and π-conjugated backbones facilitate efficient hole extraction from the perovskite absorber layer to the HTM while blocking electron backflow. Reprinted from *Advanced MaterialsTechnologies*, Nitish Rai, *et al.*, 2024, under the Creative Commons CC BY-NC-ND license.[233]

groups, could potentially reduce recombination and enhance the efficiency of charge extraction. Furthermore, functional groups of polymers especially [C═O] can inhibit the formation of Pb^0 even at 85 °C and about 45% relative humidity. Without any interface modification, the PSCs showed a PCE of 17.8 ± 0.2%. The incorporation of PBTE led to a PCE of 19.2 ± 0.2%, and the use of PTTDE further increased the PCE to 20.0 ± 0.1%, along with improvements in the I_{SC}, V_{OC}, and FF. Elevated V_{OC} values suggest that the ester-functionalized thiophene polymer interlayers are effective in reducing interfacial recombination. Meanwhile, enhancements in FF indicate improved charge transfer efficiency between the perovskite layer and the HTM. The faster-decaying photoluminescence component's lifetime (τ_1) commonly associated with the quenching of charge carriers through trap states or interfacial charge transfer, was reduced from 0.40 μs in the uncoated perovskite film to 0.23 μs with PBTE coating and further to 0.03 μs with PTTDE coating. The marked reduction in τ_1 aligns with the onset of a swift charge-transfer mechanism at the interface between the perovskite and polymer, which facilitates the extraction of holes from the perovskite into the PBTE or PTTDE layers. This enhancement is probably linked to the polythiophene structure of the polymers and may be further supported by the creation of Lewis acid–base adducts between the perovskite's under-coordinated Pb^{2+} ions and the oxygen atoms present in the ester groups. In an ambient lab setting with about 45% humidity over two weeks, nonencapsulated devices showed a decline in PCE after an initial increase.

4.2.9 Free dopant SCPs. The difference between dopant-free and doped SCPs in perovskite solar cells lies in their electrical properties and impact on device stability.[66] Doped SCPs require the addition of dopants to enhance their electrical conductivity and PCE. Dopants can introduce instability as they may attract moisture, which can degrade the perovskite layer. Dopant-free SCPs are inherently conductive without the need for additional dopants.[234,235] Dopant-free polymers can still achieve impressive efficiencies and are considered more stable, making them attractive for long-term applications. Overall, dopant-free materials are gaining attention for their potential to provide a balance between efficiency and stability in PSCs. Some researches focus on dopant-free polymeric HTMs due to high carrier mobilities, matching energy levels with perovskite, homogeneous film formation, and excellent hydrophobicity which are attractive options to replace conventional materials.

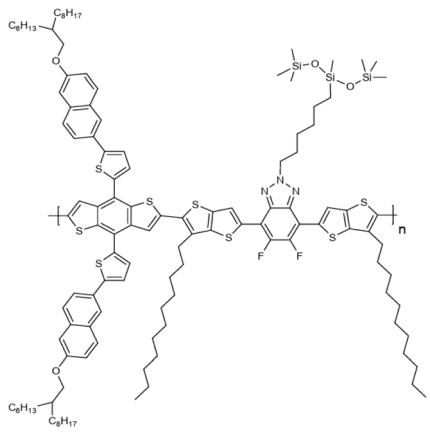

Fig. 29 The chemical structure of poly (BDT-TA-BTASi). Reproduced with permission from Zhiqing Xie, *et al.*, *ACS Applied Materials & Interfaces*, 2024, ACS.[236]

Xie *et al.* designed a donor–π–acceptor HTM: poly[4-(5-(4,8-bis(5-(6-((2-hexyldecyl)oxy)naphthalen-2-yl)thiophen-2-yl)benzo[1,2-*b*:4,5-*b*′]dithiophen-2-yl)-6-undecylthieno[3,2-*b*]thiophen-2-yl)-5,6-difluoro-2-(6(1,1,1,3,5,5,5-heptamethyltrisiloxan-3-yl)-hexyl)-7-(6-undecylthieno[3,2-*b*]thiophen-2-yl)-2*H*-benzo[*d*]-[1,2,3]triazole] (BDT-TA-BTASi) (Fig. 29).[236] This polymer has a co-planar structure with π–π strong stacking and consequently a high charge mobility that is approximately close to that of doped spiro-OMeTAD. Furthermore, the presence of siloxane and alkyl side chains promotes solubility, hydrophobicity, and molecular packing. The PCE of this device approaches 21.53%. The device maintained 92% of its performance following a 1000-hour storage period in a nitrogen environment. Additionally, it demonstrated considerable stability when exposed to elevated temperatures of 60 °C and a relative humidity level of 80 ± 10%, preserving 92% and 82% of its initial efficiency after 400 hours, respectively.

In another study,[237] in a Double-layer Halide Architecture (DHA) free dopant-P3HT was used as the HTM to tackle the poor contact between perovskite and P3HT layers. DHA is formed by depositing a slim layer of wide-bandgap halide (WBH) perovskite onto a narrow-bandgap light-absorbing layer. This is achieved through an *in situ* reaction involving *n*-hexyl trimethyl ammonium bromide (HTAB) directly on the surface of the perovskite to produce $HTAB_{0.3}(FAPbI_3)_{0.95}(MAPbBr_3)_{0.05}$. Upon applying P3HT to the DHA surface, the intertwining of its alkyl chains with those of HTAB ($C_6H_{13}^-$) is expected to facilitate P3HT's self-organization. Additionally, the presence of the $N^+(CH_3)_3^-$ group makes the perovskite surface less susceptible to damage in moist environments. To assess the function of DHA, the increased V_{OC} in HTM-free DHA-based PSCs, along with the extended charge duration in the DHA device, indicate that the WBH layer successfully neutralizes charge traps on the perovskite's surface. In the sample containing DHA, P3HT shows a dense nanofiber morphology. While amorphous P3HT exhibits minimal charge mobility, with values around 10^{-5} cm^2 V^{-1} s^{-1} the self-organized P3HT nanofibrils, which have robust π–π interactions, display a significantly enhanced mobility rate of 0.1 cm^2 V^{-1} s^{-1} in the absence of any doping agents. The Raman test indicates that more of the P3HT polymers on the DHA surface are oriented along the preferred direction. The DHA device demonstrates a significant enhancement in PCE, about 23.3% for the best sample, linked to an increased V_{OC} and FF, along with the elimination of hysteresis. Furthermore, the DHA device that incorporates P3HT exhibits a reduced series resistance (R_s) compared to the control device also using P3HT. Conversely, the DHA film presents a higher R_s relative to the control perovskite film, which can be attributed to the elevated aliphatic composition of the WBH. DHA devices without encapsulation and exposed to 85% humidity at ambient temperature preserved about 80% of their original efficiency

after 1008 hours. In contrast, the control device deteriorated entirely in just 200 hours.

5 Large scale production of hybrid PSCs

Large-scale production of hybrid PSCs involves several methods developed for scalability, efficiency, and stability.

5.1 Spin coating

Initially used as a laboratory technique, it can be adapted for larger production using automated systems to ensure uniform film formation.

5.2 Slot-die coating

Slot-die coating[238–240] is a roll-to-roll (R2R) compatible deposition technique used to fabricate thin, uniform films for solar cells. It involves precisely dispensing a liquid ink (*e.g.*, perovskite precursor solution) through a slit-shaped die onto a moving substrate, enabling high-throughput, large-area production with minimal material waste. Slot-die head contains a microfluidic channel to control ink flow. The pump system delivers ink at a controlled flow rate (μL min^{-1} to mL min^{-1}). The moving substrate is typically glass, plastic, or metal foil (for flexible PSCs). The drying system includes inline heaters or IR lamps for solvent evaporation. Table 17 shows some key challenges and solutions of this method.

5.3 Vapor-assisted deposition

Vapour-assisted deposition (VAD)[241,242] is a two-step, solvent-free method to fabricate high-quality perovskite films. This method is compatible with R2R and vacuum processes. Unlike solution processing, it involves depositing a solid metal halide (*e.g.*, PbI_2 or $PbBr_2$) layer *via* spin-coating, evaporation, or sputtering. The layer exposed to organic halide vapor (*e.g.*, MAI, FAI, or CsI) in a controlled environment diffuses into the solid film and reacts to form the perovskite crystal. This method is prized for precise stoichiometry control, reduced defects, and scalability. VAD bridges the gap between lab-scale precision and industrial scalability, offering a path to stable, high-efficiency PSCs. While slower than solution methods, its defect-suppressing capabilities make it ideal for premium applications (*e.g.*, space PV and tandems). Hybrid approaches, and combining VAD with inkjet printing for patterned deposition are some of the future directions. Lead-free perovskites adapt VAD for Sn^{2+} or Bi^{3+}-based films. Table 18 shows some important challenges and solutions of this method.

Table 17 Challenges and solutions of slot-die coating method

Challenge	Solution
Film defects (*e.g.*, pinholes)	Optimize ink formulation (additives and solvents)
Crystallization control	Use gas quenching or anti-solvent dripping
Edge effects	Adjust die design (*e.g.*, multi-slot dies)
Reproducibility	Automated feedback systems for speed/flow control

Table 18 Challenges and solutions of the vapour-assisted deposition method

Challenge	Solution
Slow reaction kinetics	Optimize temperature/vapor pressure
Limited thickness control	Layer-by-layer deposition
Equipment cost	Shared vacuum tools (*e.g.*, with OLED industry)
PbI_2 residuals	Precise stoichiometry tuning

5.4 Spray coating

Spray coating[243,244] is a solution-based deposition technique where a perovskite precursor ink is atomized into fine droplets and sprayed onto a substrate using pressurized gas (*e.g.*, air and nitrogen). The droplets dry on contact, forming a thin perovskite film. This method is low-cost, scalable, and compatible with large-area or flexible substrates, making it attractive for industrial production. Perovskite precursors (*e.g.*, PbI_2 + MAI/FAI) dissolved in solvents (DMF, DMSO, or mixtures). Additives (*e.g.*, MACl, polymer binders) may be included to improve film quality. The ink is forced through a nozzle, breaking into fine droplets (~1–50 μm diameter). Ultrasonic, pneumatic, or electrospray methods can be used. Droplets land on a heated substrate (50–120 °C), where the solvent evaporates. Multiple passes may be needed for uniform thickness. Annealing (100–150 °C) was used to crystallize the perovskite. Optional anti-solvent quenching was used to enhance grain growth. Several future research directions include high-speed robotic automated spray systems for R2R production

Table 19 Challenges and solutions of the spray coating method

Challenge	Solution
Non-uniform films	Optimize nozzle design, substrate heating, and spray distance
Pinholes/cracks	Use solvent engineering (*e.g.*, mixed solvents) or additives
Low efficiency (*vs.* spin coating)	Post-treatment (*e.g.*, gas quenching and solvent annealing)
Clogging of nozzles	Filter inks and use pulsed spraying

Table 20 Challenges and solutions of the inkjet printing method

Challenge	Solution
Nozzle clogging	Ink filtration (0.2 μm) and solvent additives
Coffee-ring effect	Mixed solvents and substrate heating (40–60 °C)
Film roughness	Multi-pass printing with drying intervals
Resolution limits	Electrohydrodynamic (EHD) printing for <5 μm features

Table 21 Critical parameters of the blade coating method

Parameter	Typical range	Effect
Blade-substrate gap	100–300 μm	Directly controls wet film thickness
Coating speed	5–50 mm s^{-1}	Faster = thinner films, but affects crystallization
Substrate temp.	30–80 °C	Higher = faster drying and smaller grains
Ink viscosity	5–50 cP	Higher viscosity = thicker films

and hybrid methods combining blade coating or inkjet printing. Some key challenges and solutions of this method are presented in Table 19.

5.5 Inkjet printing

Inkjet printing[245,246] is an additive, non-contact manufacturing technique that deposits functional inks (including perovskite precursors) in precise patterns by ejecting tiny droplets (10–100 picolitres) through microscopic nozzles. This method enables digital patterning (mask-less deposition), high material utilization (>95% efficiency), and low-temperature processing (compatible with flexible substrates). The print head contains 50–1000 nozzles (typically piezoelectric). The ink reservoir holds perovskite precursor solution. A high-precision XY-motion stage is used for accurate substrate alignment. The drying system utilizes IR lamps or a heated stage to remove solvents.

Perovskite precursors (PbI_2 + MAI/FAI) dissolved in mixed solvents (DMF/DMSO with viscosity modifiers) were optimized for a surface tension of 28–35 mN m^{-1}, viscosity of 8–20 cP, and particle size of <1% of the nozzle diameter. Piezoelectric actuators create pressure waves to eject droplets. Typical drop velocity is 5–10 m s^{-1}, and drop spacing is 20–50 μm. Droplets merge on the substrate *via* controlled coffee-ring effects, followed by multi-pass printing to achieve the desired thickness (typically 300–500 nm), and post-annealing at 100–150 °C for crystallization. Future directions include hybrid printing combined with laser scribing for monolithic interconnections, AI-driven optimization using machine learning for droplet placement correction, multi-material printing to enable simultaneous deposition of all device layers, and flexible electronics *via* direct printing on curved surfaces for wearable photovoltaic applications. Important challenges and proposed solutions for this approach are summarized in Table 20.

5.6 Blade coating

Blade coating (also called doctor blading)[247,248] is a solution-based deposition technique where a sharp blade spreads a liquid perovskite precursor ink across a substrate to form a thin, uniform film. This method bridges the gap between lab-scale spin coating and industrial R2R production, offering high material utilization (>90% efficiency), large-area compatibility (unlimited substrate width), and precise thickness control (50–500 nm range). The process begins with ink deposition of a perovskite precursor (*e.g.*, PbI_2 + MAI in DMF/DMSO, often with additives like MACl or 2D seeds), followed by blade-induced shear flow that forms a liquid meniscus, which dries into a film across three zones—upstream (wet ink reservoir), meniscus (evaporation/crystallization), and downstream (dried film). Post-treatment includes solvent quenching (*e.g.*, chlorobenzene) and thermal annealing (100–150 °C) to finalize the layer. Some critical parameters of this method are listed in Table 21. In Table 22, several significant challenges and the solutions related to this method are outlined.

Table 22 Challenges and solutions of the blade coating method

Challenge	Solution
Streaks/defects	Optimize blade edge roughness (<50 nm)
Non-uniform drying	Gradient heating or gas flow control
Coffee-ring effect	Solvent engineering (high boiling point additives)
Large grain growth	Anti-solvent dripping or vapor-assisted crystallization

5.7 Flexographic printing

Flexographic printing or flexo-printing[249,250] is a R2R compatible technique that uses a flexible relief plate to transfer ink onto substrates. Key features include direct patterning *via* raised image areas on a photopolymer plate, anilox roller controls ink volume with microscopic cells, and fast deposition with μm-level resolution. Common substrates include flexible PET, PEN, ITO-coated glass, or metal foil. The substrate undergoes plasma treatment, UV-ozone exposure, or solvent cleaning to enhance adhesion and remove contaminants. Surface treatments (*e.g.*, self-assembled monolayers) may be applied to improve wettability and charge transport. Perovskite ink includes organic and inorganic salts dissolved in solvents like DMF/DMSO. Additives (*e.g.*, polymers and surfactants) are used for stability. Viscosity, surface tension, and drying behavior are optimized to ensure uniform ink transfer. An anilox roller (engraved with micro-cells) picks up a controlled amount of ink from an ink reservoir. A doctor blade removes excess ink, ensuring precise volume transfer. A flexographic plate (made of an elastomer or photopolymer) transfers the ink onto the moving substrate. Pressure, speed, and temperature are controlled for uniform deposition. Controlled heating (infrared or hot air) ensures proper drying without phase separation. Annealing is typically done at 100–150 °C to improve perovskite crystallization and polymer integration. Fig. 30 shows a schematic of the flexo-printing setup. Table 23 lists the current challenges and solutions of this method.

5.8 Hybrid chemical vapor deposition (HCVD)

Hybrid Chemical Vapor Deposition (HCVD)[251,252] is a thin-film deposition method used to fabricate high-quality perovskite

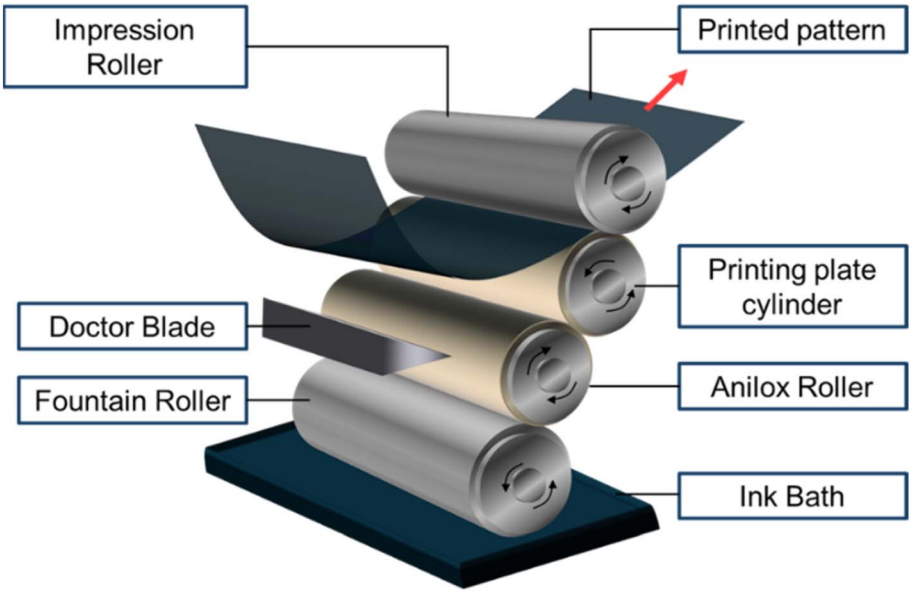

Fig. 30 Schematic picture of the flexographic setup. A flexographic printing setup for PSCs is a roll-to-roll (R2R) system designed for high-speed, patterned deposition of liquid inks onto flexible substrates. Its core structure revolves around the precise interaction of several rotating cylinders. The process begins with an ink fountain that supplies the perovskite precursor ink. A rotating anilox roller, which is a hard cylinder laser-engraved with a microscopic cell pattern, picks up a controlled and metered volume of ink from the fountain. This anilox roller then transfers the ink to the raised features of a soft, patterned printing plate, which is mounted onto the plate cylinder. As the flexible substrate (such as PET or PEN coated with transparent electrodes) passes between this plate cylinder and a central impression cylinder, the ink is pressed from the printing plate onto the substrate, forming the desired patterned thin film. This entire "inking—metering—transfer—printing" sequence happens in a continuous, rapid motion, allowing for the fast and scalable fabrication of perovskite solar cell layers.

Table 23 Challenges and solutions of the flexo printing method

Challenge	Innovation
Crystallization control	Hybrid thermal/vapor annealing stations
Edge definition	Laser-etched plates (5 μm precision)
Layer registration	CCD camera alignment systems

layers with excellent crystallinity, uniformity, and scalability. It combines aspects of solution processing and vapor-phase deposition, making it an attractive method for large-area PSC fabrication. A precursor solution containing lead halide salts is spin-coated or blade-coated onto the substrate. This partially dried precursor layer acts as a reactive medium for the subsequent vapor-phase step. The substrate is placed inside a heated vacuum chamber. Organic halides (*e.g.*, MAI and FAI) are vaporized at controlled temperatures (~150–200 °C) and diffuse into the PbI_2 film. The reaction forms a high-purity perovskite layer. The film undergoes post-annealing (~100–150 °C) to enhance crystallinity and grain growth. This step also helps in removing residual solvents and improving film stability. HCVD combines solution processing (for metal halides) and vapor-phase deposition (for organic components) to grow high-quality perovskite films. The main challenges and solutions are listed in Table 24. The schematic of the HCVD printing setup is shown in Fig. 31.

Table 24 Challenges and solutions of the HCVD method

Challenge	Solution
Slow process	Multi-zone heating for faster vapor diffusion
PbI_2 residuals	Optimize vapor pressure/temperature
Limited to flat substrates	Conformal vapor delivery systems
High equipment cost	Shared vacuum tools (*e.g.*, with OLED production)

Both VAD and HCVD are two-step deposition techniques for fabricating perovskite thin films, but they differ in their process details, precursor application, and scalability. Crucial differences are summarized in Table 25.

For a comparison between the methods described, see Tables 26 and 27.

5.9 Benefits of printing methods

The large-scale printing of solar cells presents numerous advantages essential for the progress and adoption of solar energy technology. By printing solar cells on a larger scale, the cost per unit can be significantly reduced, making solar energy more affordable and competitive with conventional energy sources.[240,256] The high flexibility of printed solar cells allows them to be applied to various surfaces and objects, including buildings, vehicles, and clothing, broadening the possibilities for solar energy generation. Large-scale printing processes can optimize material use, reduce waste, and improve the environmental footprint of solar cell production. This inherently scalable printing process facilitates a swift transition from laboratory-scale prototypes to industrial-scale production, meeting the growing demand for renewable energy sources.[257] The lightweight and adaptable nature of printed

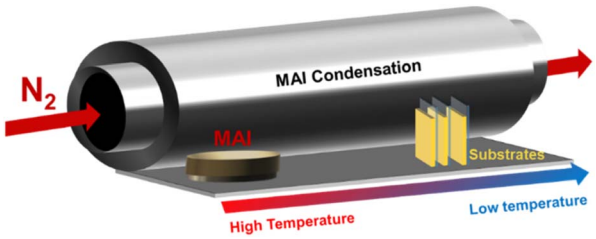

Fig. 31 Schematic picture of the HCVD setup. This machine is an integrated system that merges vapor-phase and solution-phase processing to create high-quality, uniform perovskite films, especially over large areas. Its structure typically consists of several key zones arranged in a linear or in-line sequence. The process begins in the precursor evaporation zone. Here, solid precursor powders (*e.g.*, lead iodide, PbI_2, and organic halides like methylammonium iodide, MAI) are loaded into separate, temperature-controlled crucibles or boats. These crucibles are heated to precise temperatures to sublimate the solids, converting them directly into a vapor without passing through a liquid phase. These precursor vapors are then transported by an inert carrier gas (such as nitrogen or argon) into the main deposition chamber. This chamber contains the substrate, which is typically pre-coated with other solar cell layers (like the electron transport layer) and is often heated on a temperature-controlled stage. It is within this chamber that the "hybrid" aspect often takes place: while the PbI_2 is delivered *via* vapor, a separate solution spray nozzle can simultaneously mist a solution of the organic halide dissolved in a solvent. This allows for precise control over the reaction stoichiometry. As the vapor-phase PbI_2 and the solution-phase organic halide meet at the heated substrate surface, they react to form the perovskite film (*e.g.*, $MAPbI_3$). The chamber is often equipped with vacuum pumps to maintain a controlled, low-pressure environment, which enhances vapor diffusion and leads to a more uniform film with large crystal grains and fewer defects. Finally, the substrate may pass through a post-annealing zone to crystallize the film fully before exiting the system. This combined vapor-solution approach allows for superior control over film morphology and coverage compared to purely solution-based methods.

solar cells supports innovative deployment methods, such as integration into portable devices or temporary installations, which traditional rigid panels cannot achieve. These benefits underscore the transformative potential of large-scale printing technology in the solar industry, paving the way for more sustainable and widespread solar energy use.

5.10 Challenges and defects

When printing solar cells on a large scale, several defects may arise that can impact the performance and longevity of the panels.[258] Material wastage is a significant amount of solution that can be wasted during the printing process, making it unsuitable for large-scale production. Achieving precise patterning is challenging and can hinder module fabrication, particularly when moving from small-scale to large-scale production. Film defects are another important challenge. The thin active layer (100–600 nm) of large-area solar cells is prone to defects that can cause leakage current, reducing production yields.[259] Grain size and grain boundary defects, along with ion migration in the lattice and the compactness of the interface buffer layer, significantly affect the stability of perovskite solar cells.[260] Transitioning from spin-coating to printing as the production scale increases is challenging and essential for fabricating large-area perovskite solar cells. Addressing these defects is crucial for improving the yield and performance of large-scale printed solar cells. Ongoing research and development are focused on refining printing processes and materials to minimize these defects.

5.10.1 Defect types in film formation due to printing. The printing of PSCs can lead to various film defects, which can significantly impact the performance and stability of the cells.

5.10.1.1 Point defects. These are atomic-level defects, including vacancies, interstitials, and substitutions in the perovskite lattice.[261,262] In large-scale printing, inhomogeneous precursor distribution or solvent variations can introduce point defects, leading to non-radiative recombination, which lowers efficiency. Vacancy defects or missing atoms are categorized as iodine vacancies, which are most common due to weak Pb–I bonds. Lead vacancies are less frequent but highly detrimental. Cation vacancies mean that MA^+ or FA^+ is missing from the lattice. Interstitial defects or extra atoms are created because of interstitial halides or extra I^- ions between lattice sites and interstitial Pb that can introduce deep trap states. Anti-site defects or wrong atoms in a site cause severe non-radiative recombination in the case of Pb at the I site. Also, the case of I at the Pb site is rare but disruptive. Substitutional defects or impurity atoms act as dopants; for example replacing Br^- with I^- can passivate defects but may distort the lattice.

Point defects create mid-gap trap states that capture free electrons/holes,[263] and thus reduce V_{OC} and charge carrier lifetime. Mobile defects allow halide ions to migrate under electric fields and cause current–voltage hysteresis and long-term degradation. Deep-level defects dissipate energy as heat instead of light and lower photoluminescence quantum yield (PLQY). Also, these defects accelerate moisture/oxygen

Table 25 Key differences between VAD and HCVD methods

Feature	VAD	HCVD
Crystallinity	May have lower crystallinity due to limited interdiffusion	Tends to yield higher crystallinity and larger grains due to better precursor interaction
Defect density	Higher defects due to limited conversion efficiency of PbI_2 to perovskite	Lower defects as solution interaction enhances perovskite formation
Surface morphology	May suffer from grain boundary defects and pinholes	Produces smoother, pinhole-free films
Scalability	Can be scaled but requires vacuum-based evaporation, increasing cost	More scalable and compatible with R2R processing

Table 26 Perovskite deposition method comparison table[253–255]

Method	Thickness control	Scalability	Speed	Material use	Film quality	Best for
Spin coating	High (10–500 nm)	None	Slow	<10%	Good	Lab R&D
Blade coating	Excellent (50–500 nm)	High	Medium	>90%	Very good	Pilot lines
Slot-die coating	Good (100–1000 nm)	Very high	Fast	>95%	Good	Mass production
Spray coating	Moderate	High	Medium	80–90%	Moderate	BIPV, flexible
Inkjet printing	High (20–500 nm)	Medium	Slow-Med	>95%	Good	Custom patterns
Vapor deposition	Excellent (10–300 nm)	Medium	Slow	>98%	Excellent	Tandems
HCVD	Excellent (50–400 nm)	Medium–high	Slow	>95%	Excellent	High-end apps
Flexographic	Moderate (200–800 nm)	Very high	Fast	>90%	Good	R2R electrodes

Table 27 Industrialization metrics of deposition methods[253–255]

Metric	Spin	Blade	Slot-die	Spray	Inkjet	Vapor	HCVD	Flexo
TRL level[a]	4	6	8	5	4	6	5	5
CAPEX[b] ($ per MW)	—	0.8 M	0.5 M	1.2 M	2 M	5 M	3 M	0.3 M
OPEX[c] ($ per m^2)	—	15	10	20	40	80	50	12
Yield potential (%)	—	95	97	90	85	99	98%	92%
Energy use (kWh m^{-2})	—	0.5	0.3	1.2	2	5	3	0.8

[a] TRL (Technology Readiness Level): scale from 1 (basic research) to 9 (full production). [b] CAPEX (capital expenditure): equipment/installation costs per MW capacity. [c] OPEX (operational expenditure): per square meter production costs.

penetration. These defects can be mitigated by the following methods. Halide compensation, so that excess I^- (*e.g.*, MAI) fills iodine vacancies. Lewis base additives that bind to under-coordinated Pb^{2+} reducing trap states. Polymer additives improve film uniformity and passivate grain boundaries. Mixed solvents (*e.g.*, DMF:DMSO) lead to better crystallization. Thermal annealing heals defects but must be controlled to avoid decomposition. Light soaking helps in defect annihilation under illumination.[264]

5.10.1.2 Non-uniform film thickness. Large-area printing methods can suffer from poor solution spreading, resulting in uneven thickness. Thicker regions may cause excess absorption and higher recombination, while thinner areas lead to low light absorption and shunting paths.[265,266]

5.10.1.3 Grain boundary (GB) defects. In printed large-area solar cells, GBs are particularly problematic because they introduce defects, recombination centres, and ion migration pathways, significantly impacting efficiency and stability.[267–269] Fast solvent evaporation in printing techniques (*e.g.*, inkjet and spray coating) leads to smaller grains and more GBs. Poor control over nucleation leads to random grain orientations, and likewise high defect density. In large-area printing, temperature gradients cause uneven crystallization. Some regions dry faster, leading to stress-induced cracks along GBs. Residual PbI_2 or organic halides segregate at GBs, creating electrically inactive regions. If polymers do not uniformly distribute, they can accumulate at GBs, disrupting charge transport. These methods are used to tackle the destructive effects of GBs. Additive engineering (*e.g.*, MACl and NH_4Cl) promotes Ostwald ripening for larger grains. Hot casting slows crystallization, yielding micrometer-sized grains. Lewis base additives bind to under-coordinated Pb^{2+} at GBs. Halide compensation (excess MAI/FAI) fills iodine vacancies at GBs. In 2D/3D perovskite hybrids, 2D layers cover GBs, improving stability. Some polymers with high film formation ability form a protective mesh around grains, reducing ion migration. Solvent vapor annealing heals GBs by partial re-dissolution and recrystallization.[270] Light soaking reduces trap density *via* photo-induced defect healing.[264] Ink rheology control ensures uniform nucleation and pre-patterning substrates guide grain alignment.

5.10.1.4 Pinholes and voids. Pinholes (nanoscale pores) and voids (larger empty regions) can form due to rapid solvent evaporation, poor wetting, or insufficient precursor coverage.[271] Unlike lab-scale spin-coated films, large-area printed PSCs are more prone to these defects due to process-related challenges. Fast-evaporating solvents (*e.g.*, DMF and acetone) cause uneven drying, leading to film shrinkage cracks and voids. Slow solvents (*e.g.*, DMSO and GBL) can induce coffee-ring effects, leaving pinholes. In the case of ink aggregation, perovskite precursor particles may clump together, creating gaps in the film. If the ink doesn't spread uniformly on the substrate, de-wetting occurs, leaving voids. Techniques like slot-die coating or inkjet printing dry unevenly, causing localized pinholes. Air bubbles trapped during ink dispensing burst, forming voids. If the perovskite doesn't bond well with the underlying layer (*e.g.*, TiO_2 and PEDOT:PSS), voids form. If crystallization occurs too fast (*e.g.*, in ambient air printing), pinholes appear where grains don't merge properly. Solvent escaping too quickly can leave behind voids. Strategies to minimize pinholes and voids are as follows. Mixed solvents improve wetting and slow drying. Polymer binders fill gaps and improve film continuity. Surfactants (*e.g.*, PEG and L-α-phosphatidylcholine) reduce surface tension for better spreading.[239] Vacuum-assisted deposition removes trapped air bubbles before film formation. Plasma/UV-ozone cleaning removes organic contaminants for better ink adhesion. Pre-heating substrates helps in controlled

Table 28 The effect of roughness types on the fundamental properties of perovskite solar cells and modules

Roughness type	Electrical effect	Optical effect	Stability effect
Nanoscale (<50 nm)	Increased trap-assisted recombination	Minimal scattering	Localized degradation
Sub-micron (50–500 nm)	Poor interfacial contact → higher R_s	Haze losses (~3–5% J_{SC})	Crack initiation sites
Micron-scale (>500 nm)	Shunting pathways → low FF	Severe scattering (>10% J_{SC} loss)	Delamination risks

crystallization. Exposing films to solvent vapors (*e.g.*, DMF and NMP) re-dissolves and recrystallizes perovskite, sealing pinholes.

5.10.1.5 Surface roughness. Surface roughness refers to the uneven topography of perovskite films at the nanoscale to microscale level.[272,273] In printed solar cells, excessive roughness creates interfacial problems that degrade performance and reproducibility, especially in large-area manufacturing. Performance impacts of roughness are presented in Table 28.

Rapid drying in techniques like slot-die coating leads to island growth rather than smooth films. Non-Newtonian behaviour of ink rheology causes uneven material deposition. Solute migration during drying creates raised edges and depressed centres (coffee-ring effect). High vapor pressure solvents (*e.g.*, chlorobenzene) cause abrupt phase separation. Poor ink-substrate adhesion causes dewetting patterns. Ether-based treatments yield smoother films than chlorobenzene.[274] Perovskite-quantum dot blends show very smooth surfaces.[275,276] The RMS roughness measurements showed values of 36.8 nm for the control perovskite film, 30.9 nm for the PVA-treated film, and 34.1 nm for the PEG-treated film. The reduction in roughness observed in the polymer-modified films is likely due to the development of a thin polymeric coating on the surface.[277–279]

5.10.1.6 Thermal instability. Some perovskite materials are sensitive to thermal stress during processing, which can cause defects or degradation. Thermal instability is a critical failure mode in printed PSCs, causing performance degradation and structural changes when exposed to temperature variations during manufacturing or operation.[280–282] Unlike single-crystal silicon solar cells that withstand >200 °C, perovskite devices degrade at much lower temperatures (typically 90–150 °C), creating unique challenges for printed large-area modules. Degradation pathways and their impacts based on temperature range are presented in Table 29. Some mitigation strategies are as follows. Cs^+/Rb^+ alloying suppresses phase segregation. 2D perovskite armor at grain boundaries leads to a good improvement. Thermal-stable polymers such as PTAA, and P3HT instead of spiro-OMeTAD are effective. Chloride incorporation (5–10%) delays ion migration.[283] Other items include UV-curable inks (<70 °C curing), and cold sintering techniques.

5.10.1.7 Coffee ring effect. Among these defects, the coffee ring effect is a common issue in the printing of PSCs.[284,285] This effect occurs when solute particles in a liquid are transported to and deposited at the edges of a drying droplet, forming a ring-like pattern similar to a coffee stain. The mechanism of coffee ring formation is as follows. Capillary flow: evaporation at the droplet edge creates an outward fluid flow to replenish lost solvents. Contact line pinning: the droplet perimeter remains fixed while the solvent evaporates. Marangoni effect (Ma): surface tension gradients can partially counteract outward flow (but often fail in perovskite inks). This significantly affects the uniformity and quality of printed films, especially in droplet-based deposition methods like inkjet or spray-coating. In PSCs, this effect can lead to non-uniform film thickness, poor morphology of the perovskite structure, and ultimately lower device performance. It can result in reduced internal quantum efficiency and increased charge recombination rate. Overcoming this defect is crucial for enhancing the efficiency and stability of printed PSCs. Polymers can play a vital role in eliminating the coffee ring effect by increasing the ink's viscosity, which reduces capillary flow and leads to more uniform film formation. Additionally, polymers can adjust the solvent evaporation rate, helping to form a uniform solute distribution as the ink dries, and can also modify the surface tension of the ink, influencing its wetting properties and flow behavior on the substrate, thus reducing the likelihood of coffee ring formation.

5.11 What is the role of polymers in large-scale production?

Polymers play a pivotal role in addressing the defects that arise during the large-scale printing of PSCs. Polymers can improve the quality of the perovskite film, leading to fewer defects such as pinholes or grain boundary issues. Polymers can act as a template or scaffold, guiding the crystallization of the perovskite material. This controlled growth helps to prevent the formation of defects that can arise from uncontrolled, rapid crystallization. Polymers can be used to passivate the surface of the perovskite layer. This means they fill in any existing pinholes or voids and also neutralize charge traps at the grain boundaries and surfaces of the perovskite crystals. This reduces

Table 29 Degradation pathways and their impacts

Temperature range	Primary degradation mode	Efficiency loss mechanism
50–70 °C	Ion migration begins	Increased J–V hysteresis
70–85 °C	MA^+ cation evaporation	V_{OC} drop (~100 mV)
85–100 °C	Halide segregation	Bandgap widening → J_{SC} loss
100–150 °C	PbI_2 crystallization	Shunting paths → FF collapse
>150 °C	Complete decomposition	Device failure

non-radiative recombination and improves charge extraction. Polymers can effectively mitigate defects in large-scale films of PSCs by addressing issues like the coffee-ring effect, improving crystal quality, and enhancing lattice stability. The introduction of an *in situ* polymer framework, such as poly(ethylene glycol) diacrylamide (PEGDAM), helps to modulate the Ma convection intensity within the precursor droplet.[286] The polymer framework increases the precursor's viscosity, which in turn reduces the Ma number, a value that represents the ratio of surface tension to viscous forces. A lower Ma value leads to a decrease in the intensity of Ma convection and weakens the microfluidic flocculation motion inside the droplet during solvent evaporation. The polymer framework slows down thermal capillary flow and homogenizes the heat transfer process across the film's surface, which contributes to regulating the coffee-ring effect.[286] The 3D network formed by the spontaneous cross-linking of the polymer at room temperature can anchor the flocculent movement of perovskite colloidal particles, counteracting the lateral capillary flow that causes the coffee-ring effect. The polymer framework can retard the crystallization rate of the perovskite precursor. It interacts with the perovskite components to form a complex, altering the nucleation energy barrier. This leads to the formation of a large number of nucleation sites in a short period, allowing sufficient time for subsequent crystal growth.[286] Strong interactions between the polymer and the perovskite in the wet-film state can restrain the generation of multiple intermediate phases and promote oriented crystal growth. Polymers remaining at the grain boundaries can passivate deep trap states, which facilitates improvements in both the PCE and the long-term stability of the perovskite devices. Residual stress in perovskite films can lead to lattice distortions and negatively impact the photovoltaic performance. The *in situ* polymer framework helps to release tensile stress.[286]

For large-scale production methods like blade-coating, the wettability of the surface is critical for depositing a uniform perovskite layer. Polymeric HTLs have shown distinct advantages over their small-molecule counterparts. According a study, polymeric HTLs such as poly-DBPP[287] and poly-2PACz exhibit better surface wettability compared to conventional self-assembled monolayer (SAM) HTLs.[288] This is because the polymer structure can present more hydrophilic groups (like phosphonic acid) on its surface, which helps the perovskite ink to spread more evenly during coating. The improved wettability and higher conductance of polymers like poly-2PACz, and poly-DBPP lead to better deposition homogeneity, which is confirmed by electroluminescence (EL) mapping that shows more uniform emission compared to devices using small-molecule HTLs (Fig. 32). This uniformity is crucial for large-area modules, where performance is often limited by the lowest-performing sub-cell.

The transition from a precursor ink to a solid, crystalline perovskite film is a delicate process that can easily introduce defects. Polymers can help manage this process. Specifically designed polymers, like poly-DBPP, can interact with lead cations in the precursor ink through their functional groups (biphosphonic acid). This interaction slows down the perovskite crystallization speed, which allows for the formation of a film with higher crystallinity and fewer defects.[287] By interacting with the perovskite precursors in the wet-film state, polymers like poly(*p*-xylylene) (PPX) can restrain the formation of undesirable intermediate phases and promote oriented crystallization.[289] Polymers can be applied as ultra-thin passivation layers on top of the perovskite film. For example, a ~1 nm layer of PPX deposited *via* CVD effectively passivates surface defects and trap states. This is demonstrated by a significant increase in PL intensity and a longer charge carrier lifetime, indicating a reduction in non-radiative recombination. Novel polymeric HTLs like poly-DBPP are designed with biphosphonic acid groups that can simultaneously bind to the underlying conductive substrate (ITO) and interact with the perovskite layer above. This dual interaction effectively passivates the crucial buried interface, reduces trap density, and suppresses charge recombination. In some advanced structures, a cross-linked polymer CLP can be used as an interlayer to inhibit the diffusion of mobile ions between different perovskite layers, which is a key mechanism for degradation and instability.[287] The hydrophobic nature of polymers like PPX allows them to act as

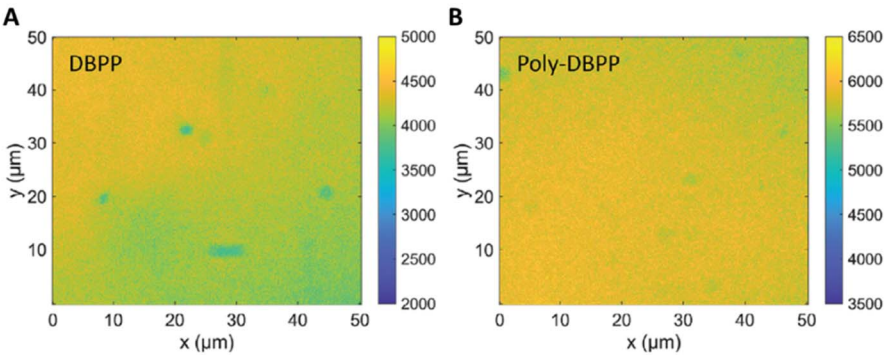

Fig. 32 EL intensity mapping of the blade-coated PSCs based on (A) small-molecule DBPP as the HTL. The map displays significant colour variation, with distinct patches of lower (greener) and higher (yellower) intensity. This indicates a non-uniform light emission across the surface of the cell. (B) Polymeric poly-DBPP as the HTL. In stark contrast to the DBPP-based cell, this map is much more uniform in color and exhibits a significantly higher overall EL intensity (indicated by the brighter, more yellow appearance). Reprinted from *Advanced Materials*, Wiley, Feifei Wang, *et al.*, 2025, under CC BY license.[286]

an effective barrier against moisture, a primary cause of perovskite degradation. Even a 1 nm layer of PPX can protect the perovskite film from degrading into lead iodide (PbI_2) when exposed to ambient air.[289] Conventional small-molecule SAM HTLs can suffer from poor UV stability, where UV radiation weakens their bond to the substrate and decomposes their molecular structure. In contrast, polymeric HTLs like poly-2PACz exhibit exceptional UV resistance, attributed to the delocalization of electrons along the conjugated polymer backbone and a stronger, more stable adhesion to the substrate. This allows devices to retain 80% of their initial efficiency even after nearly 500 hours of high-intensity UV illumination.[288]

The characteristics of the polymer used, including molecular weight, polydispersity, and interchain interactions, greatly affect the ink's viscosity and the performance of solar cells by influencing the absorbers' shape and mechanical properties.[290] Many high-performance polymers show temperature-dependent aggregation, meaning their properties change with temperature during processing.[291–293] Despite advancements in processing parameters, ensuring the scalability and consistency of polymers across different batches remains a significant challenge.

For example, PEO can adjust shear-thinning behavior for slot-die coating.[294] PEG and its family (PEGAD and PEGDAM) reduce the coffee-ring effect in printable perovskite solar cells.[295] PVP stabilizes colloidal perovskite precursors.[296,297] Fluorinated polymers such as PTFE reduce surface tension for uniform wetting on hydrophobic substrates.[102,298] PMMA passivates undercoordinated Pb^{2+} *via* carbonyl groups and PMMA can passivate defects in the perovskite film, reducing trap states that hinder charge transport. PMMA chains on PTAA create an interface dipole at the PTAA/perovskite junction due to electrostatic interactions between the ester groups in PMMA and the electron-deficient N^+ free radicals in PTAA. This physical adsorption enhances the V_{OC} by 60 mV and enables a PCE exceeding 20%, while also ensuring excellent stability.[299,300] PVA forms hydrogen bonds with perovskites, suppressing ion migration.[301] PDMS enables self-healing of cracks.[302]

Polymers are the linchpin of perovskite commercialization, bridging the gap between lab-scale innovation and GW-scale manufacturing. Future advancements will focus on AI-designed smart polymers that autonomously optimize device performance under real-world conditions.

While techniques exist to enhance the operational stability of research solar cells, such as developing polymeric and oligomeric non-fullerene acceptors (NFAs) with high thermal stability, there has been no research on suitable materials for large-scale processing. These materials significantly impact the film morphology, especially polymeric NFAs, posing a challenge for large-scale printing. Processing a precursor ink with a polymeric donor and acceptor is particularly difficult due to the high likelihood of polymer self-aggregation, leading to severe phase segregation between the two polymers.[303] This issue is especially pronounced when the meniscus-guided coating process involves slower solvent evaporation. Adding monoammonium zinc porphyrin as a surfactant to perovskite ink enhances the surface adherence of the precursor solution. It attaches to the surface of perovskite crystallites, preventing defect formation and cation escape. This leads to effective molecular encapsulation and surface passivation at grain boundaries and perovskite surfaces.[304]

The top CTL often serves as a passivator, reducing defects at the absorber surface and aiding in the extraction and transport of charge carriers. Conversely, the bottom CTL is crucial for templating film formation, significantly impacting the absorber's quality and overall device performance. Despite advancements in large-surface active layer printing methods, achieving uniform CTL thickness on flexible substrates with rough surfaces remains a challenge.[305,306]

Blade coating is commonly used for processing PTAA in inverted (p–i–n) PSCs. Fei and colleagues[307] reported a 26.9 cm^2 minimodule with a verified PCE of 21.8%, achieved by adding a small amount of bathocuproine (BCP), an ETL that can chelate with lead ions in the PTAA layer. This PTAA–BCP composite efficiently extracts and transports holes, improves the crystallinity of the perovskite layer near the HTL, and passivates the perovskite bottom surface, ensuring good contact between the perovskite layer and HTL.

6 Challenges and perspectives

In summary, we present our perspectives on the future commercialization of printable and flexible hybrid PSCs. To expedite the development of printable thin-film photovoltaics for practical applications, several critical issues must be addressed. These include production, operation, and the challenges of scaling up the production and deployment of PSCs. Addressing these challenges requires collaboration among researchers, engineers, and consumers. To realize the envisioned terawatt-scale deployment of solar panels, it is imperative to establish a dependable and robust supply chain for essential materials, ensuring the scalable production of thin-film photovoltaics. While key precursors for PSCs, such as lead iodide and formamidinium salts, are readily accessible, other critical components, particularly synthetic organics like NFAs or PTAA, remain relatively costly.

At present, the P3HT polymer stands out as the only photoactive conjugated polymer that can be synthesized in a controllable, scalable (from 100 g to kg scale), and highly reproducible manner, providing a sufficient supply at a reasonable cost. However, this scale is still significantly behind the scalability of perovskite precursor materials (kg to hundreds-of-kg scale) required for gigawatt-scale solar cell manufacturing, although it could suffice for pilot-line production.[308,309]

Modern polymer donors such as PBDBT, PM6, and J_{71} are structurally optimized, necessitating complex chemical structures and lengthy synthetic pathways. As a result, their synthesis is only reproducible at the laboratory scale (milligram to tens-of-gram scale). The use of rare metal palladium catalysts, the high cost of expensive precursors, and the less controllable synthesis due to strong polymer aggregation impede larger-scale synthesis. These polymers tend to precipitate out of reaction mixtures, making homogeneous polymerization, which results in substantial polydispersity of the crude product, extremely challenging. This process requires more time and solvents.

Although certain polymers have been utilized in blade-coated small-area devices instead of modules, there are other polymers available with simpler chemical structures, reduced production costs, and similar performance.[310] Furthermore, PTQ10 is notorious for its inconsistent batch-to-batch reproducibility, likely stemming from the non-regiospecific product formed during synthesis, which impacts its morphological and electrical properties.[311] Inconsistent molecular weights in polymers like PTAA, and P3HT lead to unpredictable hole mobility.[312] Machine learning-assisted polymerization monitoring was used for real-time control.[313] Stille/Suzuki coupling—used for N2200 and DPP-DTT—requires toxic Pd catalysts, limiting kg-scale production.[314]

To increase the scalability of these essential elements, synthetic methods need to be delicately engineered to better regulate reactions. Shin *et al.*[315] reported stepwise heating as a means of improving control over the polymerization reaction, producing the well-known PTB7 polymer with minimal batch-to-batch variation in a highly reproducible manner. Another approach is to create novel polymers whose characteristics are less dependent on their molecular weights. Recent studies suggest that terpolymers or even random polymers can more effectively address this issue, reducing the dependence of solar cell performance on the polymer batch.[316] However, this technique also reduces polymer crystallinity, resulting in slightly lower device performance compared to those using more structurally well-defined polymers. This issue could be resolved by gaining a deeper understanding of the relationships between polymer properties and structures, polymer physics in the solution phase, and the fluid dynamics of the precursor ink. Additionally, understanding how polymer self-assembly in solution impacts the morphology of the solar cell absorber is crucial. Defect-responsive smart polymers can be a good roadmap, polymers that dynamically passivate defects under operational stress (*e.g.*, thermally cross-linkable benzocyclobutene).[317]

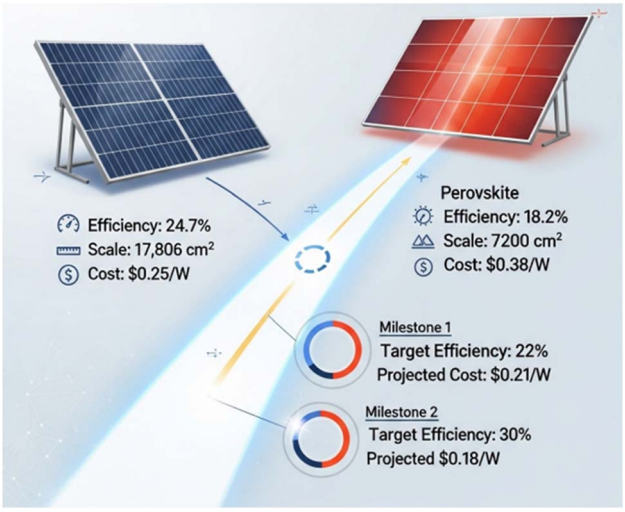

Fig. 33 The competitive landscape between established silicon solar technology and emerging perovskite solar technology, highlighting current performance and future cost-reduction pathways.

In the context of 2025, the techno-economic requirements for perovskite solar modules (PSMs) have become more clearly defined. Recent analyses indicate that rigid perovskite modules with a PCE of around 23% would need to achieve operational lifetimes of approximately 24 years to compete with crystalline silicon photovoltaics, while flexible perovskite modules would require about 17 years of stability at similar efficiency levels.[318]

From an economic perspective, the National Renewable Energy Laboratory (NREL) has recently assessed the minimum sustainable price (MSP) of perovskite–silicon tandem architectures. Their study suggests that two-terminal tandems could reach MSPs of about 0.428 $ per W_{DC}, while four-terminal designs are close at 0.423 $ per W_{DC}, depending on efficiency and production capacity [2,3].[319] In comparison, the current manufacturing cost of single-junction perovskite modules is estimated to be 0.57 $ per W, which remains higher than the benchmark for crystalline silicon. However, sensitivity analyses demonstrate that with further advances, specifically achieving higher than 25% PCE and operational lifetimes of more than 25 years, alongside reductions in material and equipment costs, perovskite modules could surpass silicon in terms of cost competitiveness.[320]

These updated projections highlight both the progress and the remaining challenges for perovskite solar technology. While current large-area PSMs still lag behind silicon in terms of cost and durability, the combination of improved stability, scalable manufacturing, and tandem designs points toward a viable economic pathway in the near future.

The PCE of a perovskite standard module is now reaching 18.2% at an area of 7200 cm^2 while the 24.7%-Si standard module is realized at an area of 17 806 cm^2. Besides, according to the calculation by the NREL, the minimum sustainable price (MSP, defined as the price that provides the minimum rate of return necessary in a given industry to support a sustainable business over a long term) with a 15%-gross margin of perovskite solar modulus manufactured at a small scale is calculated to be 0.38 $ per W, higher than that of c-Si (0.25–0.27 $ per W), but it is with possible reductions to 0.21 $ per W for a larger scale if PCE can be improved to 22% for a single-junction PSM without incurring additional costs. Further developing an all-perovskite two-junction tandem module with a PCE of 30% could lower the cost to 0.18 $ per W in the future (Fig. 33).[320]

7 Conclusion

Polymers, as a champion material, can significantly enhance the performance and stability of PSCs. The architecture of polymer passivation agents and their interaction with perovskite crystals are crucial factors. Features such as 3D structures and multiple functional groups with controllable configurations improve PSC performance. Selecting the most effective functional groups for the polymeric structure is essential. Polymers influence the kinetics of perovskite crystals during both nucleation and growth stages. Consequently, higher-quality hybrid PSCs exhibit more uniform film morphology, leading to lower series and transfer resistance, higher recombination resistance, and improved charge transfer and

extraction. Additionally, denser perovskite films with larger grains enhance vertical alignment, facilitating carrier transport. Certain moieties, such as benzene rings, and carbonyl, ester, amide, amine, thiophene, and carboxyl groups, effectively coordinate Pb^{2+} and anchor I^- ions.

SCPs hold even greater potential in PSCs. Engineering aspects like side chains, backbone, radius of gyration, Kuhn length, amorphous and crystalline regions, and intra- and inter-chain interactions can optimize light absorption, charge separation, and charge collection, alongside morphological control in PSCs. Future studies should investigate the effects of various structures, components, and chain factors in non-conducting and SCPs within different parts of PSCs in a systematic and targeted manner.

The future commercialization of printable solar cells hinges on addressing several critical issues related to production, operation, and scaling up the deployment of organic materials and PSCs. Collaboration among researchers, engineers, and consumers is essential to overcome these challenges. A reliable supply chain for essential materials is crucial for scalable thin-film photovoltaic production. While key precursors for PSCs are readily available, other components, particularly synthetic organics, remain costly. Modern polymers require complex synthesis processes, making large-scale production challenging due to high costs and synthesis difficulties. To improve scalability, synthetic methods must be refined to better control reactions. Approaches like stepwise heating and developing novel polymers less dependent on molecular weights can help, though they may impact polymer crystallinity and device performance. A deeper understanding of polymer properties, structure, and self-assembly in solution is crucial for advancing the field.

Conflicts of interest

The authors declare no conflict of interest.

Data availability

This manuscript is a review article that compiles, interprets, and discusses findings from previously published, peer-reviewed studies in reputable scientific journals. All data, results, and figures presented here are drawn directly from these original sources. Permissions have been secured for the reproduction of figures and any other materials, and full citations and acknowledgments are provided to appropriately credit the original authors and publications. No new primary data were produced or analyzed for this work. Additional details regarding sources or permissions for reproduced content can be obtained from the corresponding author upon request.

Acknowledgements

The authors gratefully acknowledge Dr Masoud Alahbakhshi for his valuable guidance, insightful discussions, and constructive feedback throughout the course of this research. His expertise and critical input significantly contributed to the development and refinement of this work. The authors wish to acknowledge the support of the Henry Royce Institute for Advanced Materials through the Industrial Collaboration Programme (RICP-R4-100061) and MATcelerateZero (MATZ0), funded from a grant provided by the Engineering and Physical Sciences Research Council EP/X527257/1. The authors acknowledge the Department for Energy Security and Net Zero (Project ID: NEXTCCUS), University College London's Research, Innovation and Global Engagement, University of Sydney – University College London Partnership Collaboration Awards, UCL-Peking University Strategic Partner Funds, Cornell-UCL Global Strategic Collaboration Awards and UCL – Korea University Strategic Partner Funds for their financial support. The authors acknowledge the ACT program (Accelerating CCS Technologies, Horizon 2020 Project No. 691712) for the financial support of the NEXTCCUS project (project ID: 327327).

References

1 Z. Huang, Z. Du, Z. Ma, Y. Zheng, Q. Zhang, W. You, J. Yang, T. Yu, S. Hou and G. Li, *Chem. Eng. J.*, 2024, **499**, 156684.
2 M. Knezevic, T.-H. Hoang, N. Rashid, M. Abdi-Jalebi, C. Colbeau-Justin and M. N. Ghazzal, *Sci. China Mater.*, 2023, **66**, 2545–2572.
3 T. Liu, R. A. Scheidt, X. Zheng, S. Joy, Q. Jiang, H. R. Atapattu, M. Chen, H. Pruett, K. Zhu and J. M. Luther, *Cell Rep. Phys. Sci.*, 2023, **4**, 1–17.
4 M. Li, H. Gao, L. Li, E. Wang, Z. Liu, I. T. Cheong, P. Wu, Y. Zhang, Y. Wang and X. Zheng, *Nat. Photonics*, 2025, 1–9.
5 Y. Guo, H. Tan and B. Xu, *Energy Environ. Sci.*, 2025, **18**, 8744–8755.
6 Y. Jiang, Z. Zhang, Y. Wang, J. Jin, Y. Huang, W. Wang, D. Ma, H. Huang, C. Chen and S. Ren, *Adv. Funct. Mater.*, 2025, 2504541.
7 M. Hu, Y. Zhu, Z. Zhou, M. Hao, C. Harnmanasvate, J. Waiyawat, Y. Wang, J. Lu, Q. An and X. Li, *Adv. Energy Mater.*, 2023, **13**, 2301888.
8 W. Cheng, R. Zhou, S. Peng, C. Wang and L. Chen, *Mater. Today Commun.*, 2023, 107879.
9 S. Hou, Z. Ma, Y. Li, Z. Du, Y. Chen, J. Yang, W. You, Q. Yang, T. Yu and Z. Huang, *Adv. Funct. Mater.*, 2024, **34**, 2310133.
10 G. S. H. Thien, K.-Y. Chan, M. A. M. Sarjidan, W. H. Abd Majid and B. K. Yap, *Appl. Surf. Sci. Adv.*, 2024, **19**, 100538.
11 M. Hu, Y. Zhu, Z. Zhou, M. Hao, C. Harnmanasvate, J. Waiyawat, Y. Wang, J. Lu, Q. An and X. Li, *Adv. Energy Mater.*, 2023, **13**, 2301888.
12 J. Yi, G. Zhang, H. Yu and H. Yan, *Nat. Rev. Mater.*, 2024, **9**, 46–62.
13 E. Akman, T. Ozturk, W. Xiang, F. Sadegh, D. Prochowicz, M. M. Tavakoli, P. Yadav, M. Yilmaz and S. Akin, *Energy Environ. Sci.*, 2023, **16**, 372–403.
14 Z. Fang, J. Sun, S. F. Liu and L. Ding, *J. Semicond.*, 2023, **44**, 080201.
15 J. Ye, M. M. Byranvand, C. O. Martínez, R. L. Z. Hoye, M. Saliba and L. Polavarapu, *Angew. Chem.*, 2021, **133**, 21804–21828.

16 A. Dey, P. Rathod and D. Kabra, *Adv. Opt. Mater.*, 2018, **6**, 1800109.
17 Q. Cai, Q. Tan, J. He, S. Tang, Q. Sun, D. He, T. Cheng, G. Ma, J. Huang and G. Su, *Joule*, 2025, 101880.
18 Y. Shi, W. Chu, L. Zhang, B. Wang, W. A. Saidi, J. Zhao and O. V Prezhdo, *Chem. Mater.*, 2025, **37**, 655–664.
19 G. Liu, M. Ghasemi, Q. Wei, B. Jia, Y. Yang and X. Wen, *Adv. Energy Mater.*, 2025, 2405239.
20 M. S. Hammer, H. Schlott, L. Lüer, C. J. Brabec, M. Sytnyk, J. Will, B. Meyer and W. Heiss, *Nat. Rev. Mater.*, 2025, 1–15.
21 X. Zhang, M. E. Turiansky, J.-X. Shen and C. G. Van de Walle, *Phys. Rev. B*, 2020, **101**(14), 140101.
22 I. du Fossé, J. T. Mulder, G. Almeida, A. G. M. Spruit, I. Infante, F. C. Grozema and A. J. Houtepen, *J. Am. Chem. Soc.*, 2022, **144**, 11059–11063.
23 Z. Guo, M. Yuan, G. Chen, F. Liu, R. Lu and W. Yin, *Adv. Sci.*, 2024, 2305799.
24 Y. Lei, Y. Xu, M. Wang, G. Zhu and Z. Jin, *Small*, 2021, **17**, 2005495.
25 G. J. W. Aalbers, T. P. A. van der Pol, K. Datta, W. H. M. Remmerswaal, M. M. Wienk and R. A. J. Janssen, *Nat. Commun.*, 2024, **15**, 1276.
26 J. Xia, C. Liang, H. Gu, S. Mei, S. Li, N. Zhang, S. Chen, Y. Cai and G. Xing, *Energy Environ. Mater.*, 2023, **6**, e12296.
27 J. Wang, L. Bi, Q. Fu and A. K. Jen, *Adv. Energy Mater.*, 2024, **14**, 2401414.
28 Y. Zhang, M. Abdi-Jalebi, B. W. Larson and F. Zhang, *Adv. Mater.*, 2024, **36**, 2404517.
29 Y. Chen, S. Tan, N. Li, B. Huang, X. Niu, L. Li, M. Sun, Y. Zhang, X. Zhang and C. Zhu, *Joule*, 2020, **4**, 1961–1976.
30 H. Cheng, X. Zang, S. Wang and B. Cai, *Sol. RRL*, 2025, **9**, 2400736.
31 W. Qi, X. Zhou, J. Li, J. Cheng, Y. Li, M. J. Ko, Y. Zhao and X. Zhang, *Sci. Bull.*, 2020, **65**, 2022–2032.
32 H. Guo, G. W. Yoon, Z. J. Li, Y. Yun, S. Lee, Y. Seo, N. J. Jeon, G. S. Han and H. S. Jung, *Adv. Energy Mater.*, 2024, **14**, 2302743.
33 J. Qin, Y. Chen, X. Guo, H. Yang, Y. Qin, C. Yao, B. Lv, Y. Bai and Y. Zhan, *Adv. Opt. Mater.*, 2023, **11**, 2202809.
34 P. Tang, M. Ameri, Q. Liang, P. I. Udenze, Z. Ouyang, M. Brown, L. Smith, I. Fedin and D. Li, *ACS Appl. Mater. Interfaces*, 2025, **17**, 31614–31626.
35 K. Chandratre, P. Sharma, S. Thomas, E. Parvazian, R. Patidar, R. Garcia-Rodriguez, E. Pean, R. Suthar, T. O. Dunlop and S. K. Pathak, *ACS Appl. Energy Mater.*, 2024, **7**, 5595–5607.
36 J. Xi, G. Zhao, X. Sun, S. Zhang, X. Du, J. Li, H. Yang, R. Wang, Z. Lu and G. Zou, *ChemNanoMat*, 2025, **11**, e202400478.
37 Y. Gou, S. Tang, C. Yuan, P. Zhao, J. Chen and H. Yu, *Mater. Horiz.*, 2024, **11**, 3465–3481.
38 Z. Wu, S. Sang, J. Zheng, Q. Gao, B. Huang, F. Li, K. Sun and S. Chen, *Angew. Chem., Int. Ed.*, 2024, **63**, e202319170.
39 F. Liu, J. Dou, W. Zhang, Y. Li, Y. Mei, Q. Guo, Q. Chen, Y. Zhao, Y. Wang and X. Zhang, *ACS Energy Lett.*, 2025, **10**, 4091–4101.
40 L. Zuo, H. Guo, D. W. deQuilettes, S. Jariwala, N. De Marco, S. Dong, R. DeBlock, D. S. Ginger, B. Dunn and M. Wang, *Sci. Adv.*, 2017, **3**, e1700106.
41 J. Ma, S. Fan, C. Shao, L. Wang, Y. Dong, G. Niu, Z. Nie, S. Yang, J. Wang and H. Yang, *Angew. Chem.*, 2025, **137**, e202425578.
42 M. Zhang, B. He, B. Yang, Z. Yang, H. Sui, H. Chen, J. Duan and Q. Tang, *Chem. Eng. J.*, 2025, 165948.
43 T. Li, P. Zhang, S. Wei, Y. Jing, J. Shi, Y. Chen, H. Zhong and G. Yang, *Adv. Opt. Mater.*, 2024, **12**, 2400486.
44 X. Huang, B. Wu and N. Zheng, *Acc. Mater. Res.*, 2024, **6**, 40–51.
45 S. Li, X. Xu, X. Wang, N. Huang, J. Fang, D. Lin, Y. Shao, J. Zhou, A. K. K. Kyaw and S. He, *Angew. Chem., Int. Ed.*, 2025, **64**, e202421174.
46 Y. Yang, N. Yang, C. Zhang, S. Li, Y. Hao, Q. Sun, Z. Chen, S. Liu, F. Guo and J. Lu, *Adv. Sci.*, 2025, e08253.
47 Z. Zhu, K. Mao, K. Zhang, W. Peng, J. Zhang, H. Meng, S. Cheng, T. Li, H. Lin and Q. Chen, *Joule*, 2022, **6**, 2849–2868.
48 M. Li, R. Sun, J. Chang, J. Dong, Q. Tian, H. Wang, Z. Li, P. Yang, H. Shi and C. Yang, *Nat. Commun.*, 2023, **14**, 573.
49 Y. Wu, G. Xu, J. Xi, Y. Shen, X. Wu, X. Tang, J. Ding, H. Yang, Q. Cheng and Z. Chen, *Joule*, 2023, **7**, 398–415.
50 C. Zhao, H. Zhang, M. Almalki, J. Xu, A. Krishna, F. T. Eickemeyer, J. Gao, Y. M. Wu, S. M. Zakeeruddin and J. Chu, *Adv. Mater.*, 2023, **35**, 2211619.
51 Z. Huang, X. Hu, C. Liu, X. Meng, Z. Huang, J. Yang, X. Duan, J. Long, Z. Zhao and L. Tan, *Adv. Funct. Mater.*, 2019, **29**, 1902629.
52 D. Wang, L. Zhang, K. Deng, W. Zhang, J. Song, J. Wu and Z. Lan, *Energy Technol.*, 2018, **6**, 2380–2386.
53 K. Ma, H. R. Atapattu, Q. Zhao, Y. Gao, B. P. Finkenauer, K. Wang, K. Chen, S. M. Park, A. H. Coffey and C. Zhu, *Adv. Mater.*, 2021, **33**, 2100791.
54 Y. Zou, W. Yu, Z. Tang, X. Li, H. Guo, G. Liu, Q. Zhang, Y. Zhang, Z. Zhang and C. Wu, *Appl. Phys. Lett.*, 2021, **119**(15), 151104.
55 K. Suwa, K. Oyaizu, H. Segawa and H. Nishide, *ChemSusChem*, 2019, **12**, 5207–5212.
56 T. Wang, Y. Li, Q. Cao, J. Yang, B. Yang, X. Pu, Y. Zhang, J. Zhao, Y. Zhang and H. Chen, *Energy Environ. Sci.*, 2022, **15**, 4414–4424.
57 M. Li, R. Sun, J. Chang, J. Dong, Q. Tian, H. Wang, Z. Li, P. Yang, H. Shi and C. Yang, *Nat. Commun.*, 2023, **14**, 573.
58 Y. Zhao, J. Wei, H. Li, Y. Yan, W. Zhou, D. Yu and Q. Zhao, *Nat. Commun.*, 2016, **7**, 10228.
59 C. Zhao, H. Zhang, M. Almalki, J. Xu, A. Krishna, F. T. Eickemeyer, J. Gao, Y. M. Wu, S. M. Zakeeruddin and J. Chu, *Adv. Mater.*, 2023, **35**, 2211619.
60 Y. Shen, G. Xu, J. Li, X. Lin, F. Yang, H. Yang, W. Chen, Y. Wu, X. Wu and Q. Cheng, *Angew. Chem.*, 2023, **135**, e202300690.
61 S. Lin, S. Wu, D. Guo, H. Huang, X. Zhou, D. Zhang, K. Zhou, W. Zhang, Y. Hu and Y. Gao, *Small Methods*, 2023, **7**, 2201663.

62 S. Valero, T. Soria, N. Marinova and J. L. Delgado, *Polym. Chem.*, 2019, **10**, 5726–5736.
63 Q. Dong, Z. Wang, K. Zhang, H. Yu, P. Huang, X. Liu, Y. Zhou, N. Chen and B. Song, *Nanoscale*, 2016, **8**, 5552–5558.
64 C.-C. Zhang, M. Li, Z.-K. Wang, Y.-R. Jiang, H.-R. Liu, Y.-G. Yang, X.-Y. Gao and H. Ma, *J. Mater. Chem. A*, 2017, **5**, 2572–2579.
65 A. Fakharuddin, M. Seybold, A. Agresti, S. Pescetelli, F. Matteocci, M. I. Haider, S. T. Birkhold, H. Hu, R. Giridharagopal and M. Sultan, *ACS Appl. Mater. Interfaces*, 2018, **10**, 42542–42551.
66 J. Jiang, Q. Wang, Z. Jin, X. Zhang, J. Lei, H. Bin, Z. Zhang, Y. Li and S. Liu, *Adv. Energy Mater.*, 2018, **8**, 1701757.
67 T.-H. Han, J.-W. Lee, C. Choi, S. Tan, C. Lee, Y. Zhao, Z. Dai, N. De Marco, S.-J. Lee and S.-H. Bae, *Nat. Commun.*, 2019, **10**, 520.
68 H. Zheng, X. Xu, S. Xu, G. Liu, S. Chen, X. Zhang, T. Chen and X. Pan, *J. Mater. Chem. C*, 2019, **7**, 4441–4448.
69 S. Collavini, M. Saliba, W. R. Tress, P. J. Holzhey, S. F. Völker, K. Domanski, S. H. Turren-Cruz, A. Ummadisingu, S. M. Zakeeruddin and A. Hagfeldt, *ChemSusChem*, 2018, **11**, 1032–1039.
70 B. Zhang, C. Chen, X. Wang, X. Du, D. Liu, X. Sun, Z. Li, L. Hao, C. Gao and Y. Li, *Angew. Chem., Int. Ed.*, 2023, **62**, e202213478.
71 B. Yu, L. Zhang, J. Wu, K. Liu, H. Wu, J. Shi, Y. Luo, D. Li, Z. Bo and Q. Meng, *J. Mater. Chem. A*, 2020, **8**, 1417–1424.
72 Q. Cao, T. Wang, J. Yang, Y. Zhang, Y. Li, X. Pu, J. Zhao, H. Chen, X. Li and I. Tojiboyev, *Adv. Funct. Mater.*, 2022, **32**, 2201036.
73 T. Zheng, Q. Zhou, T. Yang, Y. Zhao, B. Fan, J. Bo, L. Fan and R. Peng, *Carbon*, 2022, **196**, 213–219.
74 C. S. Pathak, G. Paramasivam, F. Mathies, K. Hirselandt, V. Schröder, O. Maus, J. Dagar, C. Klimm, E. Unger and I. Visoly-Fisher, *ACS Appl. Energy Mater.*, 2022, **5**, 4085–4095.
75 W. Chen, Y. Wang, G. Pang, C. W. Koh, A. B. Djurišić, Y. Wu, B. Tu, F. Liu, R. Chen and H. Y. Woo, *Adv. Funct. Mater.*, 2019, **29**, 1808855.
76 N. Chen, X. Yi, J. Zhuang, Y. Wei, Y. Zhang, F. Wang, S. Cao, C. Li and J. Wang, *Nano-Micro Lett.*, 2020, **12**, 1–13.
77 R. Garai, R. K. Gupta, A. S. Tanwar, M. Hossain and P. K. Iyer, *Chem. Mater.*, 2021, **33**, 5709–5717.
78 F. Li, J. Yuan, X. Ling, Y. Zhang, Y. Yang, S. H. Cheung, C. H. Y. Ho, X. Gao and W. Ma, *Adv. Funct. Mater.*, 2018, **28**, 1706377.
79 Y. Xu, G. Liu, J. Hu, G. Wang, M. Chen, Y. Chen, M. Li, H. Zhang and Y. Chen, *J. Phys. Chem. Lett.*, 2022, **13**, 3754–3762.
80 K. Kim, J. Han, S. Lee, S. Kim, J. Choi, J. Nam, D. Kim, I. Chung, T. Kim and S. Manzhos, *Adv. Energy Mater.*, 2023, **13**, 2203742.
81 X. Meng, Z. Xing, X. Hu, Z. Huang, T. Hu, L. Tan, F. Li and Y. Chen, *Angew. Chem., Int. Ed.*, 2020, **59**, 16602–16608.
82 T. Han, Y. Zhao, J. Yoon, J. Y. Woo, E. Cho, W. D. Kim, C. Lee, J. Lee, J. Choi and J. Han, *Adv. Funct. Mater.*, 2022, **32**, 2207142.
83 C. Zhang, Z. Wang, S. Yuan, R. Wang, M. Li, M. F. Jimoh, L. Liao and Y. Yang, *Adv. Mater.*, 2019, **31**, 1902222.
84 N. Jiang, B. Xing, Y. Wang, H. Zhang, D. Yin, Y. Liu, Y. Bi, L. Zhang, J. Feng and H. Sun, *Sci. Bull.*, 2022, **67**, 794–802.
85 Y. Zhao, P. Zhu, M. Wang, S. Huang, Z. Zhao, S. Tan, T. Han, J. Lee, T. Huang and R. Wang, *Adv. Mater.*, 2020, **32**, 1907769.
86 G. Li, Z. Su, L. Canil, D. Hughes, M. H. Aldamasy, J. Dagar, S. Trofimov, L. Wang, W. Zuo and J. J. Jerónimo-Rendon, *Science*, 2023, **379**, 399–403.
87 B. P. Finkenauer, Y. Gao, X. Wang, Y. Tian, Z. Wei, C. Zhu, D. J. Rokke, L. Jin, L. Meng and Y. Yang, *Cell Rep. Phys. Sci.*, 2021, **2**(2), 100320.
88 Q. Cao, J. Yang, T. Wang, Y. Li, X. Pu, J. Zhao, Y. Zhang, H. Zhou, X. Li and X. Li, *Energy Environ. Sci.*, 2021, **14**, 5406–5415.
89 Y. Lan, Y. Wang and Y. Song, *Flexible Printed Electron.*, 2020, **5**, 014001.
90 L. Wang, G. Liu, X. Xi, G. Yang, L. Hu, B. Zhu, Y. He, Y. Liu, H. Qian and S. Zhang, *Crystals*, 2022, **12**, 894.
91 Z. Huang, X. Hu, C. Liu, L. Tan and Y. Chen, *Adv. Funct. Mater.*, 2017, **27**, 1703061.
92 X. Duan, X. Li, L. Tan, Z. Huang, J. Yang, G. Liu, Z. Lin and Y. Chen, *Adv. Mater.*, 2020, **32**, 2000617.
93 M. Hu, Y. Zhu, Z. Zhou, M. Hao, C. Harnmanasvate, J. Waiyawat, Y. Wang, J. Lu, Q. An and X. Li, *Adv. Energy Mater.*, 2023, **13**, 2301888.
94 C. Liu, K. Huang, B. Hu, Y. Li, L. Zhang, X. Zhou, Y. Liu, Z. Liu, Y. Sheng and S. Chen, *Adv. Funct. Mater.*, 2023, **33**, 2212698.
95 L. Shen, P. Song, L. Zheng, L. Wang, X. Zhang, K. Liu, Y. Liang, W. Tian, Y. Luo and J. Qiu, *Adv. Mater.*, 2023, **35**, 2301624.
96 H. Huang, X. Zhang, W. Zhou, Y. Huang, Z. Zheng, X. Chen, Y. Zhang and H. Yan, *Mater. Chem. Front.*, 2024, **8**, 3528–3557.
97 D. Liu, X. Wang, X. Wang, B. Zhang, X. Sun, Z. Li, Z. Shao, S. Mao, L. Wang and G. Cui, *Angew. Chem., Int. Ed.*, 2023, **62**, e202301574.
98 N. Yan, Z. Fang, Z. Dai, J. Feng and S. Liu, *Adv. Funct. Mater.*, 2024, **34**, 2314039.
99 Z. Cai, Z. Yao, Z. Xing, R. Dai, Z. Huang, X. Meng, X. Hu and Y. Chen, *Adv. Funct. Mater.*, 2025, 2505921.
100 X. Zhao, R. Luo, C. Yu, X. Xu, W. Zhu, Y. Min and N. Cai, *Adv. Funct. Mater.*, 2024, **34**, 2307568.
101 H. Wang, Y. Zheng, G. Zhang, P. Wang, X. Sui, H. Yuan, Y. Shi, G. Zhang, G. Ding and Y. Li, *Adv. Mater.*, 2024, **36**, 2307855.
102 G. D. Tabi, D.-T. Nguyen, W. Liang, W. Ji, T. Lu, T. Trần-Phú, O. L. C. Lem, A. O. Mayon, K. Huang and L.-C. Chang, *Chem. Eng. J.*, 2024, **482**, 149062.
103 B. Zhang, C. Chen, X. Wang, X. Du, D. Liu, X. Sun, Z. Li, L. Hao, C. Gao and Y. Li, *Angew. Chem., Int. Ed.*, 2023, **62**, e202213478.
104 X. Tang, C. Yang, Y. Xu, J. Xia, B. Li, M. Li, Y. Zhou, L. Jiang, H. Liu and K. Ma, *Nat. Photonics*, 2025, 1–8.

105 Z. Li, C. Jia, Z. Wan, J. Xue, J. Cao, M. Zhang, C. Li, J. Shen, C. Zhang and Z. Li, *Nat. Commun.*, 2023, **14**, 6451.
106 H. Chen, H. Lin, Z. Sun, H. Li, C. He and D. Mao, *J. Mater. Chem. A*, 2023, **11**, 2443–2451.
107 Z. Li, C. Jia, Z. Wan, J. Cao, J. Shi, J. Xue, X. Liu, H. Wu, C. Xiao and C. Li, *Nat. Commun.*, 2025, **16**, 1771.
108 S. You, H. Zeng, Z. Ku, X. Wang, Z. Wang, Y. Rong, Y. Zhao, X. Zheng, L. Luo and L. Li, *Adv. Mater.*, 2020, **32**, 2003990.
109 F. Qin, W. Meng, J. Fan, C. Ge, B. Luo, R. Ge, L. Hu, F. Jiang, T. Liu and Y. Jiang, *ACS Appl. Mater. Interfaces*, 2017, **9**, 26045–26051.
110 J. Wei, F. Guo, X. Wang, K. Xu, M. Lei, Y. Liang, Y. Zhao and D. Xu, *Adv. Mater.*, 2018, **30**, 1805153.
111 Z. Xiong, L. Lan, Y. Wang, C. Lu, S. Qin, S. Chen, L. Zhou, C. Zhu, S. Li and L. Meng, *ACS Energy Lett.*, 2021, **6**, 3824–3830.
112 J. Duan, Y. Liu, X. Chen, S. Huang, W. Ou-Yang, G. Zhu, S. Zhang and Z. Sun, *Org. Electron.*, 2020, **82**, 105737.
113 J. Peng, J. I. Khan, W. Liu, E. Ugur, T. Duong, Y. Wu, H. Shen, K. Wang, H. Dang and E. Aydin, *Adv. Energy Mater.*, 2018, **8**, 1801208.
114 D. Li, Y. Huang, R. Ma, H. Liu, Q. Liang, Y. Han, Z. Ren, K. Liu, P. W. Fong and Z. Zhang, *Adv. Energy Mater.*, 2023, **13**, 2204247.
115 D. Yang, X. Zhang, K. Wang, C. Wu, R. Yang, Y. Hou, Y. Jiang, S. Liu and S. Priya, *Nano Lett.*, 2019, **19**, 3313–3320.
116 J. Peng, D. Walter, Y. Ren, M. Tebyetekerwa, Y. Wu, T. Duong, Q. Lin, J. Li, T. Lu and M. A. Mahmud, *Science*, 2021, **371**, 390–395.
117 J. Tian, Q. Xue, X. Tang, Y. Chen, N. Li, Z. Hu, T. Shi, X. Wang, F. Huang and C. J. Brabec, *Adv. Mater.*, 2019, **31**, 1901152.
118 Y. Yue, T. Umeyama, Y. Kohara, H. Kashio, M. Itoh, S. Ito, E. Sivaniah and H. Imahori, *J. Phys. Chem. C*, 2015, **119**, 22847–22854.
119 M. Jiang, Q. Niu, X. Tang, H. Zhang, H. Xu, W. Huang, J. Yao, B. Yan and R. Xia, *Polymers*, 2019, **11**, 147.
120 J. Zhou, X. Tian, R. Chen, W. Chen, X. Meng, X. Guan, J. Wang, S. Liu, F. Ren and S. Zhang, *Chem. Eng. J.*, 2023, **461**, 141914.
121 Z. Zhu, Q. Xue, H. He, K. Jiang, Z. Hu, Y. Bai, T. Zhang, S. Xiao, K. Gundogdu and B. R. Gautam, *Adv. Sci.*, 2015, **3**, 1500353.
122 F. Tan, H. Tan, M. I. Saidaminov, M. Wei, M. Liu, A. Mei, P. Li, B. Zhang, C. Tan and X. Gong, *Adv. Mater.*, 2019, **31**, 1807435.
123 E. Akman and S. Akin, *Adv. Mater.*, 2021, **33**, 2006087.
124 A. N. Mikheeva, I. E. Kuznetsov, M. M. Tepliakova, A. Elakshar, M. V Gapanovich, Y. G. Gladush, E. O. Perepelitsina, M. E. Sideltsev, A. F. Akhkiamova and A. A. Piryazev, *Molecules*, 2022, **27**, 8333.
125 Q. Fu, H. Liu, X. Tang, R. Wang, M. Chen and Y. Liu, *ACS Energy Lett.*, 2022, **7**, 1128–1136.
126 H. Hwang, S. Park, J. H. Heo, W. Kim, H. Ahn, T.-S. Kim, S. H. Im and H. J. Son, *J. Power Sources*, 2019, **418**, 167–175.
127 J. Ali, J. Song, Y. Li, K. Qian, Q. Zhang, G. Zhou, M. Zhang, L. Zhu, C. Qiu and J. Xu, *J. Mater. Chem. C*, 2019, **7**, 11932–11942.
128 M. Wang, Y. Zhao, X. Jiang, Y. Yin, I. Yavuz, P. Zhu, A. Zhang, G. S. Han, H. S. Jung and Y. Zhou, *Joule*, 2022, **6**, 1032–1048.
129 F. Zhang, J. Song, R. Hu, Y. Xiang, J. He, Y. Hao, J. Lian, B. Zhang, P. Zeng and J. Qu, *Small*, 2018, **14**, 1704007.
130 M. Li, X. Yan, Z. Kang, Y. Huan, Y. Li, R. Zhang and Y. Zhang, *ACS Appl. Mater. Interfaces*, 2018, **10**, 18787–18795.
131 B. Li, Y. Xiang, K. D. G. I. Jayawardena, D. Luo, J. F. Watts, S. Hinder, H. Li, V. Ferguson, H. Luo and R. Zhu, *Sol. RRL*, 2020, **4**, 2000060.
132 L. Meng, C. Sun, R. Wang, W. Huang, Z. Zhao, P. Sun, T. Huang, J. Xue, J.-W. Lee and C. Zhu, *J. Am. Chem. Soc.*, 2018, **140**, 17255–17262.
133 C. Geffroy, E. Grana, T. Bessho, S. Almosni, Z. Tang, A. Sharma, T. Kinoshita, F. Awai, E. Cloutet and T. Toupance, *ACS Appl. Energy Mater.*, 2020, **3**, 1393–1401.
134 M. Luo, X. Zong, M. Zhao, Z. Sun, Y. Chen, M. Liang, Y. Wu and S. Xue, *Chem. Eng. J.*, 2022, **442**, 136136.
135 Y. Zhang, Y. Ren, X. Xie, Y. Wei, L. He, L. Fang, J. Zhang, Y. Yuan and P. Wang, *Adv. Funct. Mater.*, 2022, **32**, 2108855.
136 G. You, L. Li, S. Wang, J. Cao, L. Yao, W. Cai, Z. Zhou, K. Li, Z. Lin and H. Zhen, *Adv. Energy Mater.*, 2022, **12**, 2102697.
137 D. H. Lee, S. Lim, C. Kim, H. U. Lee, D. Chung, Y. Choi, J. Choi, Y. Kim, S. B. Cho and H. Il Kim, *ACS Energy Lett.*, 2023, **8**, 1839–1847.
138 X. Wu, D. Gao, X. Sun, S. Zhang, Q. Wang, B. Li, Z. Li, M. Qin, X. Jiang and C. Zhang, *Adv. Mater.*, 2023, **35**, 2208431.
139 Y. Bai, Z. Zhou, Q. Xue, C. Liu, N. Li, H. Tang, J. Zhang, X. Xia, J. Zhang and X. Lu, *Adv. Mater.*, 2022, **34**, 2110587.
140 S. Y. Son, K. Choi, J. Lee, H. Il Kim, T. Park and M. Kim, *Chem. Mater.*, 2022, **34**, 4856–4864.
141 J. Wang, Z. Yu, D. D. Astridge, Z. Ni, L. Zhao, B. Chen, M. Wang, Y. Zhou, G. Yang and X. Dai, *ACS Energy Lett.*, 2022, **7**, 3353–3361.
142 H. Lin, T. Doba, W. Sato, Y. Matsuo, R. Shang and E. Nakamura, *Angew. Chem., Int. Ed.*, 2022, **61**, e202203949.
143 X. Meng, Z. Cai, Y. Zhang, X. Hu, Z. Xing, Z. Huang, Z. Huang, Y. Cui, T. Hu and M. Su, *Nat. Commun.*, 2020, **11**, 3016.
144 F. Wu, Q. Xiao, X. Sun, T. Wu, Y. Hua and L. Zhu, *Chem. Eng. J.*, 2022, **445**, 136760.
145 C. Y. Xu, W. Hu, G. Wang, L. Niu, A. M. Elseman, L. Liao, Y. Yao, G. Xu, L. Luo and D. Liu, *ACS Nano*, 2019, **14**, 196–203.
146 L. Wan, Y. Zhao, Y. Tan, L. Lou and Z.-S. Wang, *Chem. Eng. J.*, 2023, **455**, 140569.
147 K. Eom, U. Kwon, S. S. Kalanur, H. J. Park and H. Seo, *J. Mater. Chem. A*, 2017, **5**, 2563–2571.
148 R. Wang, L. Xie, T. Wu, C. Ge and Y. Hua, *Chem. Sci.*, 2023, **14**, 2877–2886.

149 Z. Iqbal, F. Zu, A. Musiienko, E. Gutierrez-Partida, H. Köbler, T. W. Gries, G. V Sannino, L. Canil, N. Koch and M. Stolterfoht, *ACS Energy Lett.*, 2023, **8**, 4304–4314.
150 H. Li, G. Xie, X. Wang, S. Li, D. Lin, J. Fang, D. Wang, W. Huang and L. Qiu, *Adv. Sci.*, 2023, **10**, 2300586.
151 E. Ochoa-Martinez, M. Ochoa, R. D. Ortuso, P. Ferdowsi, R. Carron, A. N. Tiwari, U. Steiner and M. Saliba, *ACS Energy Lett.*, 2021, **6**, 2626–2634.
152 A. Facchetti, *Chem. Mater.*, 2011, **23**, 733–758.
153 A. Facchetti, *Chem. Mater.*, 2011, **23**, 733–758.
154 W. Barford, *Electronic and Optical Properties of Conjugated Polymers*, OUP Oxford, 2013, vol. 129.
155 Z. Zhou, N. Luo, X. Shao, H. Zhang and Z. Liu, *ChemPlusChem*, 2023, **88**, e202300261.
156 J. Qiao, C. Yang, Q. He, F. Bai and Y. Li, *J. Appl. Polym. Sci.*, 2004, **92**, 1459–1466.
157 R. S. Kularatne, H. D. Magurudeniya, P. Sista, M. C. Biewer and M. C. Stefan, *J. Polym. Sci., Part A: Polym. Chem.*, 2013, **51**, 743–768.
158 C. Yang, B. Cheng, J. Xu, J. Yu and S. Cao, *EnergyChem*, 2024, **6**, 100116.
159 H. Zheng, X. Xu, S. Xu, G. Liu, S. Chen, X. Zhang, T. Chen and X. Pan, *J. Mater. Chem. C*, 2019, **7**, 4441–4448.
160 S. Valero, T. Soria, N. Marinova and J. L. Delgado, *Polym. Chem.*, 2019, **10**, 5726–5736.
161 N. Yaghoobi Nia, M. Bonomo, M. Zendehdel, E. Lamanna, M. M. H. Desoky, B. Paci, F. Zurlo, A. Generosi, C. Barolo and G. Viscardi, *ACS Sustain. Chem. Eng.*, 2021, **9**, 5061–5073.
162 J. Jiang, Q. Wang, Z. Jin, X. Zhang, J. Lei, H. Bin, Z. Zhang, Y. Li and S. Liu, *Adv. Energy Mater.*, 2018, **8**, 1701757.
163 T. Pratyusha, G. Sivakumar, D. Gupta and A. Yella, *Mater. Today Proc.*, 2017, **4**, 6820–6826.
164 N. Yaghoobi Nia, M. Mendez, B. Paci, A. Generosi, A. Di Carlo and E. Palomares, *ACS Appl. Energy Mater.*, 2020, **3**, 6853–6859.
165 L. Shen, T. Zhu, X. Zhang, K. Gong, H. Wang and X. Gong, *Nano Energy*, 2022, **93**, 106907.
166 F. Li, J. Yuan, X. Ling, Y. Zhang, Y. Yang, S. H. Cheung, C. H. Y. Ho, X. Gao and W. Ma, *Adv. Funct. Mater.*, 2018, **28**, 1706377.
167 C. Ren, Y. He, S. Li, Q. Sun, Y. Liu, Y. Wu, Y. Cui, Z. Li, H. Wang and Y. Hao, *Org. Electron.*, 2019, **70**, 292–299.
168 A. F. Akbulatov, E. A. Khakina, N. A. Emelianov, O. A. Kraevaya, L. A. Frolova and P. A. Troshin, *Sustain. Energy Fuels*, 2024, **8**, 4638–4645.
169 T. Chakrabarti, S. Kaarthik and A. Perumal, *ACS Appl. Energy Mater.*, 2025, **8**(5), 2837–2844.
170 H. Choi, S. U. Ryu, D. H. Lee, H. Kim, S. Song, H. Il Kim and T. Park, *ACS Energy Lett.*, 2024, **9**, 3136–3168.
171 R. L. Carey, S. Giannini, S. Schott, V. Lemaur, M. Xiao, S. Prodhan, L. Wang, M. Bovoloni, C. Quarti and D. Beljonne, *Nat. Commun.*, 2024, **15**, 288.
172 T. Pratyusha, G. Sivakumar, D. Gupta and A. Yella, *Mater. Today Proc.*, 2017, **4**, 6820–6826.
173 J. Grey, *Nat. Mater.*, 2016, **15**, 705–706.
174 L. Ding, Z.-D. Yu, X.-Y. Wang, Z.-F. Yao, Y. Lu, C.-Y. Yang, J.-Y. Wang and J. Pei, *Chem. Rev.*, 2023, **123**, 7421–7497.
175 Z. Ren, Z. Yang, W. Mu, T. Liu, X. Liu and Q. Wang, *Adv. Mater.*, 2025, **37**, 2416314.
176 F. He, T. Li, T. Shen, Y. Zhao, Z. Jin, Z. Zhang, Y. Pu, L. Deng, L. Qin and Y. Zhan, *Adv. Funct. Mater.*, 2024, 2405611.
177 S. Kim, S. Sabury, C. A. R. Perini, T. Hossain, A. O. Yusuf, X. Xiao, R. Li, K. R. Graham, J. R. Reynolds and J.-P. Correa-Baena, *ACS Energy Lett.*, 2024, **9**, 4501–4508.
178 Z. Xie, J. Park, H. Kim, B. H. Cho, C. Lakshman, H.-Y. Park, T. Gokulnath, Y.-Y. Kim, J. Yoon and J.-S. Jee, *ACS Appl. Mater. Interfaces*, 2024, **16**, 3359–3367.
179 Z. Azher, S. M. Said, A. Mainal, E. Y. Putri, H. F. B. Hizaddin, S. B. Ibrahim, N. Muhammad Sarih and M. U. Bin Mohd Junaidi, *Int. J. Green Energy*, 2024, 1–24.
180 L. Shen, X. Zhang, L. Liu, H. Sawwan, T. Zhu and X. Gong, *ACS Appl. Electron. Mater.*, 2024, **6**, 3925–3932.
181 I. R. Nikolényi and J. Tóth, *J. Magn. Magn. Mater.*, 2021, **517**, 167281.
182 D. Molina, M. J. Álvaro-Martins and Á. Sastre-Santos, *J. Mater. Chem. C*, 2021, **9**, 16078–16109.
183 J. Wu, C. Fu, R. M. Pankow, Y. Chen, D. Zheng, Z. Lu, Y. Huang, T. J. Marks and A. Facchetti, *Chem. Mater.*, 2023, **35**, 10106–10118.
184 C. Gedeon, N. Del Rio, F. Furlan, A. Taddeucci, N. Vanthuyne, V. G. Gregoriou, M. J. Fuchter, G. Siligardi, N. Gasparini and J. Crassous, *Adv. Mater.*, 2024, 2314337.
185 Z. Xing, S. Li, M. An and S. Yang, *ChemSusChem*, 2024, **17**, e202301662.
186 M. Zhang, H. Liu, Y. Liu, M. Zeng, B. Zhao and S. Tan, *Energy Fuels*, 2023, **37**, 6122–6128.
187 Z. Xie, J. Park, H. Kim, B. H. Cho, C. Lakshman, H.-Y. Park, T. Gokulnath, Y.-Y. Kim, J. Yoon and J.-S. Jee, *ACS Appl. Mater. Interfaces*, 2024, **16**, 3359–3367.
188 C. Liu, L. Shao, S. Chen, Z. Hu, H. Cai and F. Huang, *Prog. Polym. Sci.*, 2023, 101711.
189 F. Zahedi, S. Pourmahdian, M. Zendehdel, E. Rezasoltani and N. Y. Nia, *Mater. Today Energy*, 2025, 101938.
190 X. Liu and H. Jiang, *Small*, 2024, **20**, 2404753.
191 B. Li, Q. Liu, J. Gong, S. Li, C. Zhang, D. Gao, Z. Chen, Z. Li, X. Wu and D. Zhao, *Nat. Commun.*, 2024, **15**, 2753.
192 R. Li, M. Liu, S. K. Matta, A. Almasri, J. Tian, H. Wang, H. P. Pasanen, S. P. Russo, P. Vivo and H. Zhang, *Sol. RRL*, 2023, **7**, 2300367.
193 K. Hatakeyama-Sato and K. Oyaizu, *Chem. Rev.*, 2023, **123**, 11336–11391.
194 Z. Xie, Y. Do, S. J. Choi, H.-Y. Park, H. Kim, J. Kim, D. Song, T. Gokulnath, H.-B. Kim and I. W. Choi, *J. Mater. Chem. A*, 2023, **11**, 9608–9615.
195 R. Chetri and A. TN, *Energy Fuels*, 2025, **39**, 9232–9261.
196 S. Mardi, M. Pea, A. Notargiacomo, N. Yaghoobi Nia, A. Di Carlo and A. Reale, *Materials*, 2020, **13**, 1404.
197 S. W. Tong, J. Balapanuru, D. Fu and K. P. Loh, *ACS Appl. Mater. Interfaces*, 2016, **8**, 29496–29503.

198 N. Yaghoobi Nia, E. Lamanna, M. Zendehdel, A. L. Palma, F. Zurlo, L. A. Castriotta and A. Di Carlo, *Small*, 2019, **15**, 1904399.
199 Y. Wu, N. Ding, Y. Zhang, B. Liu, X. Zhuang, S. Liu, Z. Nie, X. Bai, B. Dong and L. Xu, *Adv. Energy Mater.*, 2022, **12**, 2200005.
200 M. Almalki, A. Dučinskas, L. C. Carbone, L. Pfeifer, L. Piveteau, W. Luo, E. Lim, P. A. Gaina, P. A. Schouwink and S. M. Zakeeruddin, *Nanoscale*, 2022, **14**, 6771–6776.
201 M. A. Ruíz-Sánchez, P. M. Moreno-Romero, P. G. Abrego-Martínez, D. M. Torres-Herrera, I. M. De Los Santos, L. Hechavarría-Difur, M. Courel, F. J. Sánchez-Rodríguez, H. Hu and H. J. Cortina-Marrero, *Mater. Sci. Semicond. Process.*, 2023, **157**, 107309.
202 Z. Cao, Z. Li, M. Mooney, C. Do, K. Hong, S. Rondeau-Gagné, W. Xia and X. Gu, *Macromolecules*, 2024, **57**, 10379–10388.
203 S. Subianto, R. Balu, L. de Campo, A. Sokolova, N. K. Dutta and N. R. Choudhury, *ACS Appl. Mater. Interfaces*, 2018, **10**, 44116–44125.
204 C. Beaumont, S. Naqvi and M. Leclerc, *Trends Chem.*, 2022, **4**, 714–725.
205 D. Pan, J. S. Olsson and P. Jannasch, *ACS Appl. Energy Mater.*, 2021, **5**, 981–991.
206 J. Wu, Z. Ren, F. Tang, W. Zhang, G. He, X. Yin, C. Gao and L. Wang, *Chem. Eng. J.*, 2024, **490**, 151650.
207 J. Wheeler and I. Zozoulenko, *Adv. Electron. Mater.*, 2024, 2400662.
208 K. Ji, J. Yuan, F. Li, Y. Shi, X. Ling, X. Zhang, Y. Zhang, H. Lu, J. Yuan and W. Ma, *J. Mater. Chem. A*, 2020, **8**, 8104–8112.
209 T. Zhu, L. Shen, H. Chen, Y. Yang, L. Zheng, R. Chen, J. Zheng, J. Wang and X. Gong, *J. Mater. Chem. A*, 2021, **9**, 21910–21917.
210 M. Xiao, R. L. Carey, H. Chen, X. Jiao, V. Lemaur, S. Schott, M. Nikolka, C. Jellett, A. Sadhanala and S. Rogers, *Sci. Adv.*, 2021, **7**, eabe5280.
211 S. Fratini, M. Nikolka, A. Salleo, G. Schweicher and H. Sirringhaus, *Nat. Mater.*, 2020, **19**, 491–502.
212 C.-C. Wu, E. Y. Li and P.-T. Chou, *Chem. Sci.*, 2022, **13**, 7181–7189.
213 H. Zheng, Y. Guo, Z. Lin and J. Peng, *Acc. Mater. Res.*, 2025, **6**(9), 1158–1171.
214 M. Acik and S. B. Darling, *J. Mater. Chem. A*, 2016, **4**, 6185–6235.
215 G. Ganesh, A. Yasin, I. I. Misnon, A. Fakharuddin, L. Schmidt-Mende, M. H. Ab Rahim, S. Thomas and R. Jose, *Sol. Energy*, 2023, **257**, 266–306.
216 C. Kim, H. Joung, H. J. Kim, K. Paeng, L. J. Kaufman and J. Yang, *NPG Asia Mater.*, 2023, **15**, 32.
217 W. Khelifi and C. K. Luscombe, *Prog. Polym. Sci.*, 2024, 101804.
218 L. Zhao, W. Li, H. Qin, X. Yi, W. Zeng, Y. Zhao and H. Chen, *Macromolecules*, 2023, **56**, 2990–3003.
219 D. Ko, H. Jung and M. Park, *ACS Appl. Energy Mater.*, 2024, **7**, 5986–5994.
220 T. Wu, P. Wang, L. Zheng, Y. Zhao and Y. Hua, *Adv. Energy Mater.*, 2024, **14**, 2400078.
221 J. Jiménez-López, B. M. D. Puscher, W. Cambarau, R. H. Fink, E. Palomares and D. M. Guldi, *Nanoscale*, 2019, **11**, 23357–23365.
222 I. Ahmed, L. Shi, H. Pasanen, P. Vivo, P. Maity, M. Hatamvand and Y. Zhan, *Light Sci. Appl.*, 2021, **10**, 174.
223 J. Jiménez-López, B. M. D. Puscher, W. Cambarau, R. H. Fink, E. Palomares and D. M. Guldi, *Nanoscale*, 2019, **11**, 23357–23365.
224 T. Wang, W. Deng, J. Cao and F. Yan, *Adv. Energy Mater.*, 2023, **13**, 2201436.
225 S. Wu, Z. Li, J. Zhang, X. Wu, X. Deng, Y. Liu, J. Zhou, C. Zhi, X. Yu and W. C. H. Choy, *Adv. Mater.*, 2021, **33**, 2105539.
226 Q. Lou, X. Xu, Z. Xu, T. Dai, H. Zhang, L. Zhao, F. Wang, E. Zhou, F. Gao and H. Zhou, *Cell Rep Phys Sci.*, 2025, **6**(4), 102515.
227 Y. Yang, Q. Xiong, J. Wu, Y. Tu, T. Sun, G. Li, X. Liu, X. Wang, Y. Du and C. Deng, *Adv. Mater.*, 2024, **36**, 2310800.
228 G. Welyab, M. Abebe, D. Mani, J. K. Paduvilan, L. Thottathi, A. Thankappan, S. Thomas, T. H. Wondimu and J. Y. Kim, *Next Nanotechnol.*, 2024, **5**, 100053.
229 L. He, H. Zhang, D. Zhang, C. Gao, H. Su, D. Du, D. Ding, H. Liu and W. Shen, *Adv. Funct. Mater.*, 2024, **34**, 2403020.
230 R. F. Pineda, B. R. M. Lake, J. Troughton, I. Sanchez-Molina, O. Chepelin, S. Haque, T. Watson, M. P. Shaver and N. Robertson, *Phys. Chem. Chem. Phys.*, 2018, **20**, 25738–25745.
231 D. A. M. de Alencar, G. Koch, F. De Rossi, A. Generosi, G. Ferraro, M. Bonomo, S. Noola, G. Pellis, P. Quagliotto and B. Paci, *Adv. Sustain. Syst.*, 2025, **9**, 2400674.
232 S. Yin, X. Luo, F. Tang, W. Zhong, W. Yang, Z. Xiong, Y. Lin, F. Peng and L. Ying, *Adv. Energy Mater.*, 2025, **15**, 2404575.
233 N. Rai, S. S. Reddy, A. D. Scully, K. L. J. Weerarathna, U. Bach and A. N. Simonov, *Adv. Mater. Technol.*, 2024, **9**, 2301539.
234 D. H. Lee, S. Lim, C. Kim, H. U. Lee, D. Chung, Y. Choi, J. Choi, Y. Kim, S. B. Cho and H. Il Kim, *ACS Energy Lett.*, 2023, **8**, 1839–1847.
235 Z. Zhang, J. Fu, Q. Chen, J. Zhang, Z. Huang, J. Cao, W. Ji, L. Zhang, A. Wang and Y. Zhou, *Small*, 2023, **19**, 2206952.
236 Z. Xie, J. Park, H. Kim, B. H. Cho, C. Lakshman, H.-Y. Park, T. Gokulnath, Y.-Y. Kim, J. Yoon and J.-S. Jee, *ACS Appl. Mater. Interfaces*, 2024, **16**, 3359–3367.
237 Z. Xie, J. Park, H. Kim, B. H. Cho, C. Lakshman, H.-Y. Park, T. Gokulnath, Y.-Y. Kim, J. Yoon and J.-S. Jee, *ACS Appl. Mater. Interfaces*, 2024, **16**, 3359–3367.
238 T. R. Rana, M. Abbas, E. Schwartz, F. Jiang, M. Y. Yaman, Z. Xu, D. S. Ginger and D. MacKenzie, *ACS Energy Lett.*, 2024, **9**, 1888–1894.
239 J. T. Matondo, H. Hu, Y. Ding, M. Mateen, G. Cheng and J. Ding, *Adv. Mater. Technol.*, 2024, **9**, 2302082.
240 R. Keshavarzi, F. Hajisharifi, Z. Saki, M. Omrani, R. Sheibani, N. Afzali, M. Abdi-Jalebi, L. Vesce and A. Di Carlo, *Nano Today*, 2025, **61**, 102600.

241 T. Yokoyama, T.-B. Song, D. H. Cao, C. C. Stoumpos, S. Aramaki and M. G. Kanatzidis, *ACS Energy Lett.*, 2017, **2**, 22–28.
242 K. B. Lohmann, J. B. Patel, M. U. Rothmann, C. Q. Xia, R. D. J. Oliver, L. M. Herz, H. J. Snaith and M. B. Johnston, *ACS Energy Lett.*, 2020, **5**, 710–717.
243 J. P. Chen, T. W. Colburn, J. Risner-Jamtgaard, A. Vailionis, A. Barnum, M. Golding, A. Carbone, A. C. Flick and R. H. Dauskardt, *Matter*, 2025, **8**(3), 101990.
244 B. Tyagi, N. Kumar, H. B. Lee, M. M. Ovhal, V. V. Satale, A. Mohamed, D. Kim and J. Kang, *Small Methods*, 2024, **8**, 2300237.
245 N. A. N. Ouedraogo, Y. Ouyang, B. Guo, Z. Xiao, C. Zuo, K. Chen, Z. He, G. O. Odunmbaku, Z. Ma and W. Long, *Adv. Energy Mater.*, 2024, **14**, 2401463.
246 F. Mathies, H. Eggers, B. S. Richards, G. Hernandez-Sosa, U. Lemmer and U. W. Paetzold, *ACS Appl. Energy Mater.*, 2018, **1**, 1834–1839.
247 Y. Zhong, R. Munir, J. Li, M.-C. Tang, M. R. Niazi, D.-M. Smilgies, K. Zhao and A. Amassian, *ACS Energy Lett.*, 2018, **3**, 1078–1085.
248 H. Fang, W. Shen, H. Guan, G. Chen, G. Li, W. Ai, S. Fu, Z. Xu, W. Chen and P. Jia, *Adv. Mater.*, 2025, **37**, 2414790.
249 J. E. Huddy and W. J. Scheideler, in *2024 IEEE 52nd Photovoltaic Specialist Conference (PVSC)*, IEEE, 2024, pp. 483–485.
250 J. E. Huddy, Y. Ye and W. J. Scheideler, *Adv. Mater. Technol.*, 2022, **7**, 2101282.
251 P. Luo, S. Zhou, W. Xia, J. Cheng, C. Xu and Y. Lu, *Adv. Mater. Interfaces*, 2017, **4**, 1600970.
252 T. Huang, Y. Zhang, J. Sun, Y. Gu, F. Wang, Y.-W. Lu and P. Luo, *ACS Appl. Energy Mater.*, 2024, **7**, 11225–11232.
253 X. Tian, S. D. Stranks, J. Huang, V. M. Fthenakis, Y. Yang and F. You, *Energy Environ. Sci.*, 2025, **18**, 194–213.
254 L. de Queiroz Corrêa, B. H. de Souza Miranda, G. de Amorim Soares and D. Bagnis, in *Sustainable Strategies in Organic Electronics*, Elsevier, 2022, pp. 521–560.
255 E. Aydin, T. G. Allen, M. De Bastiani, A. Razzaq, L. Xu, E. Ugur, J. Liu and S. De Wolf, *Science*, 2024, **383**, eadh3849.
256 A. Khorasani, F. Mohamadkhani, M. Marandi, H. Luo and M. Abdi-Jalebi, *Adv. Energy Sustain. Res.*, 2024, **5**, 2300275.
257 J. Liu, M. Zhang, X. Sun, L. Xiang, X. Yang, X. Hu, Z. Wang, T. Hou, J. Qin and Y. Huang, *Nano-Micro Lett.*, 2025, **17**, 318.
258 B. Kang and F. Yan, *Energy Environ. Sci.*, 2025, **18**, 3917–3954.
259 P. Wang, Y. Han, Z. Lv, L. Miao, M. Wang, Z. Liu, T. Feng, M. Gao, Y. Shi and R. Cai, *J. Phys. Chem. Lett.*, 2025, **16**, 2695–2704.
260 N. Camaioni, C. Carbonera, L. Ciammaruchi, G. Corso, J. Mwaura, R. Po and F. Tinti, *Adv. Mater.*, 2023, **35**, 2210146.
261 H. Zheng, Z. Tang, P. Liang, H. Shu, L. Wang, J. Huang, A. A. Levin, P. N. Brunkov and Z. Liu, *Thin Solid Films*, 2021, **732**, 138781.
262 G. G. Njema, B. C. Mosonik, C. C. Ahia and J. K. Kibet, *Chem.–Eur. J.*, 2024, **30**, e202403192.
263 L. Lin, L. Yang, G. Du, X. Li, Y. Li, J. Deng, K. Wei and J. Zhang, *ACS Appl. Energy Mater.*, 2023, **6**, 10303–10318.
264 J. P. Velásquez, E. A. Ramírez, A. Flórez, J. F. Montoya, R. Betancur, D. Ramírez, M. da S. Carvalho and F. Jaramillo, *Adv. Eng. Mater.*, 2023, **25**, 2201561.
265 X. Tian, J. Wang, J. Ji and G. Lu, *Renew. Energy*, 2025, **240**, 122170.
266 F. Li, C. Gong, B. Fan, Z. Xing, X. Meng, S. Zhang, X. Hu and Y. Chen, *Adv. Funct. Mater.*, 2022, **32**, 2206412.
267 R. Chen, Y. Yang, Z. Dai, L. Yuan, J. Du, P. Yang, Y. Yang, H. Shen, Z. Liu and H. Wang, *Nano Energy*, 2023, **115**, 108759.
268 Y. Wu, D. Liu, W. Chu, B. Wang, A. S. Vasenko and O. V Prezhdo, *Nanoscale*, 2025, **17**, 2224–2234.
269 Q. Wei, D. Zheng, L. Liu, J. Liu, M. Du, L. Peng, K. Wang and S. Liu, *Adv. Mater.*, 2024, **36**, 2406295.
270 H. Hu, D. B. Ritzer, A. Diercks, Y. Li, R. Singh, P. Fassl, Q. Jin, F. Schackmar, U. W. Paetzold and B. A. Nejand, *Joule*, 2023, **7**, 1574–1592.
271 C. Chen, J. Chen, H. Han, L. Chao, J. Hu, T. Niu, H. Dong, S. Yang, Y. Xia and Y. Chen, *Nature*, 2022, **612**, 266–271.
272 B. Dou, J. B. Whitaker, K. Bruening, D. T. Moore, L. M. Wheeler, J. Ryter, N. J. Breslin, J. J. Berry, S. M. Garner and F. S. Barnes, *ACS Energy Lett.*, 2018, **3**, 2558–2565.
273 K. Chen, Y. Zeng, X. Gao, X. Liu, L. Zhu and F. Wu, *ChemSusChem*, 2024, **17**, e202301349.
274 T. Xu, Z. Wan, H. Tang, C. Zhao, S. Lv, Y. Chen, L. Chen, Q. Qiao and W. Huang, *J. Alloys Compd.*, 2021, **859**, 157784.
275 Y. Wang, Y. Wang, L. Deng, X. Li, X. Zhang, H. Wang, C. Li, Z. Shi, T. Hu and K. Liu, *Adv. Energy Mater.*, 2024, **14**, 2402066.
276 J. T. Matondo, H. Hu, Y. Ding, M. Mateen, G. Cheng and J. Ding, *Adv. Mater. Technol.*, 2024, **9**, 2302082.
277 J. T. Matondo, H. Hu, Y. Ding, M. Mateen, G. Cheng and J. Ding, *Adv. Mater. Technol.*, 2024, **9**, 2302082.
278 M. Wang, Y. Zhao, X. Jiang, Y. Yin, I. Yavuz, P. Zhu, A. Zhang, G. S. Han, H. S. Jung and Y. Zhou, *Joule*, 2022, **6**, 1032–1048.
279 J. Hu, C. Wang, S. Qiu, Y. Zhao, E. Gu, L. Zeng, Y. Yang, C. Li, X. Liu and K. Forberich, *Adv. Energy Mater.*, 2020, **10**, 2000173.
280 L. J. Sutherland, H. C. Weerasinghe and G. P. Simon, *Adv. Energy Mater.*, 2021, **11**, 2101383.
281 X. Tan, S. Wang, Q. Zhang, H. Wang, H. Liu, W. Li, L. Zhu, T. Song, Z. Cui and Y. Bai, *J. Mater. Chem. A*, 2023, **11**, 1920–1926.
282 J. Cho and P. V Kamat, *Chem. Mater.*, 2020, **32**, 6206–6212.
283 L. Li, Z. Huang, X. Meng, Z. Xing, B. Fan, J. Li and Y. Chen, *Adv. Mater.*, 2024, **36**, 2310752.
284 Z. Chu, B. Fan, W. Shi, Z. Xing, C. Gong, J. Li, L. Li, X. Meng, M. B. K. Niazi and X. Hu, *Adv. Funct. Mater.*, 2025, 2424191.
285 L. Li, Z. Huang, X. Meng, Z. Xing, B. Fan, J. Li and Y. Chen, *Adv. Mater.*, 2024, **36**, 2310752.
286 F. Wang, T. Liu, Y. Liu, Y. Zhou, X. Dong, Y. Zhang, X. Shi, Y. Dou, Z. Ren and L. Wang, *Adv. Mater.*, 2024, **36**, 2412059.

287 T. Liu, Z. Ren, Y. Liu, Y. Zhang, J. Liang, F. Cheng, Y. Li, X. Shi, Y. Dou and X. Hu, *Sci. Adv.*, 2025, **11**, eadu3493.
288 M. M. Byranvand, F. Behboodi-Sadabad, A. A. Eliwi, V. Trouillet, A. Welle, S. Ternes, I. M. Hossain, M. R. Khan, J. A. Schwenzer and A. Farooq, *J. Mater. Chem. A*, 2020, **8**, 20122–20132.
289 S. Smeets, Q. Liu, J. Vanderspikken, T. J. Quill, S. Gielen, L. Lutsen, K. Vandewal and W. Maes, *Chem. Mater.*, 2023, **35**, 8158–8169.
290 Z. Wang, Z. Peng, N. Balar and H. Ade, *J. Mater. Chem. A*, 2024, **12**, 113–120.
291 C.-K. Pan, Y.-F. Ding, Z.-F. Yao, X.-Y. Wang, Y.-Y. Zhou, X.-Z. Wu, J.-Y. Wang and J. Pei, *Macromolecules*, 2024, **57**, 4107–4117.
292 Z. Chen, B. Wu, B. Yin, Y. Li, K. Liu, S. Kim, X. Gao, Z. Huang, Z. Liu and C. Yang, *Macromol. Chem. Phys.*, 2025, 2400464.
293 F. Ershad, W. Song and C. Yu, *Nat. Photonics*, 2023, **17**, 928–930.
294 L. Li, Z. Huang, X. Meng, Z. Xing, B. Fan, J. Li and Y. Chen, *Adv. Mater.*, 2024, **36**, 2310752.
295 H. Hu, M. Chen, N. Yao, L. Wu, Q. Zhong, B. Song, M. Cao and Q. Zhang, *ACS Appl. Mater. Interfaces*, 2021, **13**, 4017–4025.
296 A. Alasiri, K. Zubair, S. Rassel, D. Ban and O. D. Alshehri, *Heliyon*, 2024, **10**(20), e39141.
297 N. A. N. Ouedraogo, M. Yang, C. He, Y. Chen, X. Zhang, H. Yan, C. B. Han and Y. Zhang, *Sustain. Energy Fuels*, 2020, **4**, 4257–4263.
298 J. Peng, J. I. Khan, W. Liu, E. Ugur, T. Duong, Y. Wu, H. Shen, K. Wang, H. Dang and E. Aydin, *Adv. Energy Mater.*, 2018, **8**, 1801208.
299 L. Hu, L. Zhang, W. Ren, C. Zhang, Y. Wu, Y. Liu, Q. Sun, Z. Dai, Y. Cui and L. Cai, *J. Mater. Chem. C*, 2022, **10**, 9714–9722.
300 X. Meng, J. Lin, X. Liu, X. He, Y. Wang, T. Noda, T. Wu, X. Yang and L. Han, *Adv. Mater.*, 2019, **31**, 1903721.
301 J. Kang, R. Huang, S. Guo, G. Han, X. Sun, I. Ismail, C. Ding, F. Li, Q. Luo and Y. Li, *Sol. Energy*, 2021, **217**, 105–112.
302 F. Qi, Y. Li, F. R. Lin and A. K. Jen, *ChemSusChem*, 2024, e202301559.
303 C. Li, J. Yin, R. Chen, X. Lv, X. Feng, Y. Wu and J. Cao, *J. Am. Chem. Soc.*, 2019, **141**, 6345–6351.
304 N. Y. Nia, M. Zendehdel, M. Abdi-Jalebi, L. A. Castriotta, F. U. Kosasih, E. Lamanna, M. M. Abolhasani, Z. Zheng, Z. Andaji-Garmaroudi and K. Asadi, *Nano Energy*, 2021, **82**, 105685.
305 M. Haghighi, N. Ghazyani, S. Mahmoodpour, R. Keshtmand, A. Ghaffari, H. Luo, R. Mohammadpour, N. Taghavinia and M. Abdi-Jalebi, *Sol. RRL*, 2023, **7**, 2201080.
306 C. Fei, N. Li, M. Wang, X. Wang, H. Gu, B. Chen, Z. Zhang, Z. Ni, H. Jiao and W. Xu, *Science*, 2023, **380**, 823–829.
307 C. Fei, N. Li, M. Wang, X. Wang, H. Gu, B. Chen, Z. Zhang, Z. Ni, H. Jiao and W. Xu, *Science*, 2023, **380**, 823–829.
308 H. Kassem, A. Salehi and M. Kahrizi, *Energy Technol.*, 2024, **12**, 2301032.
309 C. Sun, F. Pan, H. Bin, J. Zhang, L. Xue, B. Qiu, Z. Wei, Z.-G. Zhang and Y. Li, *Nat. Commun.*, 2018, **9**, 743.
310 X. Rodríguez-Martínez, E. Pascual-San-José and M. Campoy-Quiles, *Energy Environ. Sci.*, 2021, **14**, 3301–3322.
311 N. Y. Nia, F. Matteocci, L. Cina and A. Di Carlo, *ChemSusChem*, 2017, **10**, 3854–3860.
312 L. Gao, J. Lin, L. Wang and L. Du, *Acc. Mater. Res.*, 2024, **5**, 571–584.
313 L. Ding, Z.-D. Yu, X.-Y. Wang, Z.-F. Yao, Y. Lu, C.-Y. Yang, J.-Y. Wang and J. Pei, *Chem. Rev.*, 2023, **123**, 7421–7497.
314 S. M. Lee, K. H. Park, S. Jung, H. Park and C. Yang, *Nat. Commun.*, 2018, **9**, 1–8.
315 W. Shin, W. Ko, S.-H. Jin, T. Earmme and Y.-J. Hwang, *Chem. Eng. J.*, 2021, **412**, 128572.
316 X. Wang, Z. Ding, X. Huang, X. Liu, Y. Wang, Y. Wang and W. Huang, *J. Mater. Chem. C*, 2024, **12**, 351–387.
317 P. Holzhey, M. Prettl, S. Collavini, N. L. Chang and M. Saliba, *Joule*, 2023, **7**, 257–271.
318 J. J. Cordell, M. Woodhouse and E. L. Warren, *Joule*, 2025, **9**(2), 101781.
319 P. Zhu, C. Chen, J. Dai, Y. Zhang, R. Mao, S. Chen, J. Huang and J. Zhu, *Adv. Mater.*, 2024, **36**, 2307357.
320 P. Zhu, C. Chen, J. Dai, Y. Zhang, R. Mao, S. Chen, J. Huang and J. Zhu, *Adv. Mater.*, 2024, **36**, 2307357.